RICE UNIVERSITY

Impact of Sunlight and Natural Organic Matter on the Fate, Transport, and Toxicity of Carbon Based Nanomaterials

by

Xiaolei Qu

A THESIS SUBMITTED
IN PARTIAL FULFILLMENT OF THE
REQUIREMENTS FOR THE DEGREE

Doctor of Philosophy

APPROVED, THESIS COMMITTEE

Qilin Li, Associate Professor, Civil and Environmental Engineering

Pedro J.J. Alvarez, Chair, George R. Brown Professor, Civil and Environmental Engineering

Weiwei Zhong, Assistant Professor, Biochemistry and Cell Biology

R. Bruce Weisman, Professor, Chemistry

HOUSTON, TEXAS
May 2013

ABSTRACT

Impact of Sunlight and Natural Organic Matter on the Fate, Transport, and Toxicity of Carbon Based Nanomaterials

By

Xiaolei Qu

The fast growing production of carbon based nanomaterials (CNMs) and their potential widespread use in consumer products raise concerns regarding their potential environmental risks. The present study investigated the role of photochemical transformation and natural organic matter (NOM) in the fate, transport, and toxicity of fullerenes and carbon nanotubes (CNTs) in natural aquatic systems, providing fundamental information for risk assessment and management.

Photochemical transformation of aqueous fullerene nanoparticles (nC_{60}) and CNTs occurs at significant rates under UVA irradiation at intensity similar to that in sunlight. The transformation processes are mediated by self-generated ROS, resulting in changes of surface structure depending on the initial surface oxidation state of CNMs. UVA irradiation leads to oxygenation of nC_{60} surface and decarboxylation of carboxylated multi-walled carbon nanotubes (COOH-MWCNTs).

The environmental transport of CNMs is significantly affected by their surface chemistry, concentration and species of electrolytes, and concentration and properties of co-existing NOM. In electrolyte solutions without NOM, the mobility of CNMs is largely

decided by their surface chemistry, primarily the oxygen-containing functional groups. The mobility of nC_{60} greatly depends on its surface oxygen concentration, while the mobility of COOH-MWCNTs correlates well with the abundance of surface carboxyl groups.

Humic acid, as a surrogate of NOM, can significantly enhance nC_{60} stability through steric hindrance. The extent of stabilization depends on the amount and properties of humic acid adsorbed. Humic acid has limited adsorption on UVA-irradiated nC_{60}. Soil humic acid is more efficient in stabilizing nC_{60} than aquatic humic acid due to its higher molecular weight. Humic acid immobilized onto the silica surface can enhance or hinder nC_{60} deposition, depending on the complex interplay of attractive and repulsive forces.

MWCNTs are more toxic to bacteria, *Escherichia coli*, than COOH-MWCNTs due to their higher bioavailability and oxidative capacity. Surface oxidation induced by ·OH reduces the toxicity of MWCNTs. Oxidative stress is a major toxicity mechanism, which can be mitigated by adding antioxidants.

Overall, this study highlights the critical role of environment-induced structural changes of CNMs in their potential environmental risks. It also provides structure-activity relationships for the assessment of CNM mobility and toxicity.

Acknowledgements

I would like to thank my advisors Professor Qilin Li and Professor Pedro Alvarez. Their valuable knowledge, insight, and criticisms are indispensable to this dissertation work. I am grateful for all the guidance and opportunities they have provided me. I also want to thank my thesis committee members Professor Weiwei Zhong and Professor Bruce Weisman for their advice and support.

I want to thank Dr. Yu Sik Hwang for his guidance and assistance to get me started on this project. I would like to thank my lab mates and colleagues in the department: Jinjian Wu, Cong Yu, Dr. Michael Liga, Dr. Alison Contreras, Jianwei Ma, Dr. Sen Wang, Xuening Li, Jonathon Brame, Jie Ma, Mengyan Li, Dr. Yu Yang, Dr. Zongmin Xiu, Jing Wang and many other people who have helped me in many ways during my stay at Rice. It is my great pleasure to work with them.

I'd like to thank the SEA staff, especially Dr. Bo Chen, Dr. Liang Gang, and Dr. Wenhua Guo for their training and technical support. I want to thank Andrea Torres, Jennifer Mashburn, and Sandra Baylor for their kindly help and support.

I'd like to acknowledge the funding agencies that supported my study and research: NSF Center for Biological and Environmental Nanotechnology (Award EEC-0647452), EPA STAR program (grant # R834093) and WateReuse Research Foundation (grant # WateReuse-10-13).

This dissertation is dedicated to my wife Ao Kong and my parents Ming Qu and Yajun Zhang. Their unconditional love and support is the strength of my life.

Table of Contents

List of Figures and Tables

The following publications have been published or prepared for submission based on this dissertaition.

1. Qu, X.L., Alvarez, P.J.J., Li, Q.L. Self-generated ROS Mediate the Photochemical Transformation of Carboxylated Multi-walled Carbon Nanotubes in Sunlight. In preparation.

2. Qu, X.L., Alvarez, P.J.J., Li, Q.L. Impact of Sunlight and Humic Acid on the Deposition Kinetics of Aqueous Fullerene Nanoparticles (nC_{60}). *Environmental Science & Technology* 46(24), 2012.

3. Hwang, Y.S., Qu, X.L., Li, Q.L. Aggregation and Deposition of Carboxylated Multi-Walled Carbon Nanotubes Suspended in Water: Role of Photochemical Transformation. *Carbon* 55 81-89. 2012.

4. Qu, X.L., Alvarez, P.J.J., Li, Q.L. Applications of Nanotechnology in Water and Wastewater Treatment. *Water Research*. *Special Issue: Nanotechnology for Water and Wastewater Treatment.* ASAP. DOI: 10.1016/j.watres.2012.09.058. 2012.

5. Qu, X.L., Brame, J., Li, Q. and Alvarez, J.J.P. Nanotechnology for a Safe and Sustainable Water Supply: Enabling Integrated Water Treatment and Reuse. *Accounts of Chemical Research*. 46(3), 834-843. 2013.

6. Qu, X.L., Hwang, Y.S., Alvarez, P.J.J., Bouchard, D. and Li, Q.L. UV Irradiation and Humic Acid Mediate Aggregation of Aqueous Fullerene (nC_{60}) Nanoparticles. *Environmental Science & Technology* 44(20), 7821-7826. 2010.

7. Qu, X. L.; Li, Q. L.; Alvarez, P. J. J.; Choi, Y. C.; Conlon, W. J.; Diaz, I. Review of Nanomaterial Research and Relevance for Water Reuse. In press. WateReuse Research Foundation, Alexandria, VA.

Chapter 1: Introduction and Statement of Purpose

1.1 Introduction

The word "nano", derived from the Greek νᾶνος, is used in the metric system as a prefix to mean 10^{-9} or one-billionth. According to the National Nanotechnology Initiative, nanotechnology is "the understanding and control of matter at dimensions between approximately 1 and 100 nanometers, where unique phenomena enable novel applications". Although this is not a unanimously accepted definition, most organizations and countries have the same elements in their definition of nanotechnology: control or manipulation of matter in the nanoscale range that confers unique properties and reactivity distinct from those of bulk materials.

Carbon based nanomaterials (CNMs, e.g., carbon nanotubes and fullerenes) are a distinct group of nanomaterials that have no bulk counterparts. Carbon nanotubes (CNTs) and fullerenes are both allotropes of carbon. Fullerenes have enclosed cagelike structures composed of 12 five-membered carbon rings and a nonspecific number of six-membered carbon rings. CNTs are hollow structures that can be visualized as graphene sheets, one single atomic layer of carbon, rolled up into cylinders with nanoscale diameter and possibly capped by half fullerenes. The electrical, mechanical, optical and many other unique physicochemical properties of CNMs enable a wide range of promising applications. CNTs have already been applied in a number of commercial products such as rechargeable batteries, automotive parts, sporting goods, boat hulls and water filters [1]. Fullerenes are now mainly commercially used in cosmetics as antioxidants. A recent study estimated the production of fullerenes and CNTs to be 2 ~ 80 and 55 ~ 1,101 tons

per year respectively as of 2011 [2]. Their potential widespread use in consumer products will inevitably lead to their presence in the natural environment. Fate and transport modeling predicted the concentrations of fullerenes and CNTs at the order of magnitude of pg/L ~ ug/L in surface waters and ng/L ~ ug/L in engineered systems [3-6]. Evidence from the literature suggested that CNMs pose toxicity to various organisms such as microorganisms (e.g., bacteria [7-14], algae [15-17] protozoa [18, 19] and fungi [20]), aquatic invertebrates (e.g., daphnia) and vertebrates (e.g., fish) [21], and human cell lines [22], raising concerns regarding their adverse impact on human health and ecological systems. As a result, the fate, transport and toxicity of CNMs and their relation to nanomaterial structure need to be carefully studied in order to assess and mitigate potential hazards.

Significant studies have been devoted to investigating the release, fate and transport, bioavailability, and toxicity of CNMs. However, the predictive capabilities for CNM environmental behaviors are still very limited due to several major knowledge gaps and challenges. One of the most critical challenges is rooted in the diversity of the CNM structures and their environmental transformations. Unlike traditional pollutants such as organic chemicals and ions, each kind of CNMs comes in a myriad of different forms. Moreover, their environmental behaviors strongly depend on the physical and chemical structures. Possible transformation processes of CNMs can change their physicochemical properties and consequently alter their environmental risks. However, the transformation of CNMs under natural conditions and its impact on the potential environmental risks have not been systematically investigated. The present study focuses on bridging this key knowledge gap by examining the impact of interactions with sunlight and NOM on the fate, transport and toxicity of two major CNMs, fullerene C_{60} nanoparticles and CNTs.

1.2 Objectives and Scope of Dissertation

The overall objective of this dissertation work is to determine the role of photochemical transformation and natural organic matter in the fate, transport, and toxicity of carbon based nanomaterials in natural aquatic systems, providing fundamental information for risk assessment.

Specifically, it was broken down into following objectives:

Objective 1: To investigate the photochemical transformation of carbon based nanomaterials in the presence of sunlight and its potential mechanisms.

Objective 2: To address the impact of photochemical transformation and NOM on the transport behaviors (i.e., aggregation and deposition) of carbon based nanomaterials in realistic aqueous conditions.

Objective 3: To determine the effects of photochemical transformation on the toxicity of carbon based nanomaterials.

1.3 Thesis Organization

The present thesis comprises seven chapters. Chapter 1 is a brief introduction to this investigation including the background and research objectives. The following chapter provides a thorough literature review of relevant topics covered in this dissertation including the phototransformation, environmental transport, and toxicity of CNMs. The laboratory investigation results will be presented in Chapter 3-6. The contents of each

separate chapter have been either published by or prepared for peer-reviewed journals. The major conclusions and engineering significance of this work, as well as future research needs, will be discussed in Chapter 7. A brief description of the laboratory investigation (Chapter 3-6) is presented below.

Objective 1: To investigate the photochemical transformation of carbon based nanomaterials in the presence of sunlight and its potential mechanisms.

The first part of the laboratory investigation (Chapter 3) aims to achieve the sub-objective pertaining to the phototransformation of CNTs under sunlight exposure and its mechanisms. It also covers the impact of phototransformation on the aggregation and deposition behaviors of CNTs.

In the entire investigation, the sunlight was simulated by UVA irradiation which is the major UV light in the solar spectrum. The production of ROS including $^1O_2$ and ·OH by COOH-MWCNTs under UVA light was quantified using probe molecules. COOH-MWCNTs were later reacted with externally generated $^1O_2$ and ·OH respectively to examine their impacts on nanotube surface chemistry. The changes of oxygen-containing functional group distribution and the surface defects of COOH-MWCNTs were characterized by chemical derivatization in conjunction with X-ray photoelectron spectroscopy (XPS) and Raman spectroscopy. They were later compared with the corresponding changes in photochemical transformation of COOH-MWCNTs under UVA light to illustrate the differential roles of self-generated ROS in phototransformation process. Inhibition experiments in low-oxygen conditions and in the presence of hole scavengers were performed to further reveal the reaction mechanisms

and the generation route of ·OH. Impact of ·OH on the stability of COOH-MWCNTs was examined using sedimentation experiments to elucidate the potential implications of phototransformation on their transport in aquatic systems. The aggregation kinetics of COOH-MWCNT before and after irradiation was also studied using dynamic light scattering (DLS) in NaCl and $CaCl_2$ solutions, and their deposition kinetics was examined by quartz crystal microbalance with dissipation monitoring (QCM-D) on a silica surface.

Objective 2: To address the impact of photochemical transformation and NOM on the transport behaviors (i.e., aggregation and deposition) of carbon based nanomaterials in realistic aqueous conditions.

Chapter 3 and 4 illustrate the impact of sunlight and NOM on the aggregation and deposition behaviors of nC_{60}, respectively.

In Chapter 3, the initial aggregation kinetics of both pristine and irradiated nC_{60} was investigated by DLS in solutions varying in ionic strength, ionic composition and humic acid concentration. nC_{60} before and after UVA irradiation were characterized using particle size and surface potential measurements and XPS. The influence of sunlight irradiation was examined by comparing the aggregation of nC_{60} and irradiated nC_{60} in NaCl and $CaCl_2$ solutions. Ca^{2+} was introduced to the experiment design due to its abundance in the natural aquatic systems and its ability to specifically bond oxygen-containing functional groups on irradiated nC_{60} surface. The role of NOM on nC_{60} aggregation was evaluated through comparison between aggregation kinetics with and without the presence of dissolved Suwannee River humic acid (SRHA) and batch

sorption of SRHA on nC_{60}. Classic DLVO theory of colloidal stability was employed to interpret data and explore non-DLVO forces involved.

In Chapter 4, the impact of UVA irradiation and humic acid, in either dissolved or surface-immobilized form, on deposition of nC_{60} on a silica surface was studied using packed column experiments and QCM-D under various solution conditions. The silica surface serves as a surrogate for natural sediments. nC_{60} irradiated by UVA for varying periods of time was thoroughly characterized, and its deposition kinetics on bare and humic acid coated silica surface measured under different NaCl and humic acid concentrations was compared to that of pristine nC_{60}. Both aquatic humic acid (SRHA) and soil humic acid (Elloitt humic acid, EHA) were used in this study to probe the influence of humic acid properties on their ability to alter the deposition of nC_{60}.

Objective 3: To determine the effects of photochemical transformation on the toxicity of carbon based nanomaterials.

The influence of phototransformation on the toxicity of carbon nanotubes will be discussed in Chapter 6, in which the impact of environment-induced structure change on CNT toxicity was investigated using *Escherichia coli* as a model organism. Both MWCNT and COOH-MWCNT were reacted with ·OH to simulate their phototransformation in the environment. The antibacterial activity of reacted CNTs was quantified by plate counting method and compared to the initial CNTs. Antioxidants were used in the inhibition experiment to further reveal the toxicity mechanisms. The oxidative capacity of different CNT samples was quantified by their ability to oxidize reduced glutathione, a common antioxidant and redox state mediator.

1.4 References

(1) De Volder, M. F.; Tawfick, S. H.; Baughman, R. H.; Hart, A. J., Carbon Nanotubes: Present and Future Commercial Applications. *Science* **2013,** *339*, (6119), 535-539.

(2) Hendren, C. O. H. C. O.; Mesnard, X.; Droge, J.; Wiesner, M. R., Estimating Production Data for Five Engineered Nanomaterials As a Basis for Exposure Assessment. *Environ. Sci. Technol.* **2011,** *45*, (7), 2562-2569.

(3) Aschberger, K.; Micheletti, C.; Sokull-Kluttgen, B.; Christensen, F. M., Analysis of currently available data for characterising the risk of engineered nanomaterials to the environment and human health - Lessons learned from four case studies. *Environment international* **2011,** *37*, (6), 1143-56.

(4) Mueller, N. C.; Nowack, B., Exposure modeling of engineered nanoparticles in the environment. *Environ. Sci. Technol.* **2008,** *42*, (12), 4447-4453.

(5) Gottschalk, F.; Sonderer, T.; Scholz, R. W.; Nowack, B., Modeled Environmental Concentrations of Engineered Nanomaterials (TiO2, ZnO, Ag, CNT, Fullerenes) for Different Regions. *Environ. Sci. Technol.* **2009,** *43*, (24), 9216-9222.

(6) Gottschalk, F.; Sonderer, T.; Scholz, R. W.; Nowack, B., POSSIBILITIES AND LIMITATIONS OF MODELING ENVIRONMENTAL EXPOSURE TO ENGINEERED NANOMATERIALS BY PROBABILISTIC MATERIAL FLOW ANALYSIS. *Environ. Toxicol. Chem.* **2010,** *29*, (5), 1036-1048.

(7) Kang, S.; Mauter, M. S.; Elimelech, M., Physicochemical determinants of multiwalled carbon nanotube bacterial cytotoxicity. *Environ. Sci. Technol.* **2008,** *42*, (19), 7528-7534.

(8) Kang, S.; Mauter, M. S.; Elimelech, M., Microbial Cytotoxicity of Carbon-Based Nanomaterials: Implications for River Water and Wastewater Effluent. *Environ. Sci. Technol.* **2009,** *43*, (7), 2648-2653.

(9) Kang, S.; Pinault, M.; Pfefferle, L. D.; Elimelech, M., Single-walled carbon nanotubes exhibit strong antimicrobial activity. *Langmuir* **2007,** *23*, (17), 8670-8673.

(10) Vecitis, C. D.; Zodrow, K. R.; Kang, S.; Elimelech, M., Electronic-Structure-Dependent Bacterial Cytotoxicity of Single-Walled Carbon Nanotubes. *ACS Nano* **2010,** *4*, (9), 5471-5479.

(11) Arias, L. R.; Yang, L. J., Inactivation of Bacterial Pathogens by Carbon Nanotubes in Suspensions. *Langmuir* **2009,** *25*, (5), 3003-3012.

(12) Rodrigues, D. F.; Elimelech, M., Toxic Effects of Single-Walled Carbon Nanotubes in the Development of E. coli Biofilm. *Environ. Sci. Technol.* **2010,** *44*, (12), 4583-4589.

(13) Yang, C. N.; Mamouni, J.; Tang, Y. A.; Yang, L. J., Antimicrobial Activity of Single-Walled Carbon Nanotubes: Length Effect. *Langmuir* **2010,** *26*, (20), 16013-16019.

(14) Kang, S.; Herzberg, M.; Rodrigues, D. F.; Elimelech, M., Antibacterial effects of carbon nanotubes: Size does matter. *Langmuir* **2008,** *24*, (13), 6409-6413.

(15) Wei, L. P.; Thakkar, M.; Chen, Y. H.; Ntim, S. A.; Mitra, S.; Zhang, X. Y., Cytotoxicity effects of water dispersible oxidized multiwalled carbon nanotubes on marine alga, Dunaliella tertiolecta. *Aquat. Toxicol.* **2010,** *100*, (2), 194-201.

(16) Blaise, C.; Gagne, F.; Ferard, J. F.; Eullaffroy, P., Ecotoxicity of selected nano-materials to aquatic organisms. *Environ. Toxicol.* **2008,** *23*, (5), 591-598.

(17) Velzeboer, I.; Hendriks, A. J.; Ragas, A. M. J.; Van de Meent, D., Aquatic ecotoxicity tests of some nanomaterials. *Environ. Toxicol. Chem.* **2008,** *27*, (9), 1942-1947.

(18) Ghafari, P.; St-Denis, C. H.; Power, M. E.; Jin, X.; Tsou, V.; Mandal, H. S.; Bols, N. C.; Tang, X. W., Impact of carbon nanotubes on the ingestion and digestion of bacteria by ciliated protozoa. *Nat. Nanotechnol.* **2008,** *3*, (6), 347-351.

(19) Zhu, Y.; Zhao, Q. F.; Li, Y. G.; Cai, X. Q.; Li, W., The interaction and toxicity of multi-walled carbon nanotubes with Stylonychia mytilus. *J. Nanosci. Nanotechnol.* **2006,** *6*, (5), 1357-1364.

(20) Gorczyca, A.; Kasprowicz, M. J.; Lemek, T., Physiological effect of multi-walled carbon nanotubes (MWCNTs) on conidia of the entomopathogenic fungus, Paecilomyces fumosoroseus (Deuteromycotina: Hyphomycetes). *J. Environ. Sci. Health Part A-Toxic/Hazard. Subst. Environ. Eng.* **2009,** *44*, (14), 1592-1597.

(21) Zhu, S. Q.; Oberdorster, E.; Haasch, M. L., Toxicity of an engineered nanoparticle (fullerene, C-60) in two aquatic species, Daphnia and fathead minnow. *Mar. Environ. Res.* **2006,** *62*, S5-S9.

(22) Sayes, C. M.; Fortner, J. D.; Guo, W.; Lyon, D.; Boyd, A. M.; Ausman, K. D.; Tao, Y. J.; Sitharaman, B.; Wilson, L. J.; Hughes, J. B.; West, J. L.; Colvin, V. L., The differential cytotoxicity of water-soluble fullerenes. *Nano Lett.* **2004,** *4*, (10), 1881-1887.

Chapter 2: Background and Literature Review

2.1 Photochemical Transformation of CNM Nanoparticles

2.1.1 Photochemical Transformation of Fullerene

Recent studies suggest the photochemical transformation under solar irradiation is an important fate process of nC_{60} in aquatic systems [1-7]. Table 2.1 summarizes reported studies on the photochemical transformation of nC_{60}. Professor Jafvert's group has been actively involved in this topic and contributes most to the literature. Several other groups including our lab have also looked at this issue from different aspects.

Table 2.1. Summary of studies on photochemical transformation of fullerene nanoparticles (nC_{60}).

Ref.	PI	CNM	Light source	Irradiation time (h)	Main findings
1	Jafvert CT 2009	nC_{60}	Sunlight, UVA (300-400 nm)	110 (sunlight), 1560 (UVA)	O_2 is required. Form water soluble intermediates which could be mineralized or volatilized. pH, fulvic acid and the preparation methods have little effects on the transformation.
2	Jafvert CT 2009	nC_{60}	Sunlight, UVA (300-410 nm)	15 (UVA), 21 (sunlight)	nC_{60} produces $^1O_2$ under sunlight or UVA, which in turn oxidizes the $^3C_{60}$. The rate of $^1O_2$ production is a function of cluster size. The water soluble intermediates are photoreactive.
4	Zepp RG 2009	Fullerol	Simulated sunlight, UVA (366 nm)	450 (simulated sunlight), 330	First evidence of mineralization of fullerene derivatives under environmental conditions. O_2 is required. The photoreaction

Ref.	PI	CNM	Light source	Irradiation time (h)	Main findings
				(UVA)	kinetics can be described by biexponential rate expressions. Fullerenol can be fully degraded, while around 47% of the final products can be mineralized. The pH dependence of the photoreaction is attributed to changes in intramolecular hemiketal formation.
8	Kim JH 2009	nC_{60}	UVC (254 nm)	110	Photochemical transformation was achieved through oxidative pathway without carbon mineralization as reflected by the need for oxygen and negligible loss of TOC. Water soluble products largely maintain a 60 carbon structure, containing various oxygen functional groups such as epoxides and ethers. The products are less toxic to E. coli.
6	Jafvert CT 2010	nC_{60}	Sunlight, visible light (> 400 nm), monochromatic light (436 nm and 366 nm)	947 (sunlight), 35 (Visible light),	Visible light is important for the photochemcial transformation of nC_{60}. The apparent quantum yield at 436 nm is comparable to that at 366 nm. Photoreaction generates water soluble C_{60} derivatives (meanwhile reduce the particle size), most of which retain a 60 atom carbon structure, while have oxygen-containing functional groups (vinyl ether, carbonyl, carboxyl) as well as olefinic carbons after 947 h irradiation by sunlight.
3	Li Q 2010	$nC_{60,}$ fullerol	UVA (300-400 nm)	168 (nC_{60}), 504 (fullerol)	UVA irradiation results in surface oxygenation and hydroxylation. The core of nanoparticles remains intact over 21 days irradiation. Fullerol can be partially mineralized under long-term UVA exposure. Humic acid reduces transformation kinetics by scavenging ROS. Oxidized nC_{60} can't be fully extracted by

Ref.	PI	CNM	Light source	Irradiation time (h)	Main findings
					toluene.
[7]	Gelca R 2011	nC_{60}	Simulated sunlight	2016	C_{60} breaks down into small water soluble products which contain oxygen and hydrogen atoms.

nC_{60} is able to produce $^1O_2$ in the presence of oxygen and either UVA light (~350 nm [1]) or visible light (436 nm [6]), both within the solar spectrum. The self-generated ROS can react with surface C_{60} and consequently oxidize the nC_{60} surface [2]. Several studies found the presence of dissolved oxygen is indispensable for the transformation, supporting the crucial role of ROS [1, 3, 8]. Visible light (>400 nm) was found to contribute significantly to nC_{60} photochemical transformation [6]. Our group's previous research suggests nC_{60} undergoes surface oxidation under UVA irradiation in a week [3]. During long term sunlight exposure, water soluble intermediates will be generated, which may be partially mineralized [1, 6]. Most of the intermediates after 947 h solar irradiation still maintain the 60 carbon structure, while possess olefinic carbons as well as various oxygen-containing functional groups including vinyl ether, carbonyl and carboxyl groups [6]. However, in another study, in which nC_{60} was irradiated under simulated sunlight for 2016 h (12 weeks), oxidized small molecular weight compounds were found in the suspension, suggesting the 60 carbon structure of the initial intermediates can be further broken down into small pieces [7]. Fullerol, a hydroxylated derivative of C_{60}, has many structural similarities with the intermediates that have 60 carbon structures. Thus, it can be used as a surrogate to study the possible mineralization of nC_{60} in sunlight. Reported studies

show fullerol can be fully degraded but only partially mineralized (47%) by photoreaction under natural conditions [4]. Similar experiments carried out in our lab came to the same conclusion that some 40% of the fullerol can be mineralized under UVA light [3]. There are also several works that studied the transformation of nC_{60} under conditions that likely can be found in water treatment facilities, such as exposure to UVC light and ozone [8, 9]. When exposed to UVC light (254 nm), photochemical transformation of nC_{60} generates water soluble 60 carbon cage products with various oxygen-containing functional groups such as epoxides and ethers in days. No carbon mineralization was found in 30 h [8]. The reaction between nC_{60} and dissolved ozone results in highly oxidized (C:O ~ 2:1), water soluble C_{60} products with repeating hydroxyl and hemiketal functional groups in hours [9]. Although the oxidation conditions are quite different from that in the presence of sunlight, it is still helpful to examine the similarities and differences of these studies.

The experimental conditions of the aforementioned studies vary. However, by carefully comparing their results, some general conclusions can be drawn here: 1) solar irradiation (both UVA and visible light) can induce photochemical transformation of nC_{60}, resulting in oxidized nC_{60} surface and water soluble intermediates; 2) the surface oxidation of nC_{60} takes place first, then some oxidized intermediates will be released from nC_{60} surface and dissolve into the water; 3) oxidized nC_{60} surface comprises a wide range of oxygen-containing functional groups. The intermediates still maintain the 60 carbon structure at first, but will break down into small pieces and eventually be partially mineralized during prolonged solar irradiation.

One of the factors worth special attention is the time scale of the photochemical transformation. Noticeable surface oxidation of nC_{60} will take place in days of solar irradiation. However, the size of nC_{60} does not change within a week [3]. The significant dissolution of intermediates and a corresponding reduction of particle size occur in weeks [6]. Noticeable mineralization most likely takes place in months [1, 3]. The nC_{60} is expected to be oxidized, break down, and eventually be at least partially mineralized after long term exposure to sunlight.

2.1.2 Photochemical Transformation of CNTs

Compared to fullerenes, the information regarding the photochemical transformation of CNTs in nature settings is scarce. Nevertheless, the structural similarities between CNTs and fullerenes imply that it is very likely that similar sunlight-mediated oxidation processes will, to some extent, also occur to CNTs. It was recently reported that the functionalized single-walled carbon nanotubes (SWCNT) (e.g., carboxylated and functionalized with polyethylene oxide groups) produces ROS including $^1O_2$, $O_2\cdot^-$, and ·OH in the presence of sunlight [10, 11], while surfactant stabilized unfunctionalized SWCNTs have no measurable ROS production under similar conditions [11]. Since the ROS is adjacent to the carbon surface, it is reasonable to assume that the CNT surface may be modified by these self-generated ROS. Although little is known about the photochemical transformation of CNTs under solar irradiation, we can gain some insight by carefully extrapolating our knowledge about the photochemical transformation of fullerene as well as the chemical oxidization of CNTs. In this work, our emphasis will be placed on how the surface chemistry evolves in the presence of sunlight.

2.1.3 Characterizing Physicochemical Properties of CNM Nanoparticles

The physicochemical properties of CNM nanoparticles largely control their environmental behavior. Thus careful examination of these properties is crucial for getting an in-depth understanding of nanoparticle mobility and toxicity. Various techniques (summarized in Table 2.2) were employed to explore these changes and further reveal the mechanisms.

2.1.3.1 Particle Size and Morphology

Light scattering methods are often used to determine particle sizes and size distributions. DLS is a commonly used technique to size nanoparticles since it is able to analyze in a fast, in-situ and real-time manner. The DLS technique estimates the hydrodynamic diameter of a particle from the velocity of its Brownian motion by monitoring the fluctuation of scattered light intensity which depends on the particle size. The large particles scatter more light than small ones since the intensity of scattering is proportional to the sixth power of the diameter of the particle. As a result, the intensity-average size of the particles given by DLS is often larger than their number-average size. DLS is also widely used in studying aggregation kinetics of nanoparticles, which will be discussed in detail in section 2.2.2.2.

There are several microscopic techniques available for qualitative analysis of nanoparticles, including optical, electron and scanning-probe microscopies. They provide information about size, shape and morphology of the nanomaterials. The commonly used

microscopic methods are electron scanning electron microscopy (SEM), transmission electron microscopy (TEM), and atomic force microscopy (AFM).

SEM can provide the morphology of nanoparticles with nm resolution. TEM has better resolution than SEM; and it offers selected-area electron diffraction (SAED) which provides information about the crystalline properties of nanoparticles. The major drawback of conventional electron microscopes is their high vacuum working environment. The sample needs to be dehydrated before analysis, which can change the sample properties. Also some SEM samples require coating to make them conductive. Environmental SEM and TEM instruments have been developed to study wet samples. However, they do it at the cost of resolution; and neither of them can provide temporal information about the particle size. AFM is able to measure sample size and morphology in the aqueous phase.

2.1.3.2 Surface Potential Measurement

The surface charge, or surface potential, is one of the most important properties of nanoparticles. The common way to estimate the surface potential is to measure the ζ potential/electrophoretic mobility (EPM) of the nanoparticles. By measuring particle's migration rate in a known electric field, we can get EPM from direct analysis. For spherical particles, EPM values can be converted into ζ potential using Smoluchowski equation [12]. Another way to get surface charge is titration. The total amount of the specific charge can be measured by acid/base titration and subsequently solving the charge balance. The specific surface area is usually determined by the Brunauer-Emmett-

Teller (BET) method. The surface charge (the charge density, C m^{-2}) is the quotient of the specific charge and the specific surface area.

2.1.3.3 Surface Composition and Functionality

XPS is a powerful tool for characterizing the surface chemistry of nanomaterials. It quantitatively measures the elemental composition and chemical state of the existing elements. XPS is a surface technique, which only provides information about the first 3~10 nm depth of the surface [13]. Other than chemical composition, XPS is more and more widely used for exploring the surface functionality of nanomaterials. That can be achieved by either peak deconvolution or chemical derivatization.

Peak deconvolution. The binding energy of the photoelectrons can be influenced by its local chemical environment to some extent. Thus by deconvolution of the XPS peak of a certain element, we can have a qualitative understanding of the functional groups containing this element. Peak deconvolution was used in several studies to quantitatively analyze the surface functionality. However, that might be problematic due to the close binding energy of different species and the limited resolution of XPS.

Chemical derivatization. A newly developed XPS in conjunction with chemical derivatization method is able to quantify the surface functional groups on carbonaceous materials in a more precise and reliable manner [14, 15]. In this method, the targeted oxygen-containing functional group (e.g., carboxyl, hydroxyl, and carbonyl) is selectively tagged with specific derivatizing reagents containing fluorine or nitrogen atoms. After derivatization, the concentration of the tags can be quantified by measuring the surface

fluorine/nitrogen concentration using XPS as fluorine and nitrogen atoms are not present on underivatized CNT surfaces. Then the concentration of the targeted oxygen-containing functional group can be calculated based on its stoichiometrical reactions with the derivatizing reagent. The reactions between the functional groups and the derivatizing reagents are summarized in Figure 2.1.

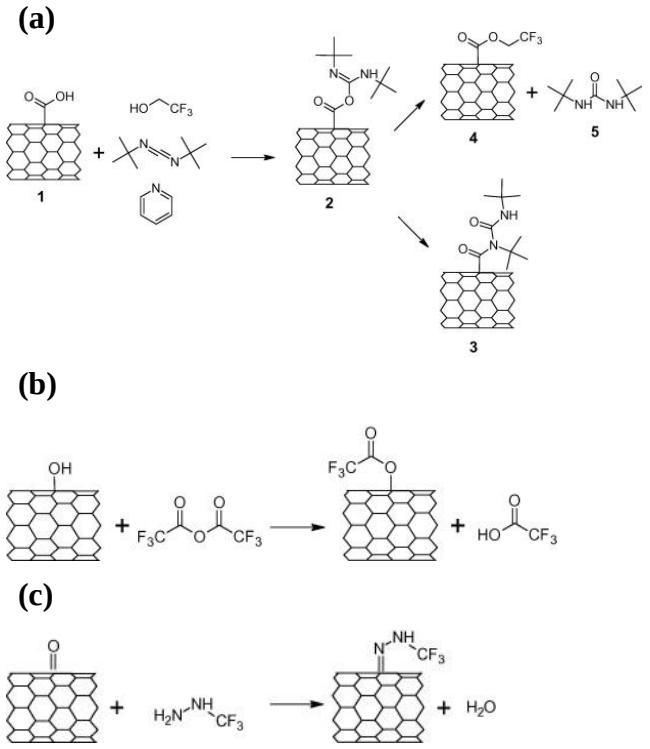

Figure 2.1. The selective reactions of carboxyl groups (COOH) with N,N'-di-*tert*-butyl-carbodiimide and 2,2,2-trifluoroethanol in the presence of pyridine (a); hydroxyl groups (OH) with trifluoroacetic anhydride (b); and carbonyl groups (C=O) with trifluoroethylhydrazine (c). Reprinted from Wepasnick, K. A.; Smith, B. A.; Schrote, K. E.; Wilson, H. K.; Diegelmann, S. R.; Fairbrother, D. H., Surface and structural characterization of multi-walled carbon nanotubes following different oxidative treatments. *Carbon* 2011, 49, (1), 24-36, with permission from Elsevier.

Raman spectroscopy is one of the major methods for the characterization of CNTs. It is generally believed that the D-band (1300~1400 cm^{-1}) in the CNT Raman spectrum is induced by the defect sites and amorphous carbon, while the G-band (1500~1600 cm^{-1})

represents the well-ordered sp^2 graphitic carbons. The ratio of the intensity of these two peaks, I_D/I_G, is usually used as an indicator for the surface detect abundance.

Table 2.2. Particle and surface characterization methods.

Properties	Analytical methods
Size	DLS, TEM
Morphology	TEM
Surface potential	Electrophoretic mobility measurement by phase analysis light scattering
Surface functionality	XPS in conjunction with chemical derivatization, FTIR, Raman spectroscopy

2.2 Environmental Transport of CNM Nanoparticles

Colloidal behavior (e.g., aggregation and deposition) of nanomaterials is a major mechanism that distinguishes their fate, transport and bioavailability compared to molecular or ionic pollutants. The main routes for nanomaterials to be removed from aquatic systems are to aggregate (homoaggregate or heteroaggregate with naturally occurring particles) and subsequently settle down, or deposit on natural surfaces. The aggregation and deposition of CNMs have been extensively studied in recent years [16]. Results of these studies suggest the colloidal behavior of CNMs can be decently described by the traditional Derjaguin-Landau-Verwey-Overbeek (DLVO) theory in

combination with several non-DLVO interactions, i.e., steric hindrance, hydration, hydrophobic forces, bridging, and straining [16, 17]. The colloidal behavior of CNMs are mainly decided by the surface chemistry (e.g., surface potential, surface functional groups, adsorption of macromolecules) of the CNM particles (and the collectors in case of deposition) as well as the solution chemistry (e.g., ionic strength, ion species, organic contents).

2.2.1 Relevant Colloidal Forces and Theories

The size of CNM nanoparticles falls in the range of colloids. Within this size range, the particle-particle and particle-surface interactions are controlled by a set of physical rules which have been studied in colloidal science.

2.2.1.1 DLVO Theory

DLVO theory is the classic theory that describes the interactions between particle and particle/surface. It assumes the total interaction energy experienced by two approaching particles (in the aggregation) or a particle and a surface (in the deposition) can be evaluated by the superposition of two common colloidal forces, van der Waals (VDW) and electrical double layer (EDL) interactions. The resulting total interaction energy (V_T) decides the stability of the particles.

$$V_T = V_{VDW} + V_{EDL} \tag{2-1}$$

Figure 2.2 is a typical interaction energy profile between two approaching particles.

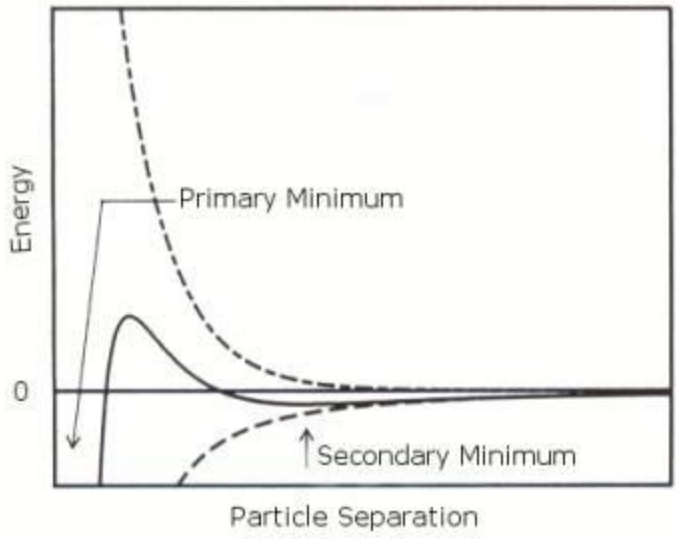

Figure 2.2. A typical interaction energy profile between two approaching particles.

At the vicinity of the particle surface, V_{VDW} increases drastically to form a deep attractive well, the primary minimum. A secondary minimum is located at farther distance with a much shallow shape. Studies suggested that DLVO theory alone cannot explain the colloidal behavior of many systems. In these cases, the non-DLVO forces should be taken into account.

2.2.1.2 Non-DLVO Forces

The non-DLVO forces include hydration force, hydrophobic interaction, steric effects, and bridging.

Hydration force. The hydration force is a strong short-range (normally < 5nm) repulsive force that decays exponentially with the distance. It stems from the change of hydration layer of the particle surface. Particles in water are surrounded by several layers

of water molecules which are commonly believed to have different structure from that in the bulk phase. In order for the particles to come into direct contact, the surfaces need to be dehydrated, which costs work and increases the free energy of the system.

Hydrophobic interaction. Water is a polar solvent and has little affinity to hydrophobic surfaces. The orientation of water molecules near hydrophobic surfaces is entropically unfavorable. When these water molecules are expelled into the bulk, the free energy of the system is reduced accordingly. Thus the hydrophobic surfaces tend to attract each other in water, which we usually refer to as hydrophobic interaction. Hydrophobic interaction has a much longer interaction range than hydration force, up to about 80 nm [18].

Steric effects. When adsorbed onto particle surface, polymers and many other macromolecules can stabilize particles mainly through steric effects. Steric effects arise from the displacement of the associated water during the interpenetration of the hydrophilic parts of the polymers that stretch into the solution when particles approach each other. This process increases the free energy, thus hinders the attachment. The intensity of steric effects is decided by several factors including the surface coverage, the molecular weight and conformation of the polymer, and the solubility of the polymer component stretching into solution.

Bridging. When the particle surface is only partially covered by the polymer, in some cases, the polymers can interconnect particles, resulting in higher aggregation.

2.2.1.3 Schulze-Hardy Rule

The Schulze-Hardy rule suggests the colloidal stability strongly depends on the counter-ion valence, z. Cations of higher valence are more efficient in coagulation. It can be expressed as:

$$ccc \propto \frac{1}{z^n} \quad (2\text{-}2)$$

Where CCC is the critical coagulation concentration, n = 6 for particles with high potentials, and n=2 for particles with low potentials [19].

2.2.2 Experimental and Theoretical Approaches to Study Nanoparticle Aggregation and Deposition

2.2.2.1 Sedimentation Experiment

Sedimentation refers to the process of particles in suspension gravitationally settling out of the aqueous phase. During the sedimentation experiment, the change of nanoparticle concentration in aqueous phase is monitored using a UV-vis or turbidity spectrometer. Sedimentation experiment results can be used to qualitatively compare the stability of different nanoparticles or nanoparticles in different solution chemistry. The sedimentation rate is decided by the particle size, shape, and concentration.

2.2.2.2 Aggregation Behavior

Dynamic light scattering technique (DLS)

DLS is the most commonly employed method to study the aggregation of nanoparticles. It can provide us the information about hydrodynamic particle size (average size and size distribution) as a function of time, *in situ*. The initial aggregation rate, i.e., the initial increase rate of the intensity weighted mean hydrodynamic radius $a_h(t)$, is proportional to the primary particle concentration N_0 and the aggregation rate constant k:

$$\left(\frac{da_h(t)}{dt}\right)_{t\to 0} \propto kN_0 \tag{2-3}$$

The value of $\left(\frac{da_h(t)}{dt}\right)_{t\to 0}$ was determined by applying linear least square regression analysis to the initial phase of the aggregation curve (i.e., hydrodynamic radius as a function of time).

The attachment efficiency α (the inverse of the stability ratio W) is defined as the aggregation rate constant in the solution of interest normalized by the rate constant in the diffusion-limited regime, where the aggregation rate constant is independent of electrolyte concentration:

$$\alpha = \frac{k}{(k)_{\text{fast}}} = \frac{\frac{1}{N_0}\left(\frac{\mathrm{d}a_h(t)}{\mathrm{d}t}\right)_{t\to 0}}{\frac{1}{(N_0)_{\text{fast}}}\left(\frac{\mathrm{d}a_h(t)}{\mathrm{d}t}\right)_{t\to 0,\text{fast}}} \tag{2-4}$$

In equation 2-4, the subscript “fast” denotes diffusion-limited aggregation conditions. At low electrolyte concentrations, only a fraction of the collisions leads to aggregation due to the presence of an energy barrier, i.e., α is less than one. The energy barrier is suppressed due to electric double layer compression at higher electrolyte concentrations

and is eliminated if the electrolyte concentration surpasses the critical coagulation concentration (CCC), i.e., the diffusion-limited regime. In the diffusion-limited regime, α equals one. The α value was used to describe the stability of nanoparticles in different solution chemistries. Because all samples used in DLS measurements had the same nC_{60} concentration, i.e., N_0 equals $(N_0)_{fast}$, α was calculated by equation 2-5.

$$\alpha = \frac{\left(\frac{da_h(t)}{dt}\right)_{t\to 0}}{\left(\frac{da_h(t)}{dt}\right)_{t\to 0,\text{fast}}} \tag{2-5}$$

$\left(\frac{da_h(t)}{dt}\right)_{t\to 0,\text{fast}}$ was the average of the initial slopes of all aggregation kinetic curves obtained in the diffusion-limited regime, i.e., aggregation rate independent of electrolyte concentration. Stability curves were constructed by plotting the α value as a function of the background electrolyte concentration. The critical coagulation concentration (CCC) was approximated by the electrolyte concentration at the intersection of the reaction-limited stability curve (extrapolated from the linear section of the actual stability curve) and the diffusion-limited stability curve (constant α value). The CCC value serves as a quantitative metric to compare nanomaterial colloidal stability in various solution chemistries.

2.2.2.3 Deposition Behavior

a. Packed-bed column technique

The lab-scale packed-bed column is the most commonly used approach to study colloid transport in porous media. Particle removal in a packed-bed column is evaluated

by monitoring the effluent particle concentration as a function of time using UV-vis spectroscopy.

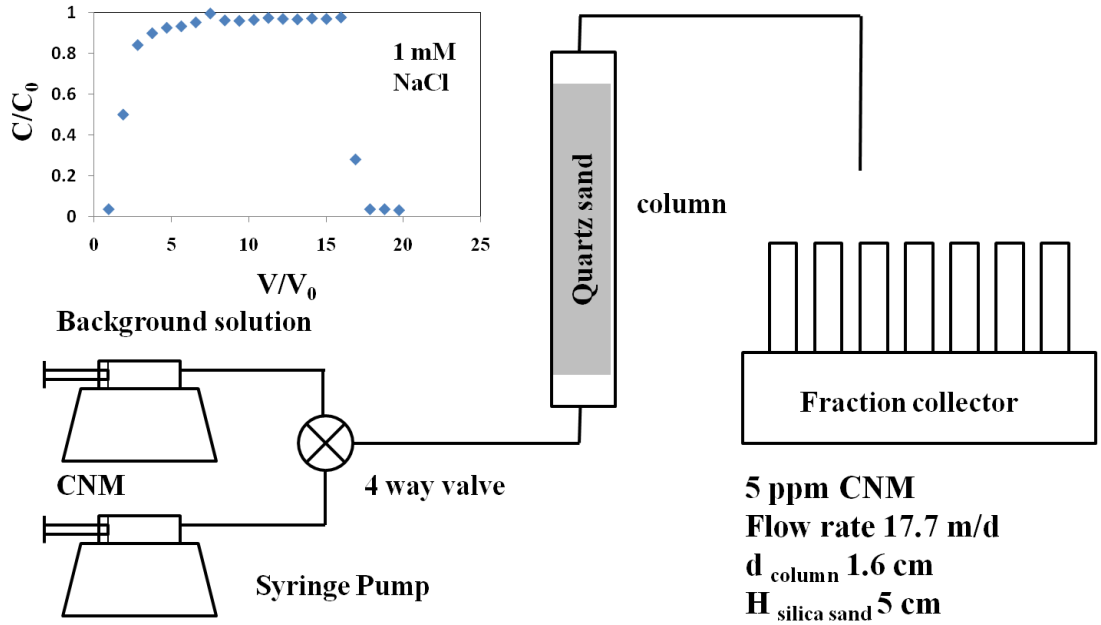

Figure 2.3. Column experiment setup and representative breakthrough curve.

The CNM attachment efficiency can be calculated using colloid filtration theory (CFT) [20]:

$$\alpha = -\frac{2d_c}{3(1-\varepsilon)\eta_0 L}\ln\frac{C}{C_0} \quad (2\text{-}6)$$

Where d_c is the collector diameter, ε is the porosity, η_0 is the single-collector contact efficiency, L is the length of the column, C and C_0 are the influent and effluent particle concentration,

The single-collector contact efficiency η_0 can be determined using a correlation equation developed by Tufenkji and Elimelech based on the numerical solution of the convective-diffusion equation [21]:

$$\eta_0 = 2.4A_s^{1/3}N_R^{-0.081}N_{Pe}^{-0.715}N_{vdW}^{0.052} + 0.55A_sN_R^{1.675}N_A^{0.125} + 0.22N_R^{-0.24}N_G^{1.11}N_{vdW}^{0.053} \quad (2\text{-}7)$$

Where A_s is a porosity-dependent parameter, N_R is the aspect ratio, N_{Pe} is the Peclet number, N_{vdw} is the van der Waals number, N_A is the attraction number, N_G is the gravity number.

Equation 2-7 was derived from mass balance in one-dimensional flow in a packed-bed column when advection is the main transport mechanism. Due to the extreme small particle size of nC_{60} and slow flow velocity in the column which simulates the slow groundwater flow in the subsurface, transport of nC_{60} nanoparticles can be diffusion dominated. Equation 2-7 may not be adequate to describe the transport behavior of nC_{60}. Additionally the breakthrough curve will be fitted to advective-diffusion equation to get the particle deposition rate coefficient, assuming the particle removal can be represented by first-order kinetics. The attachment efficiency will then be determined by normalizing the particle deposition rate coefficient to that under favorable conditions:

$$C_{(x)} = C_0 \exp\left[-\frac{k_d}{v}x\right] \quad (2\text{-}8)$$

$$k_d = -\frac{U}{\varepsilon L}\ln\left(\frac{C}{C_0}\right) \quad (2\text{-}9)$$

$$\alpha = \frac{k_d}{k_{d,favorable}} \quad (2\text{-}10)$$

Favorable deposition conditions can be achieved by reversing the surface charge of the collector, such that the particles and collectors are oppositely charged. The collectors will be treated with pol-L-lysine (PLL) or aminosilane to impart a net positive charge.

b. Quartz Crystal Microbalance (QCM) system

QCM is widely used in studies of biopolymer adsorption/desorption kinetics and has been recently used to study nanoparticle deposition kinetics. Compared to packed-bed column experiment, QCM can provide in-situ, real time information about CNM deposition on bare or coated silica surface which simulates the sand surface.

CNM mass transfer rate in QCM

During the period of deposition, the CNM nanoparticles are stable at low ionic strength, while undergo aggregation at higher ionic strength. Thus at high ionic strength the mass transfer rate will decrease due to the increase of particle size caused by aggregation and consequent decrease of diffusion coefficient as described by the Stokes-Einstein equation.

$$D_{AB} = \frac{kT}{f} = \frac{kT}{3\pi\mu d} \tag{2-11}$$

Where D_{AB} refers to the diffusion coefficient, f is the friction factor, k is the Boltzman constant, T is the absolute temperature, μ is the absolute viscosity, and d is the particle diameter.

The mass transport rate can be acquired by theoretical and experimental approaches

(I) Theoretical calculation

It was reported that the Smoluchowski-Levich approximation for parallel-plate geometry can be used to estimate the particle transfer rate for QCM system [22]:

$$r = 0.560 \frac{DC}{a} \left(\frac{Pe}{L}\right)^{1/3} \quad (2\text{-}12)$$

Where r is the mass transfer rate, D is the diffusion coefficient, C is the number concentration, a is the radius of particle based on DLS measurement, Pe is the Peclet number, L is the average distance along the flow from the inlet to the outlet.

Since the geometry of QCM flow chamber isn't precisely a parallel-plate system, equation 2-12 may not be adequate to predict the mass transfer rate in QCM.

(II) Experimental approach

The deposition kinetics under favorable conditions indicates the mass transfer rate of CNM towards sand surface in a given solution chemistry. Deposition rates of CNM on PLL-coated silica surface are only controlled by diffusion since the attachment efficiency under favorable conditions is assumed to be unity.

c. Correlation between data from column and QCM systems.

Previously, nC_{60} deposition onto bare sand surface has been studied in both column and QCM systems and the results are qualitatively consistent. Since the hydrodynamic conditions and solution chemistry in each system or study differed, quantitative comparisons were not available. By employing similar hydrodynamic conditions which

are accessed by Peclet number, attachment efficiencies from these two approaches will be quantitatively compared. Potential correlation will be investigated to connect the results from column and QCM systems.

For column system (sphere in uniform flow):

$$P_{e\ column} = \frac{3A_f V a^3}{R^2 D} \quad (2\text{-}13)$$

$$A_f = \frac{3}{2}\left[1 + \frac{0.19R_e}{1+0.25R_e^{0.56}}\right] \quad (2\text{-}14)^{23}$$

For QCM-D system (parallel-plate channel):

$$P_{e\ QCM} = \frac{3Va^3}{2b^2 D} \quad (2\text{-}15)^{19}$$

2.2.4 The Aggregation Behavior of CNMs

The aggregation behavior of CNMs has been extensively studied in recent years. And most of results have been carefully summarized by two reviews [13, 16]. Generally, the DLVO theory can at least qualitatively capture the CNM aggregation pattern. Although many non-DLVO forces were also found to play an important role in the CNM aggregation, it is always convenient to use DLVO theory as a starting point for data analysis. Two types of interactions, van der Waals force and electrostatic force, need to be taken into consideration within the framework of DLVO theory. The most important parameter that decides the van der Waals force is the Hamaker constant (6.7×10^{-21} J for nC_{60} in water [24]), which is a material property (size, composition, and geometry) and

rather stable in most cases. As a result, electrostatic force is the key factor that controls particle aggregation as solution chemistry varies.

The aggregation of CNMs in different ionic strength is the fundamental behavior that influences their environmental mobility. The surface potential of CNMs as reflected by the EPM or surface charge density becomes less negative as the ionic strength increases. Consequently, the CNM nanoparticles will be destabilized due to the reduced electrostatic repulsion. In terms of predictive metrics, the surface charge density can well describe the CNT aggregation propensity. On the other hand, the EPM is not a good metric for CNT stability as it only reflects the surface charge density at the shear layer which can be affected by the associated water and the counterions [25, 26].

For CNMs with high concentration of surface oxygen functional groups (e.g., oxidized CNTs and nC_{60}), the solution pH can strongly affect their stability by controlling the dissociation of functional groups. At high pH conditions, the deprotonation of carboxyl groups will lead to higher surface potential and more hydrophilic surface, resulting in higher repulsion forces. Thus oxidized MWCNTs (OMWCNTs) and nC_{60} (both sonicated and stirred) are more stable at high pH [25, 27]. OMWCNTs can be dispersed in aqueous phase at pH > 4 [28] or 5 [29], while they precipitate at lower pH. Several papers studied the influence of pH on nC_{60} stability with the aim to gain further understanding of the origin of nC_{60} surface charge [27]. nC_{60} produced by sonication, solvent exchange, and stirring all exhibit higher EPM at high pH in monovalent electrolytes [27, 30], indicating that the negative surface charge of nC_{60} at least partially came from the surface functional groups.

The electrolyte species are of great importance for the aggregation process. As stated in the Schulze-Hardy rule, cations with higher valence are expected to more efficiently coagulate CNM nanoparticles. Two studies have focused on the role of electrolyte species and the applicability of Schulze-Hardy rule for fullerene nanoparticles and carbon nanotubes, respectively [31, 32]. The reciprocal CCC of nC_{60} for cation charges z=1, 2, and 3 are related as 1:20:1500 [32]. Thus the *n* in the Schulze-Hardy rule (equation 2-2) will be 4.3~6.6 for nC_{60}. For carbon nanotubes, the *n* is around 6 [31]. Another study found the CCC of different cations for tannic acid stabilized MWCNT exponentially correlated to ionic valence [29]. These *n* values lie in the upper range of the prediction for Schulze-Hardy rule (the *n* is predicted to be 6 for particles with high surface charge, and 2 for particles with low surface charge [19]). Hydroxyfullerene, which is usually referred to as fullerol, was found to act as a chelate ligand to the metals. Metal ions can induce precipitation of dissolved fullerol, leading in its removal from the aqueous phase [33]. Organic electrolytes (e.g. Methylene Blue chloride, cetyltrimethylammonium bromide) were also able to destabilize nC_{60} [32]. However, an excess of cetyltrimethylammonium bromide was found to stabilize nC_{60} due to the hydrophilic second adsorbed layer.

NOM is one of the key factors governing the fate and transport of colloids in the environment. Ubiquitous in the aquatic systems and soils, NOM is known to electrosterically stabilize colloid particles and greatly enhance their mobility. NOM can readily adsorb onto CNM surface via hydrophobic forces and stabilize both nC_{60} and CNT nanoparticles, even at very high ionic strength (several hundred mM IS) [29, 34-37]. In such conditions, the surface charge of the CNM nanoparticles is likely to be effectively screened, suggesting the steric effect is the main stabilization mechanism. Other

macromolecules, such as protein (bovine serum albumin (BSA)), cell culture medium (Luria-Bertani (LB)), and polysaccharide (alginate), also can stabilize CNT in the similar fashion [37]. BSA was most efficient in stabilizing CNT as its globular structure can provide higher steric effect. Polymer (polyvinyl pyrrolidone (PVP)) and surfactant (sodium dodecyl sulfate (SDS)) were also found to stabilize nC_{60} [32]. However, in the presence of high concentration of Ca^{2+}, bridging effect took place between humic acid coated nC_{60}, facilitating the aggregation, and causing attachment efficiency higher than unity [34].

The surface chemistry of the CNM nanoparticles is the pivot for their colloidal behavior. It is also the most common origin of the discrepancy between different works. The common methods to make nC_{60} suspension are solvent exchange, sonication (or solvent exchange and sonication), and prolonged stirring. nC_{60} prepared using these techniques have different surface chemistry. Prolonged stirring in water imparted oxygen onto the nC_{60} nanoparticle surface [27]. Due to the surface oxidation, stirred nC_{60} normally has a higher surface potential and thus is more stable in aqueous phase. Bulky functional groups such as phenyl alkyl ester moieties on the nC_{60} surface were found to impede the aggregation process through steric effect [38]. For CNTs, the CCC, total oxygen concentration, and surface charge are linearly correlated [26]. Among all the functional groups on acid oxidized carbon nanotubes, carboxyl groups play the most important role in the aggregation behavior [26]. MWCNTs with higher carboxyl group content were found to form a denser aggregate [28]. CNT with higher surface oxygen content are more stable in NaCl solutions. However, in $CaCl_2$ solutions, the OMWCNT with different surface oxygen concentration exhibit similar aggregation behavior [39]. This was attributed to the

fact that Ca cations have a higher affinity to form complexes with adjacent carboxyl groups on high-oxygen OMWCNT (10.6% O) surface than with isolated carboxyl groups on low-oxygen OMWCNT (6.3% O) surface.

2.2.5 The Deposition Behavior of CNMs

To date, there are twelve papers in the literature reporting the deposition behavior of fullerene nanoparticles [24, 40-50]. Professors Wiesner, Chen, Elimelech, Pennell, and Bouchard are the major investigators on this topic. These studies suggest that the physicochemical properties of nanoparticles (surface potential, surface functional groups) and the collectors (size, surface potential), the solution chemistry (ionic strength, ion species, organic contents), and the hydraulic conditions (Darcy velocity) are the major factors governing the deposition process. The deposition of nC_{60} is qualitatively in good agreement with the classic DLVO theory and mostly happens in primary minimum [47]. The ionic strength is one of the most often tested variables. The deposition of nC_{60} increases with increasing ionic strength due to the charge screening. The influence of ionic strength is usually consistent with the change of nanoparticle surface potential. Ionic strength screens the surface charge of nC_{60}, resulting in lower ζ potential or EPM and subsequently weaker electrostatic repulsion. Multivalent ions (e.g., Mg^{2+}, Ca^{2+}) are much more efficient in screening the surface charge of nanoparticles as suggested by the Schulze-Hardy rule. One study reported charge reversal of nC_{60} in low concentrations of $CaCl_2$ [30]. However, another study showed that nC_{60} remained negatively charged over the same range of $CaCl_2$ concentrations [47]. Jaisi et al. suggested the deposition of SWCNT is less reversible in $CaCl_2$ than in KCl solutions [51].

The mechanisms that control CNT deposition are different from nC_{60} to some extent due to the large aspect ratio of the nanotubes. Straining effect was identified as a major retention mechanism in several cases [48, 51]. The straining means the nanoparticles are stuck at the adjunctions between the porous media. The extent of straining is decided by both the size of the nanoparticles and the collectors. It usually takes place when the ratio of the particle to the collector diameters is greater than 0.003 [52].

The influence of macromolecules on nC_{60} deposition process was investigated by Wiesner [43] and Chen and Elimelech [44]. The macromolecules tested included humic acid, tannic acid and alginate. Humic acid, even at low concentrations (1 mg/L TOC) can significantly reduce the attachment of nC_{60} mainly due to the steric hindrance forces [44]. The humic acid was also found to facilitate the transport of CNTs in porous media [51, 53]. Tannic acid, a common surrogate of humic acid, also has similar effect [43]. The influence of alginate is still debatable. Espinasse et al. showed that the presence of alginate at a concentration of 2 mg/L facilitates nC_{60} deposition, which can be attributed to the destabilizing effect of alginate on nC_{60} nanoparticles [43]. Another study suggested 1 mg/L TOC alginate can efficiently slow the deposition kinetics, similar to humic acid [44]. Other than dissolved macromolecules, the influence of surface immobilized macromolecules (humic acid, alginate, and extracellular polymeric substance (EPS)) was also studies by two groups [44, 49]. Surface immobilized humic acid was found to retard nC_{60} deposition through steric repulsion [44]. Surface immobilized alginate provided steric repulsion and meanwhile increased the surface roughness of collector surface; thus it could lead to both lower and higher attachment [44]. Surface immobilized EPS enhanced the deposition of nC_{60}, presumably due to attractive interactions between EPS and nC_{60} as well as the

increased surface roughness [49]. The controversial results from different studies suggest that the influence of dissolved and surface immobilized macromolecules is still inconclusive; further investigation is necessary to gain more insight into the mechanisms.

The flow rate can sometimes lead to different retention of CNM nanoparticles in porous media. Lecoanet et al. found nC_{60} retention at two flow rates (34.56 m/d and 120.96 m/d) were similar, suggesting the time scale of attachment is greater than that of mass transport [41]. Another study carried out by Espinasse et al. suggested the retention of nC_{60} is lower at 103.68 m/d than 34.56 m/d [43]. The mobility of MWCNT was found to be constant at flow rate higher than 4 m/d, but decreased at 0.42 m/d [54].

The deposition behavior of CNMs also strongly depends on their physicochemical properties. The CNMs nanoparticles with higher surface charge or surface oxygen concentration tend to be more stable in the aqueous phase. nC_{60} with more surface oxygen is more stable against deposition due to the higher surface potential and hydrophilicity [50]. Similar to the aggregation behavior, CNT with high surface oxygen content is more stable in NaCl solutions, but as stable as CNT with low surface oxygen content in $CaCl_2$ solutions, which is attributed to the strong affinity between Ca cation and adjacent carboxyl groups on MWCNT with high surface oxygen content [39].

2.3 Toxicity of CNM Nanoparticles

Evidence from the literature suggested that CNMs pose toxicity to various organisms such as microorganisms (e.g., bacteria [55-62], algae [63-65] protozoa [66, 67] and fungi [68]), aquatic invertebrates (e.g., daphnia) and vertebrates (e.g., fish) [69], and human cell lines [70], raising

concerns regarding their adverse impact to human health and ecological systems. This work focuses on the toxicity of CNMs toward bacteria.

2.3.1 Toxicity of Fullerene Nanoparticles

Reports of the toxicity of fullerene nanoparticles have been inconsistent. The early reported toxic effect of nC_{60} partially stemed from trace amounts of tetrahydrofuran (THF) intermediate solvent and its byproducts [71-73]. After eliminating the influence of toxic solvent, nC_{60} was found to be only mild toxic to bacteria. Initial studies postulated that reactive oxygen species (ROS) generation is one of the major toxicity mechanisms involved [74, 75]. However, reports on the ROS generation of nC_{60} were contradictory. Several studies reported minimal to no ROS production by aqueous nC_{60} due to self-quenching [76, 77]. Thus it has been suggested that the toxicity of nC_{60} stems from ROS-independent oxidative stress [78, 79].

2.3.2 Toxicity of CNTs

Recent studies suggested that CNTs are cytotoxic to bactria, with SWCNTs exhibiting the strongest antimicrobial activity [56]. The early investigation showed physical membrane perturbation is one of the major toxicity mechanisms [57, 62, 80]. As a result, direct contact between CNT and bactria is required for inactivation. NOM reduces the bacterial attachment, but does not mitigate toxicity toward attached cells [56]. Later on, oxidative stress was identified as another toxicity mechanism as suggested by the high level of oxidative stress-related gene expression [62]. However, another study concluded oxidative stress doesn't play an important role in the antimicrobial activity due to small

oxidative potential of SWCNTs [80]. The antimicrobial mechanism of CNTs is not completely understood. Studies have shown that the physicochemical properties of CNTs have great influence on its cytotoxicity [55, 58, 62, 80]. SWCNTs exhibit much higher toxicity than MWCNTs due to their smaller diameter [62]. For MWCNTs, a correlation between bacterial cytotoxicity and physicochemical properties that enhance MWCNT-cell contact opportunities was found [55]. The authors suggested that nanotubes with higher toxicity are uncapped, debundled, short, and dispersed in solution. The effect of length on the CNT toxicity is still controversial. Short MWCNTs and SWCNTs were reported to possess higher toxicity [55, 80]. However, one study suggested longer SWCNTs are more toxic than the shorter one [61]. Metallic SWCNTs have higher toxicity than the semiconducting SWCNTs [58].

Based on these studies of CNT cytotoxicity, it was recently reported that the cytotoxicity of CNTs can be generally explained by a three-step mechanism: (1) Direct contact between CNTs and bacteria; (2) Cell membrane perturbation; and (3) Disruption of a specific microbial process via disturbing/oxidizing a vital cellular structure/component [58]. Another study suggested this mechanism is also applicable to graphene-based materials (i.e., graphite, graphite oxide, graphene oxide and reduced graphene oxide) [81].

2.4 References

(1) Hou, W. C.; Jafvert, C. T., Photochemical Transformation of Aqueous C(60) Clusters in Sunlight. *Environ. Sci. Technol.* **2009,** *43*, (2), 362-367.

(2) Hou, W. C.; Jafvert, C. T., Photochemistry of Aqueous C(60) Clusters: Evidence of (1)O(2) Formation and its Role in Mediating C(60) Phototransformation. *Environ. Sci. Technol.* **2009,** *43*, (14), 5257-5262.

(3) Hwang, Y. S.; Li, Q. L., Characterizing Photochemical Transformation of Aqueous nC(60) under Environmentally Relevant Conditions. *Environ. Sci. Technol.* **2010,** *44*, (8), 3008-3013.

(4) Kong, L. J.; Tedrow, O.; Chan, Y. F.; Zepp, R. G., Light-Initiated Transformations of Fullerenol in Aqueous Media. *Environ. Sci. Technol.* **2009,** *43*, (24), 9155-9160.

(5) Li, Q. L.; Xie, B.; Hwang, Y. S.; Xu, Y. J., Kinetics of C(60) Fullerene Dispersion in Water Enhanced by Natural Organic Matter and Sunlight. *Environ. Sci. Technol.* **2009,** *43*, (10), 3574-3579.

(6) Hou, W. C.; Kong, L. J.; Wepasnick, K. A.; Zepp, R. G.; Fairbrother, D. H.; Jafvert, C. T., Photochemistry of Aqueous C(60) Clusters: Wavelength Dependency and Product Characterization. *Environ. Sci. Technol.* **2010,** *44*, (21), 8121-8127.

(7) Gelca, R.; Surowiec, K.; Anderson, T. A.; Cox, S. B., Photolytic Breakdown of Fullerene C(60) Cages in an Aqueous Suspension. *J. Nanosci. Nanotechnol.* **2011,** *11*, (2), 1225-1229.

(8) Lee, J.; Cho, M.; Fortner, J. D.; Hughes, J. B.; Kim, J. H., Transformation of Aggregate C(60) in the Aqueous Phase by UV Irradiation. *Environ. Sci. Technol.* **2009,** *43*, (13), 4878-4883.

(9) Fortner, J. D.; Kim, D. I.; Boyd, A. M.; Falkner, J. C.; Moran, S.; Colvin, V. L.; Hughes, J. B.; Kim, J. H., Reaction of Water-Stable C-60 aggregates with ozone. *Environ. Sci. Technol.* **2007,** *41*, (21), 7497-7502.

(10) Chen, C. Y.; Jafvert, C. T., Photoreactivity of Carboxylated Single-Walled Carbon Nanotubes in Sunlight: Reactive Oxygen Species Production in Water. *Environ. Sci. Technol.* **2010,** *44*, (17), 6674-6679.

(11) Chen, C. Y.; Jafvert, C. T., The role of surface functionalization in the solar light-induced production of reactive oxygen species by single-walled carbon nanotubes in water. *Carbon* **2011,** *49*, (15), 5099-5106.

(12) Smoluchowski, M., Contributiona la théorie de l'endosmose électrique et de quelques phenomenes corrélatifs. *Bull. Intl Acad. Sci. Cracovie* **1903,** *8*, 182-200.

(13) Chen, K. L.; Smith, B. A.; Ball, W. P.; Fairbrother, D. H., Assessing the colloidal properties of engineered nanoparticles in water: case studies from fullerene C(60) nanoparticles and carbon nanotubes. *Environ. Chem.* **2010,** *7*, (1), 10-27.

(14) Langley, L. A.; Fairbrother, D. H., Effect of wet chemical treatments on the distribution of surface oxides on carbonaceous materials. *Carbon* **2007,** *45*, (1), 47-54.

(15) Langley, L. A.; Villanueva, D. E.; Fairbrother, D. H., Quantification of surface oxides on carbonaceous materials. *Chem. Mat.* **2006,** *18*, (1), 169-178.

(16) Petosa, A. R.; Jaisi, D. P.; Quevedo, I. R.; Elimelech, M.; Tufenkji, N., Aggregation and Deposition of Engineered Nanomaterials in Aquatic Environments: Role of Physicochemical Interactions. *Environ. Sci. Technol.* **2010,** *44*, (17), 6532-6549.

(17) Petersen, E. J.; Zhang, L. W.; Mattison, N. T.; O'Carroll, D. M.; Whelton, A. J.; Uddin, N.; Nguyen, T.; Huang, Q. G.; Henry, T. B.; Holbrook, R. D.; Chen, K. L., Potential Release Pathways, Environmental Fate, And Ecological Risks of Carbon Nanotubes. *Environ. Sci. Technol.* **2011,** *45*, (23), 9837-9856.

(18) Claesson, P. M.; Christenson, H. K., VERY LONG-RANGE ATTRACTIVE FORCES BETWEEN UNCHARGED HYDROCARBON AND FLUOROCARBON SURFACES IN WATER. *J. Phys. Chem.* **1988,** *92*, (6), 1650-1655.

(19) Elimelech, M.; Gregory, J.; Jia, X.; Williams, R. A., Particle Deposition and Aggregation: Measurement, Modelling and Simulation. *Oxford, UK* **1995**.

(20) Yao, K. M.; Habibian, M. M.; Omelia, C. R., WATER AND WASTE WATER FILTRATION - CONCEPTS AND APPLICATIONS. *Environ. Sci. Technol.* **1971,** *5*, (11), 1105-&.

(21) Tufenkji, N.; Elimelech, M., Correlation equation for predicting single-collector efficiency in physicochemical filtration in saturated porous media. *Environ. Sci. Technol.* **2004,** *38*, (2), 529-536.

(22) Quevedo, I. R.; Tufenkji, N., Influence of Solution Chemistry on the Deposition and Detachment Kinetics of a CdTe Quantum Dot Examined Using a Quartz Crystal Microbalance. *Environ. Sci. Technol.* **2009,** *43*, (9), 3176-3182.

(23) Adamczyk, Z.; Warszynski, P.; Szyk-Warszynska, L.; Weronski, P., Role of convection in particle deposition at solid surfaces. *Colloid Surf. A-Physicochem. Eng. Asp.* **2000,** *165*, (1-3), 157-187.

(24) Chen, K. L.; Elimelech, M., Aggregation and deposition kinetics of fullerene (C-60) nanoparticles. *Langmuir* **2006,** *22*, (26), 10994-11001.

(25) Smith, B.; Wepasnick, K.; Schrote, K. E.; Bertele, A. H.; Ball, W. P.; O'Melia, C.; Fairbrother, D. H., Colloidal Properties of Aqueous Suspensions of Acid-Treated, Multi-Walled Carbon Nanotubes. *Environ. Sci. Technol.* **2009,** *43*, (3), 819-825.

(26) Smith, B.; Wepasnick, K.; Schrote, K. E.; Cho, H. H.; Ball, W. P.; Fairbrother, D. H., Influence of Surface Oxides on the Colloidal Stability of Multi-Walled Carbon Nanotubes: A Structure-Property Relationship. *Langmuir* **2009,** *25*, (17), 9767-9776.

(27) Chen, K. L.; Elimelech, M., Relating Colloidal Stability of Fullerene (C(60)) Nanoparticles to Nanoparticle Charge and Electrokinetic Properties. *Environ. Sci. Technol.* **2009,** *43*, (19), 7270-7276.

(28) Shieh, Y. T.; Liu, G. L.; Wu, H. H.; Lee, C. C., Effects of polarity and pH on the solubility of acid-treated carbon nanotubes in different media. *Carbon* **2007,** *45*, (9), 1880-1890.

(29) Lin, D. H.; Liu, N.; Yang, K.; Zhu, L. Z.; Xu, Y.; Xing, B. S., The effect of ionic strength and pH on the stability of tannic acid-facilitated carbon nanotube suspensions. *Carbon* **2009,** *47*, (12), 2875-2882.

(30) Brant, J.; Lecoanet, H.; Hotze, M.; Wiesner, M., Comparison of electrokinetic properties of colloidal fullerenes (n-C-60) formed using two procedures. *Environ. Sci. Technol.* **2005,** *39*, (17), 6343-6351.

(31) Sano, M.; Okamura, J.; Shinkai, S., Colloidal nature of single-walled carbon nanotubes in electrolyte solution: The Schulze-Hardy rule. *Langmuir* **2001,** *17*, (22), 7172-7173.

(32) McHedlov-Petrossyan, N. O.; Klochkov, V. K.; Andrievsky, G. V., Colloidal dispersions of fullerene C-60 in water: some properties and regularities of coagulation by electrolytes. *J. Chem. Soc.-Faraday Trans.* **1997,** *93*, (24), 4343-4346.

(33) Anderson, R.; Barron, A. R., Reaction of hydroxyfullerene with metal salts: A route to remediation and immobilization. *J. Am. Chem. Soc.* **2005,** *127*, (30), 10458-10459.

(34) Chen, K. L.; Elimelech, M., Influence of humic acid on the aggregation kinetics of fullerene (C-60) nanoparticles in monovalent and divalent electrolyte solutions. *J. Colloid Interface Sci.* **2007,** *309*, (1), 126-134.

(35) Hyung, H.; Fortner, J. D.; Hughes, J. B.; Kim, J. H., Natural organic matter stabilizes carbon nanotubes in the aqueous phase. *Environ. Sci. Technol.* **2007,** *41*, (1), 179-184.

(36) Saleh, N. B.; Pfefferle, L. D.; Elimelech, M., Aggregation Kinetics of Multiwalled Carbon Nanotubes in Aquatic Systems: Measurements and Environmental Implications. *Environ. Sci. Technol.* **2008,** *42*, (21), 7963-7969.

(37) Saleh, N. B.; Pfefferle, L. D.; Elimelech, M., Influence of Biomacromolecules and Humic Acid on the Aggregation Kinetics of Single-Walled Carbon Nanotubes. *Environ. Sci. Technol.* **2010,** *44*, (7), 2412-2418.

(38) Bouchard, D.; Ma, X.; Issacson, C., Colloidal Properties of Aqueous Fullerenes: Isoelectric Points and Aggregation Kinetics of C(60) and C(60) Derivatives. *Environ. Sci. Technol.* **2009,** *43*, (17), 6597-6603.

(39) Yi, P.; Chen, K. L., Influence of Surface Oxidation on the Aggregation and Deposition Kinetics of Multiwalled Carbon Nanotubes in Monovalent and Divalent Electrolytes. *Langmuir* **2011,** *27*, (7), 3588-3599.

(40) Lecoanet, H. F.; Bottero, J. Y.; Wiesner, M. R., Laboratory assessment of the mobility of nanomaterials in porous media. *Environ. Sci. Technol.* **2004,** *38*, (19), 5164-5169.

(41) Lecoanet, H. F.; Wiesner, M. R., Velocity effects on fullerene and oxide nanoparticle deposition in porous media. *Environ. Sci. Technol.* **2004,** *38*, (16), 4377-4382.

(42) Brant, J.; Lecoanet, H.; Wiesner, M. R., Aggregation and deposition characteristics of fullerene nanoparticles in aqueous systems. *J. Nanopart. Res.* **2005,** *7*, (4-5), 545-553.

(43) Espinasse, B.; Hotze, E. M.; Wiesner, M. R., Transport and retention of colloidal aggregates of C-60 in porous media: Effects of organic macromolecules, ionic composition, and preparation method. *Environ. Sci. Technol.* **2007,** *41*, (21), 7396-7402.

(44) Chen, K. L.; Elimelech, M., Interaction of Fullerene (C(60)) Nanoparticles with Humic Acid and Alginate Coated Silica Surfaces: Measurements, Mechanisms, and Environmental Implications. *Environ. Sci. Technol.* **2008,** *42*, (20), 7607-7614.

(45) Li, Y. S.; Wang, Y. G.; Pennell, K. D.; Abriola, L. M., Investigation of the transport and deposition of fullerene (C60) nanoparticles in quartz sands under varying flow conditions. *Environ. Sci. Technol.* **2008,** *42*, (19), 7174-7180.

(46) Wang, Y. G.; Li, Y. S.; Fortner, J. D.; Hughes, J. B.; Abriola, L. M.; Pennell, K. D., Transport and retention of nanoscale C-60 aggregates in water-saturated porous media. *Environ. Sci. Technol.* **2008,** *42*, (10), 3588-3594.

(47) Wang, Y. G.; Li, Y. S.; Pennell, K. D., Influence of electrolyte species and concentration on the aggregation and transport of fullerene nanoparticles in quartz sands. *Environ. Toxicol. Chem.* **2008,** *27*, (9), 1860-1867.

(48) Jaisi, D. P.; Elimelech, M., Single-Walled Carbon Nanotubes Exhibit Limited Transport in Soil Columns. *Environ. Sci. Technol.* **2009,** *43*, (24), 9161-9166.

(49) Tong, M. P.; Ding, J. L.; Shen, Y.; Zhu, P. T., Influence of biofilm on the transport of fullerene (C(60)) nanoparticles in porous media. *Water Res.* **2010,** *44*, (4), 1094-1103.

(50) Isaacson, C.; Zhang, W.; Powell, T.; Ma, X.; Bouchard, D., Temporal Changes in Aqu/C(60) Physical-Chemical, Deposition, and Transport Characteristics in Aqueous Systems. *Environ. Sci. Technol.* **2011,** *45*, (12), 5170-5177.

(51) Jaisi, D. P.; Saleh, N. B.; Blake, R. E.; Elimelech, M., Transport of Single-Walled Carbon Nanotubes in Porous Media: Filtration Mechanisms and Reversibility. *Environ. Sci. Technol.* **2008,** *42*, (22), 8317-8323.

(52) Bradford, S. A.; Torkzaban, S.; Walker, S. L., Coupling of physical and chemical mechanisms of colloid straining in saturated porous media. *Water Res.* **2007,** *41*, (13), 3012-3024.

(53) Wang, P.; Shi, Q. H.; Liang, H. J.; Steuerman, D. W.; Stucky, G. D.; Keller, A. A., Enhanced Environmental Mobility of Carbon Nanotubes in the Presence of Humic Acid and Their Removal from Aqueous Solution. *Small* **2008,** *4*, (12), 2166-2170.

(54) Liu, X. Y.; O'Carroll, D. M.; Petersen, E. J.; Huang, Q. G.; Anderson, C. L., Mobility of Multiwalled Carbon Nanotubes in Porous Media. *Environ. Sci. Technol.* **2009,** *43*, (21), 8153-8158.

(55) Kang, S.; Mauter, M. S.; Elimelech, M., Physicochemical determinants of multiwalled carbon nanotube bacterial cytotoxicity. *Environ. Sci. Technol.* **2008,** *42*, (19), 7528-7534.

(56) Kang, S.; Mauter, M. S.; Elimelech, M., Microbial Cytotoxicity of Carbon-Based Nanomaterials: Implications for River Water and Wastewater Effluent. *Environ. Sci. Technol.* **2009,** *43*, (7), 2648-2653.

(57) Kang, S.; Pinault, M.; Pfefferle, L. D.; Elimelech, M., Single-walled carbon nanotubes exhibit strong antimicrobial activity. *Langmuir* **2007,** *23*, (17), 8670-8673.

(58) Vecitis, C. D.; Zodrow, K. R.; Kang, S.; Elimelech, M., Electronic-Structure-Dependent Bacterial Cytotoxicity of Single-Walled Carbon Nanotubes. *ACS Nano* **2010,** *4*, (9), 5471-5479.

(59) Arias, L. R.; Yang, L. J., Inactivation of Bacterial Pathogens by Carbon Nanotubes in Suspensions. *Langmuir* **2009,** *25*, (5), 3003-3012.

(60) Rodrigues, D. F.; Elimelech, M., Toxic Effects of Single-Walled Carbon Nanotubes in the Development of E. coli Biofilm. *Environ. Sci. Technol.* **2010,** *44*, (12), 4583-4589.

(61) Yang, C. N.; Mamouni, J.; Tang, Y. A.; Yang, L. J., Antimicrobial Activity of Single-Walled Carbon Nanotubes: Length Effect. *Langmuir* **2010,** *26*, (20), 16013-16019.

(62) Kang, S.; Herzberg, M.; Rodrigues, D. F.; Elimelech, M., Antibacterial effects of carbon nanotubes: Size does matter. *Langmuir* **2008,** *24*, (13), 6409-6413.

(63) Wei, L. P.; Thakkar, M.; Chen, Y. H.; Ntim, S. A.; Mitra, S.; Zhang, X. Y., Cytotoxicity effects of water dispersible oxidized multiwalled carbon nanotubes on marine alga, Dunaliella tertiolecta. *Aquat. Toxicol.* **2010,** *100*, (2), 194-201.

(64) Blaise, C.; Gagne, F.; Ferard, J. F.; Eullaffroy, P., Ecotoxicity of selected nano-materials to aquatic organisms. *Environ. Toxicol.* **2008,** *23*, (5), 591-598.

(65) Velzeboer, I.; Hendriks, A. J.; Ragas, A. M. J.; Van de Meent, D., Aquatic ecotoxicity tests of some nanomaterials. *Environ. Toxicol. Chem.* **2008,** *27*, (9), 1942-1947.

(66) Ghafari, P.; St-Denis, C. H.; Power, M. E.; Jin, X.; Tsou, V.; Mandal, H. S.; Bols, N. C.; Tang, X. W., Impact of carbon nanotubes on the ingestion and digestion of bacteria by ciliated protozoa. *Nat. Nanotechnol.* **2008,** *3*, (6), 347-351.

(67) Zhu, Y.; Zhao, Q. F.; Li, Y. G.; Cai, X. Q.; Li, W., The interaction and toxicity of multi-walled carbon nanotubes with Stylonychia mytilus. *J. Nanosci. Nanotechnol.* **2006,** *6*, (5), 1357-1364.

(68) Gorczyca, A.; Kasprowicz, M. J.; Lemek, T., Physiological effect of multi-walled carbon nanotubes (MWCNTs) on conidia of the entomopathogenic fungus, Paecilomyces fumosoroseus (Deuteromycotina: Hyphomycetes). *J. Environ. Sci. Health Part A-Toxic/Hazard. Subst. Environ. Eng.* **2009,** *44*, (14), 1592-1597.

(69) Zhu, S. Q.; Oberdorster, E.; Haasch, M. L., Toxicity of an engineered nanoparticle (fullerene, C-60) in two aquatic species, Daphnia and fathead minnow. *Mar. Environ. Res.* **2006,** *62*, S5-S9.

(70) Sayes, C. M.; Fortner, J. D.; Guo, W.; Lyon, D.; Boyd, A. M.; Ausman, K. D.; Tao, Y. J.; Sitharaman, B.; Wilson, L. J.; Hughes, J. B.; West, J. L.; Colvin, V. L., The differential cytotoxicity of water-soluble fullerenes. *Nano Lett.* **2004,** *4*, (10), 1881-1887.

(71) Andrievsky, G.; Klochkov, V.; Derevyanchenko, L., Is the C60 fullerene molecule toxic?! *Fullerenes, Nanotubes, and Carbon Nanostructures* **2005,** *13*, (4), 363-376.

(72) Henry, T. B.; Menn, F. M.; Fleming, J. T.; Wilgus, J.; Compton, R. N.; Sayler, G. S., Attributing effects of aqueous C-60 nano-aggregates to tetrahydrofuran decomposition products in larval zebrafish by assessment of gene expression. *Environ. Health Perspect.* **2007,** *115*, (7), 1059-1065.

(73) Zhang, B.; Cho, M.; Fortner, J. D.; Lee, J.; Huang, C. H.; Hughes, J. B.; Kim, J. H., Delineating Oxidative Processes of Aqueous C(60) Preparations: Role of THF Peroxide. *Environ. Sci. Technol.* **2009,** *43*, (1), 108-113.

(74) Markovic, Z.; Todorovic-Markovic, B.; Kleut, D.; Nikolic, N.; Vranjes-Djuric, S.; Misirkic, M.; Vucicevic, L.; Janjetovic, K.; Isakovic, A.; Harhaji, L.; Babic-Stojic, B.;

Dramicanin, M.; Trajkovic, V., The mechanism of cell-damaging reactive oxygen generation by colloidal fullerenes. *Biomaterials* **2007,** *28*, (36), 5437-5448.

(75) Sayes, C. M.; Gobin, A. M.; Ausman, K. D.; Mendez, J.; West, J. L.; Colvin, V. L., Nano-C-60 cytotoxicity is due to lipid peroxidation. *Biomaterials* **2005,** *26*, (36), 7587-7595.

(76) Lee, J.; Yamakoshi, Y.; Hughes, J. B.; Kim, J. H., Mechanism of C-60 photoreactivity in water: Fate of triplet state and radical anion and production of reactive oxygen species. *Environ. Sci. Technol.* **2008,** *42*, (9), 3459-3464.

(77) Lee, J.; Fortner, J. D.; Hughes, J. B.; Kim, J. H., Photochemical production of reactive oxygen species by C-60 in the aqueous phase during UV irradiation. *Environ. Sci. Technol.* **2007,** *41*, (7), 2529-2535.

(78) Lyon, D. Y.; Brunet, L.; Hinkal, G. W.; Wiesner, M. R.; Alvarez, P. J. J., Antibacterial activity of fullerene water suspensions (nC(60)) is not due to ROS-mediated damage. *Nano Lett.* **2008,** *8*, (5), 1539-1543.

(79) Lyon, D. Y.; Alvarez, P. J. J., Fullerene Water Suspension (nC(60)) Exerts Antibacterial Effects via ROS-Independent Protein Oxidation. *Environ. Sci. Technol.* **2008,** *42*, (21), 8127-8132.

(80) Liu, S. B.; Wei, L.; Hao, L.; Fang, N.; Chang, M. W.; Xu, R.; Yang, Y. H.; Chen, Y., Sharper and Faster "Nano Darts" Kill More Bacteria: A Study of Antibacterial Activity of Individually Dispersed Pristine Single-Walled Carbon Nanotube. *ACS Nano* **2009,** *3*, (12), 3891-3902.

(81) Liu, S. B.; Zeng, T. H.; Hofmann, M.; Burcombe, E.; Wei, J.; Jiang, R. R.; Kong, J.; Chen, Y., Antibacterial Activity of Graphite, Graphite Oxide, Graphene Oxide, and Reduced Graphene Oxide: Membrane and Oxidative Stress. *ACS Nano* **2011,** *5*, (9), 6971-6980.

Chapter 3: Photochemical Transformation of Carboxylated Multi-walled Carbon Nanotubes in Sunlight

3.1 Introduction

The remarkable electronic, mechanical and optical properties of CNTs enabled a wide range of promising applications. The production of CNTs in the United States was already estimated to be 55 ~ 1,101 tons per year as of 2011 [1]. The fast growing production and potential widespread use in consumer products (e.g., electronics and sport equipments) raise concerns regarding their potential risk to human health and ecosystems. As a result, the fate, transport and toxicity of CNTs need to be carefully studied in order to assist risk assessment as well as mitigate potential hazards.

Transformation of CNTs leads to changes of physicochemical properties which govern the environmental mobility and toxicity. Several studies have investigated the potential routes of CNT transformation or degradation under natural conditions, most of which focus on enzyme-catalyzed degradation processes [2-4]. Peroxidase enzymes, mainly horseradish peroxidase and myeloperoxidase, were reported to degrade both SWCNTs and MWCNTs in the presence of trace amount of H_2O_2 [3, 4]. The degradation was attributed to the high oxidative potential of peroxidases and their byproducts such as hypochlorite [2]. However little is known about the abiotic transformation of CNTs in the environment. Our recent study reported that COOH-MWCNTs lost surface oxygen-containing functional groups under UVA irradiation in aqueous solutions [5]. Certain CNTs (e.g., carboxylated SWCNT and MWCNT) was found to produce ROS when exposed to UVA light [5, 6]. These ROS have similar or higher oxidative potential than those oxidants

involved in the enzyme-catalyzed degradation processes and are produced on the sidewall. Moreover, photogenerated $^1O_2$ was reported to oxidize fullerene nanoparticles, which share similar carbon structures as CNTs, facilitating their transport in the environment [7-9]. Thus we hypothesize that COOH-MWCNTs will react with self-generated ROS and undergo photochemical transformation under solar irradiation, leading to changes of the structure and consequently their fate and transport in the environment.

In this study, we examined our hypothesis and investigated mechanisms of the photochemical transformation of COOH-MWCNTs under UVA light which is the major UV component in sunlight. The production of $^1O_2$ and ·OH by COOH-MWCNTs under UVA light was quantified using probe molecules. COOH-MWCNTs were reacted with externally generated $^1O_2$ and ·OH respectively to examine their impacts on nanotube surface chemistry. The changes of oxygen-containing functional group distribution and the surface defects of COOH-MWCNTs were characterized by Raman spectroscopy and chemical derivatization in conjunction with XPS. They were later compared with the corresponding changes in photochemical transformation of COOH-MWCNTs to illustrate the differential roles of self-generated ROS in phototransformation process. Inhibition experiments in low-oxygen conditions and in the presence of hole scavengers were performed to further reveal the reaction mechanisms and the generation route of ·OH. Impacts of ·OH on the stability of COOH-MWCNTs was examined using sedimentation experiments to elucidate the potential implications of phototransformation on their transport in aquatic systems. Based on these evidence, we propose the photochemical transformation of COOH-MWCNTs in sunlight is mediated by self-generated ROS, mainly ·OH, leading to reduction of surface oxygen concentration, mainly through

removal of carboxyl groups. The phototransformation process reduced the surface potential and stability of COOH-MWCNTs and consequently their mobility in the aquatic environment.

3.2 Materials and Methods

3.2.1 Materials

COOH-MWCNTs (>95%, PD15L1-5-COOH) were purchased from NanoLab, Inc. (Newton, MA) with reported diameter and length to be 15 ± 5 nm and 1 ~ 5 μm, respectively. They were produced by refluxing pristine MWCNTs synthesized by a chemical vapor deposition method in a concentrated HNO_3/H_2SO_4 mixture. Terephthalic acid (TPA, >99%) was purchased from Acros organics (New Jersey, USA). Furfuryl alcohol (FFA, 98%), 2-hydroxyterephthalic acid (HTPA, 97%), Rose Bengal (95%), 2,2,2-trifluoroacetic anhydride (TFAA, >99%), 2,2,2-trifluoroethanol (TFE, >99%), N,N'-di-tert-butyl-carbodiimide (DTBC, >99%), and 2,2,2-trifluoroethylhydrazine (TFH, 70 wt.% solution in water) were purchased from Aldrich Chemicals (Milwaukee, Wisconsin). All other chemicals were reagent grade. The deionized water (18.2 MΩ•cm resistivity at 25 °C) was produced by a Barnstead Epure water purification system (Dubuque, IA).

3.2.2 Preparation of COOH-MWCNT Stock Suspension

The COOH-MWCNT stock suspension was prepared by direct sonication. 40 mg COOH-MWCNT was added to 400 mL deionized water in a 500-mL glass beaker. The mixture was placed in an ice bath and sonicated with a sonicating probe (Vibra-Cell VCX

500, Sonics & Material, Newtown, CT) at 100 W for 30 min. The COOH-MWCNTs used in the aggregation and deposition experiments in Section 3.4.6 were prepared differently. An aliquot of 5 mg COOH-MWCNT was added to 100 mL deionized water in a 200 mL glass beaker. The mixture was put in an ice bath and sonicated with the same sonicating probe for 30 min (power output of 50 W for 10 min, 75 W for 10 min, and 100 W for 10 min). A stable dispersion was obtained after sonication and was stored in dark at room temperature until use.

3.2.3 Photochemcial Transformation Experiments

The photochemical transformation experiments were carried out in a Luzchem LZC-4V Photoreactor (Luzchem, Ottawa, Ontario, Canada). Eight 8W black-light lamps (EIKO F8T5/BL, 4 on each side) with an emitting spectrum in the UVA range (350±50 nm) were employed to mimic the UVA fraction of the solar spectrum. The total light intensity at the center of the reactor where the sample suspension was located was measured at 2.4 mW/cm^2 using a Radiometer (Control Company, Friendswood, TX), which is comparable to the UVA intensity of sunlight measured on a sunny day in Houston, Texas. In each experiment, a 500-mL glass beaker containing 400 mL of suspension was placed at the center of the photoreactor. All suspensions contained 10 mg/L COOH-MWCNTs with unadjusted pH at 5.7 ± 0.3. In low-oxygen inhibition experiment, 100 mL 10 mg/L COOH-MWCNTs in a 150-mL glass bottle was purged with N_2 for 1 h and sealed during irradiation. A parallel sample without N_2 purge was irradiated in a 150-mL glass bottle with the cap open. The dissolved oxygen concentration in the suspension was measured by a dissolved oxygen meter (YSI 550A, YSI Incorporated). Samples used in the aggregation and deposition experiments in

Section 3.4.6 were prepared differently. Four 8W black lamps were employed in irradiation experiments, providing a light intensity of approximately 2 mW/cm^2 at the center of the reactor. In each experiment, two Erlenmeyer flasks each containing 50 mL of sample were placed on the merry-go-round at the center of the photoreactor and rotated to ensure uniform exposure. All suspensions contained 4 mg/L COOH-MWCNT with unadjusted pH at 6.0 ± 0.2. As the photochemical reaction proceeded, samples were withdrawn at predetermined times and stored in dark for further analyses and aggregation and deposition kinetic experiments.

3.2.4 ROS Measurements

The $^1O_2$ generation was quantified by the loss of a scavenger, FFA [10]. 100 mL suspension containing 0.2 mM FFA and 10 mg/L COOH-MWCNTs was sealed with vented labfilm, and stirred and irradiated at a intensity of 2.4 mW/cm^2 provided by six 4W black-light lamps (EIKO F4T5/BL, 3 on each side, 350±50 nm) in a custom made photoreactor. The FFA at this concentration is suggested to be specific to $^1O_2$ [11, 12]. Before taking the sample, deionized water was added into the suspension to compensate the evaporation during irradiation. Sample aliquots of 5 mL were withdrawn at predetermined times using a syringe and filtered through 0.22-μm pore size PTFE filters (Millipore, Billerica, MA). The remaining FFA in the filtrate was analyzed by 218 nm UV-absorbance using a high-performance liquid chromatography (SHIMADZU, Japan) with a C18 column (Ecilipse XD8, Agilent) and a mobile phase comprising 30% acetonitrile and 70% 0.1 wt% phosphoric acid at a flow rate of 0.5 mL/min.

The production of ·OH was measured by a fluorescence probe, TPA [13, 14]. TPA was dissolved in 0.5 mM NaOH solution, stirred for 24 h, and filtered through a 0.45-μm membrane. 100 mL suspension of 72 μM TPA and 10 mg/L COOH-MWCNT was irradiated under the same condition as $^1O_2$ measurements. Deionized water was added into the suspension before withdrawing samples to compensate the evaporation during irradiation. Samples were filtered through 30K MWCO centrifugal filters (Amicon Ultra, Millipore, Ireland) to remove CNTs. The reaction between ·OH and TPA yielded HTPA, which was later analyzed by a fluorescence spectroscopy ($\lambda_{excitation}$=315nm, $\lambda_{emission}$=425 nm, HITACHI F-2500).

In control experiments, solutions containing only the scavengers were irradiated under the same condition to determine the loss of FFA and the generation of HTPA without the presence of CNTs. All the ROS measurements were also repeated in dark condition.

3.2.5 Reactions between COOH-MWCNTs and External ROS

In order to isolate effects of $^1O_2$ and ·OH on COOH-MWCNT surface chemistry, external ROS sources were introduced. ·OH was generated by UV photolysis of H_2O_2. 50 mg/L COOH-MWCNTs were mixed with 15% H_2O_2 and exposed to 2.0 mW/cm^2 UVA irradiation in the Luzchem LZC-4V Photoreactor using six 8W black-light lamps. After reacting for a predetermined period of time, the resulting COOH-MWCNT suspension was filtered through 0.1-μm membrane. The CNTs retained on the membrane was thoroughly washed with deionized water and dried in vacuum at 80 ℃ for 24 h for further analysis.

$^1O_2$ was produced by sensitizing Rose Bengal under visible light provided by 8 fluorescence lamps (SYLVANIA F8T5/CW) in the Luzchem LZC-4V Photoreactor. Oxygen gas was continuously purged into the solution containing 50 mg/L COOH-MWCNTs and 12.5 μM Rose Bengal. Upon finishing the reaction, CNT suspension was filtered through 0.1-μm membrane. The Rose Bengal adsorbed on COOH-MWCNTs was removed by consecutively washing with 100 mL methanol for at least 6 times. Then the CNT samples were washed with deionized water and dried in vacuum at 80 ℃ for 24 h.

3.2.6 Sedimentation Experiments

Immediately before sedimentation experiments, COOH-MWCNT samples were re-suspended in deionized water using cup sonication at 100 W for 5 min. 1 mL 40 mM NaCl solution was mixed with 3 mL COOH-MWCNT suspension (A_{350} = 0.7) to induce aggregation and sedimentation. The sedimentation curves were recorded using a SHIMADZU UV-vis spectrometer at a wavelength of 350 nm.

3.2.7 Characterization of COOH-MWCNTs

The surface chemical composition of the CNTs was characterized using XPS. The XPS analysis was carried out using a PHI Quanteria SXM scanning X-ray microprobe ULVAC-PHI with an 24.8 W X-ray source and a 200.0 μm X-ray spot size at 45.0° (26.00 eV). The atomic concentrations of different elements were quantified by the areas of corresponding photoelectron peaks. The concentration of three major oxygen-containing functional groups including carboxyl, hydroxyl and carbonyl (atomic oxygen concentrations in the functional groups) were quantified using chemical derivatization in conjunction with XPS technique which has been described in previous papers [15, 16].

Functional groups were quantified one at a time. The recipes of derivation reagents are as follow: 1.0 mL TFE, 0.4 mL pyridine and 0.2 mL DTBC for carboxyl groups; 1.0 mL TFAA for hydroxyl groups; and 0.4 mL TFH for carbonyl groups. Briefly, a piece of CNT cake layer on filtration membrane was placed in a 1.5 mL microtube with cap removed. The derivation reagents for a specific functional group were added into the glass reaction vessel and frozen by dipping the reaction vessel into a liquid nitrogen container. The microtube containing CNT sample was immediately put into the reaction vessel which was then evacuated and sealed. The derivatization was allowed to proceed for 24 h at room temperature. The resulting CNT samples were analyzed using XPS right after being taken out of the reaction vessel. The oxygen concentrations in major oxygen-containing functional groups can be calculated based on the measured C(1s), F(1s), and N(1s) peaks from the XPS spectra of CNTs after derivatization and the surface carbon concentration of CNTs prior to derivatization. The residue oxygen concentration was calculated by subtracting oxygen concentration in measured three oxygen-containing functional groups measured from the total surface oxygen concentration. More details regarding quantifying oxygen-containing functional groups on CNT surface can be found in Reference [15].

The Raman spectra of CNTs were acquired using a RENISHAW in Via Raman microscope (RENISHAW, Hoffman Estates, IL) with a 514 nm laser focused through a ×50 objective lens. Each sample was scanned 10 times. The ζ potential of CNTs was measured in folded capillary cells (Malvern, Worcestershire, UK) by phase analysis light scattering (PALS) at 23 °C. Ten measurements were carried out for each sample.

3.2.8 Aggregation Kinetics of COOH-MWCNTs

Aggregation kinetics of the initial and irradiated COOH-MWCNT suspensions in various solution conditions were characterized by monitoring the intensity-weighted average particle hydrodynamic diameter (D_h) as a function of time via time-resolved DLS measurement. For all experiments, 0.25 mL of the COOH-MWCNT suspension was transferred to a disposable polystyrene cuvette (Sarstedt, Germany) and the appropriate amount of stock NaCl or $CaCl_2$ solution and DI water were added to achieve the desired electrolyte concentration. The addition of NaCl and $CaCl_2$ has negligible impact on the pH of the suspensions. The total volume of the final suspension was 1 mL and the concentration of COOH-MWCNT suspensions was 1.0 mg/L. The solution was briefly shaken and quickly inserted into the vat of the light scattering unit. The DLS measurement was initiated immediately. Auto-correlation function was accumulated for every 15 s.

The initial aggregation rate constant (k) of the COOH-MWCNT suspensions was obtained by fitting the initial linear increase in D_h [17, 18] using eq 3-1:

$$\left(\frac{dD_h(t)}{dt}\right)_{t\to 0} \propto kN_0 \tag{3-1}$$

where which N_0 is the initial number concentration. In our experiments, all samples have the same particle concentration. For most cases, linear least square regression was applied to the $D_h(t)$ data between the initial value $D_h(0)$ to approximately 1.5 $D_h(0)$. However, at low electrolyte concentrations, the aggregation happened very slowly; the regression analysis was conducted to less than 1.5 $D_h(0)$ but over more than 20 min. To

quantify the aggregation kinetics, the attachment efficiency (α, the inverse of the stability ratio W) was calculated by normalizing the initial aggregation rate in D_h at the electrolyte concentration of interest by the initial rate of increase in D_h under diffusion-limited conditions, where the rate is independent of electrolyte concentration [19]:

$$\alpha = \frac{1}{W} = \frac{k}{k_{fast}} = \frac{\left(\frac{dD_h(t)}{dt}\right)_{t\to 0}}{\left(\frac{dD_h(t)}{dt}\right)_{t\to 0:\,fast}} \qquad (3\text{-}2)$$

Although the DLS size measurement and the above equations assume spherical particles, the results should be valid for comparative studies of the same type of particles. Several studies have shown that this approach could be applied to characterize aggregation behavior of CNTs [20-24].

3.2.9 Deposition Kinetics of COOH-MWCNTs

Deposition kinetics of the COOH-MWCNTs onto silica surface was studied using QCM-D (Q-Sense E4, Västra Frölunda, Sweden). The QCM-D unit is equipped with four measurement chambers, each holds a 5 MHz AT-cut silica coated quartz crystal sensor. Before use, the silica crystals were soaked in 2% SDS cleaning solution for 12 hr and sonicated in a sonication bath for 15 min. They were then rinsed with deionized water, dried with ultra high-purity N_2 and cleaned in an ozone/UV chamber (Bioforce Nanoscience, Inc., Ames, IA) for 30 min. Clean crystals were mounted in the measurement chambers with a constant temperature of 20 ^{o}C. The flow rate was set at 0.1 mL/min which results in a laminar flow in the measurement chambers. Before each

measurement, the background solution was flowed across the crystal surface until the frequency signal drifts less than 1.8 Hz/h. After a stable baseline was achieved, predetermined amount of electrolyte solution and COOH-MWCNTs suspension were mixed to form samples with 2 mg/L COOH-MWCNT in the electrolyte solution of interest. The resulting suspension was immediately pumped through the measurement chambers, allowing COOH-MWCNT deposition onto the silica crystal surface to be monitored. As the deposition took place, the increasing mass of COOH-MWCNTs on the silica crystal surface hindered the vibration of the crystal and subsequently reduced its frequency. The mass of a thin and rigid deposited layer on the silica crystal surface can be related to the frequency shift as described by the Sauerbrey equation [25]:

$$\Delta m = -\frac{C\Delta f_n}{n} \tag{3-3}$$

where Δm is the deposited mass, Δf_n is the frequency shift at overtone n, and C is the crystal constant (17.7 ng/(Hz cm^2)). Although the Squerbrey equation doesn't strictly apply for MWCNT deposition, the frequency shift was found to be proportional to the mass of MWCNTs deposited on the crystal [24]. Thus the deposition rate was quantified using the initial slope (200 s) of the frequency shift at the third overtone, which is the most stable. All deposition experiments were performed in duplicate.

3.3 Results and Discussion

3.3.1 Photochemical Transformation of COOH-MWCNTs

COOH-MWCNT suspensions were exposed to UVA light for 7 days and the change of surface chemistry upon UVA irradiation was examined by XPS. UVA irradiation reduced the surface oxygen concentration of COOH-MWCNTs as shown in Figure 3.1. Similar result also has been reported for graphene oxide upon UV irradiation [26]. To further understand the change of surface chemistry, we examined the changes of major oxygen-containing surface functional groups. The concentrations of three major oxygen-containing functional groups: carboxyl, hydroxyl, and carbonyl, were differentiated from the total oxygen concentration. Figure 1 clearly shows that the reduction of total surface oxygen is attributed to the removal of carboxyl groups. On the other hand, the residue oxygen concentration increased, while O[OH] and O[CO] remained fairly constant during the irradiation. This finding supported our speculation in an earlier study that COOH-MWCNTs underwent surface decarboxylation in sunlight [5]. Nevertheless, the mechanism of CNT photochemical transformation is still unknown. It has been reported that the certain SWCNTs were able to produce ROS in UVA or near-infrared light [6, 27]. ROS are highly reactive and responsible for oxidative transformation of a wide range of organic compounds in natural systems. We hypothesize that self-generated ROS can react with the sidewall, leading to ROS-mediated oxidation of CNTs.

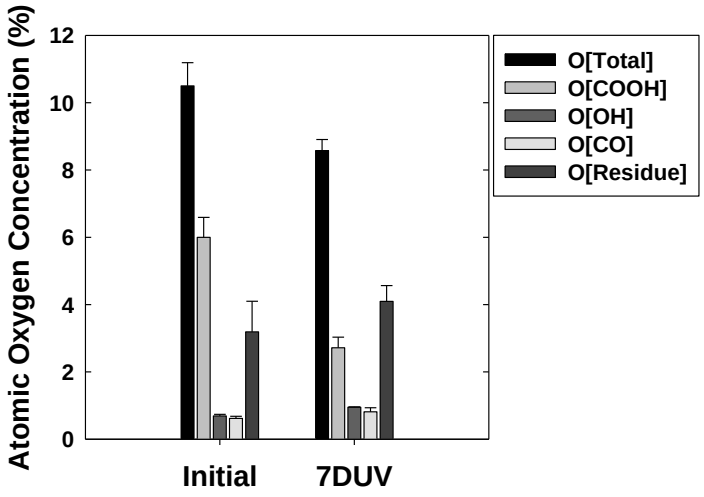

Figure 3.1. Atomic surface oxygen concentration and the distribution of oxygen-containing functional groups on initial and 7-day UVA-irradiated (7DUV) COOH-MWCNTs surfaces. Error bars represent standard deviation.

3.3.2 Production of ROS by COOH-MWCNTs

To test our hypothesis, the production of two major ROS, $^1O_2$ and ·OH, by COOH-MWCNTs was quantified using probe molecules. COOH-MWCNTs were able to generate both $^1O_2$ and ·OH in UVA light as shown in Figure 3.2. In dark condition, FFA, the $^1O_2$ scavenger, was stable both with and without the presence of COOH-MWCNTs (Figure 3.2a). After 67 h irradiation, 17.4 % of the initial FFA was degraded, presumably due to direct photolysis or evaporation. However, the degradation of FFA was much faster in the presence of 10 mg/L COOH-MWCNTs, with a 37.7 % loss in the same period of time, suggesting the production of $^1O_2$. The pseudo-steady-state concentration of $^1O_2$, $[^1O_2]_{ss}$, was calculated to be 6.48×10^{-15} M. This value is comparable to the $[^1O_2]_{ss}$

generated by carboxylated and polyethylene glycol functionalized SWCNTs (3.3×10^{-14} and 1.46×10^{-14} M, respectively) exposed to a UVA light source with different intensity [6].

Under the same set of irradiation conditions, TPA was employed to trap the ·OH. The resulting product, HTPA, was used to quantify the production of ·OH (Figure 3.2b). In dark condition, small amount of HTPA was formed, indicating that COOH-MWCNTs might be able to oxidize TPA without photoexcitation. In the presence of UVA light, the HTPA concentration increased with increasing irradiation time in the presence of COOH-MWCNTs, while little HTPA was formed in the absence, indicating ·OH generation by COOH-MWCNTs. These results show that COOH-MWCNTs are able to produce ·OH in the solar spectrum. The pseudo-steady-state concentration of ·OH, $[\cdot OH]_{ss}$, was 1.48×10^{-18} M under UVA irradiation, much lower than previous reported $[\cdot OH]_{ss}$ generated by carboxylated SWCNTs (1.58×10^{-15} M) [6]. It's worth noting that the actual ROS production by COOH-MWCNTs is difficult to quantify due to the microheterogeneous distribution of ROS in solutions [28, 29]. The short lifetime of $^1O_2$ and ·OH (~ 4 μs and ~ ns in water, respectively [30]) leads to very limited diffusion length. Thus a steep ROS concentration gradient was expected from the CNT surface to the bulk solution. This is especially the case for ·OH since it often presents as surface bounded/adsorbed ·OH rather than free radical diffusing into the bulk solution [31]. Thus it's difficult for scavenger molecules to penetrate into the ROS diffusion zone which locates at the vicinity of the nanotube surface. For instance, earlier study has reported the $^1O_2$ concentration inside and near the irradiated humic acid macromolecules was 2~3 orders of magnitude higher than the measured value in bulk aqueous phase using FFA as a probe [28, 32]. As a result, the ROS could have much larger impact on the CNT structure than expected based on the

measured concentrations in bulk solutions as they were generated and consumed right on the CNT surface.

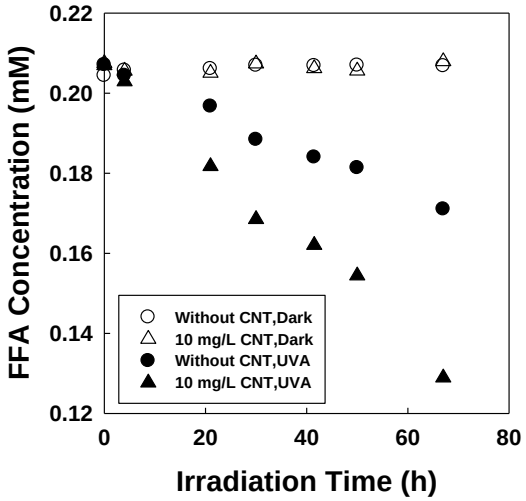

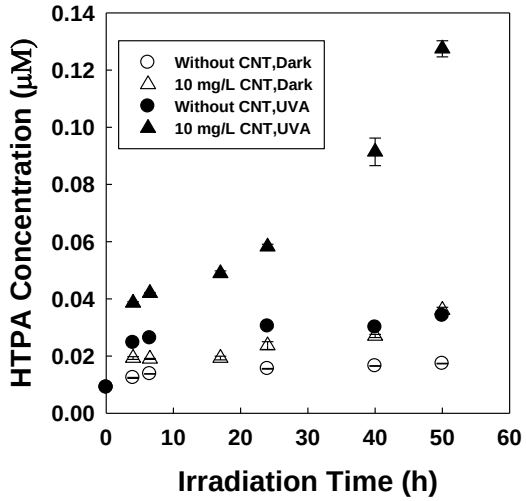

Figure 3.2. FFA loss, representing $^1O_2$ generation (a) and HTPA generation, representing ·OH generation (b) as a function of irradiation time with and without the presence of 10 mg/L COOH-MWCNTs and UVA light. Error bars represent standard deviation.

3.3.3 Effects of $^1O_2$ and ·OH on COOH-MWCNT Surface Chemistry

To isolate effects of $^1O_2$ and ·OH on COOH-MWCNT surface chemistry, COOH-MWCNT was reacted with externally generated $^1O_2$ and ·OH respectively. Rose Bengal was excited by visible light to produce $^1O_2$ which subsequently reacted with carbon nanotubes. After 3 days reaction, however, the surface oxygen of COOH-MWCNTs slightly increased from 10.5 ± 0.69% to 11.26 ± 0.18%; contradict to the observed decreased surface oxygen in the photochemical transformation experiments. Thus $^1O_2$ was not the major mechanism for the photochemical transformation of COOH-MWCNT. Previous experimental and density functional theory calculation studies reported that $^1O_2$ can interact with pristine CNT sidewall, yielding surface oxides [33-35], which agrees with the observed surface oxygen concentration increase. As shown in Figure 3.3, unlike other oxygen-containing functional groups, the carboxyl group concentration decreased after reaction, suggesting that $^1O_2$ also reacts with carboxyl groups, which contributes to the photochemical transformation of COOH-MWCNTs.

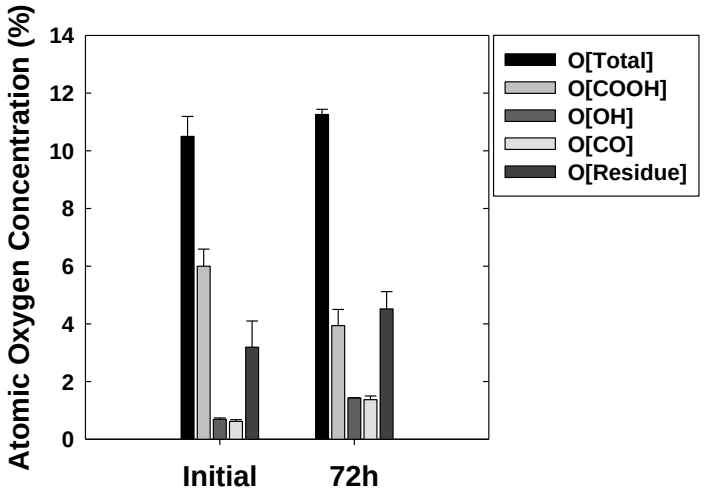

Figure 3.3. Atomic surface oxygen concentration and the distribution of oxygen-containing functional groups on initial and 72h $^1O_2$-treated COOH-MWCNTs surfaces. Error bars represent standard deviation.

·OH was generated by direct photolysis of H_2O_2 with a UVA source. As mentioned in the previous section, COOH-MWCNTs could generate ROS by itself in UVA light. However, the impact of self-generated ROS was expected to be negligible as compared to the external ·OH due to the elevated H_2O_2 concentration used. The surface oxygen concentration along with the distribution of major oxygen-containing functional groups after reacting with ·OH was presented in Figure 3.4. The surface oxygen concentration of COOH-MWCNT gradually decreased as the reaction preceded and reached a plateau at around 5% O after 11 h reaction. The plateau could be caused by the depletion of H_2O_2 after prolonged photolysis. In order to rule out this possibility, H_2O_2 was replenished in another set of experiment denoted as pentagram in Figure 3.4a in which COOH-MWCNTs were harvested after 16.5 h reaction, resuspended in fresh 15% H_2O_2 and reacted for another 7.5 h (i.e., they were reacted with ·OH for 24 h with H_2O_2 replenished

at 16.5 h). The surface oxygen concentration of the resulting COOH-MWCNTs was 4.90 ± 0.14%, similar to that without H_2O_2 replenishment, suggesting the plateau was not caused by H_2O_2 depletion. The oxygen-containing functional groups have different reactivity toward ·OH depending on their nature and location. However, given the high oxidative potential of ·OH (E_0 = 2.3 V, pH 7.0 [36]), it is unlikely that these oxygen-containing groups (~5% O) are inert to ·OH. We speculate reactions with ·OH are unspecific. They both generate and remove oxygen-containing functional groups, leaving holes on the sidewall. This dynamic process reached balance after 11 h at around 5 % O. Our hypothesis is supported by earlier studies in the literature. It has been reported that ·OH attacked defect sites as well as carbon double bonds on pristine MWCNT sidewalls, forming oxygen-containing functional groups including hydroxyl, carbonyl and carboxyl groups [37, 38]. ·OH can further react with hydroxyl and carbonyl groups and oxidize them to carboxyl groups, which can be removed from the CNTs by ·OH. The concentration of hydroxyl groups was found to increase at the beginning and then decrease, indicating they can be further oxidized to form carbonyl and carboxyl groups. The concentration of carboxyl groups also underwent similar trend as they were removed by ·OH at the late stage of the reaction [38]. Figure 3.4b clearly shows that COOH-MWCNTs continuously loss carboxyl groups upon reaction with ·OH, while concentrations of other oxygen-containing functional groups remain relatively stable. This observation qualitatively agrees with the evolution of functional groups in the photochemical transformation of COOH-MWCNT.

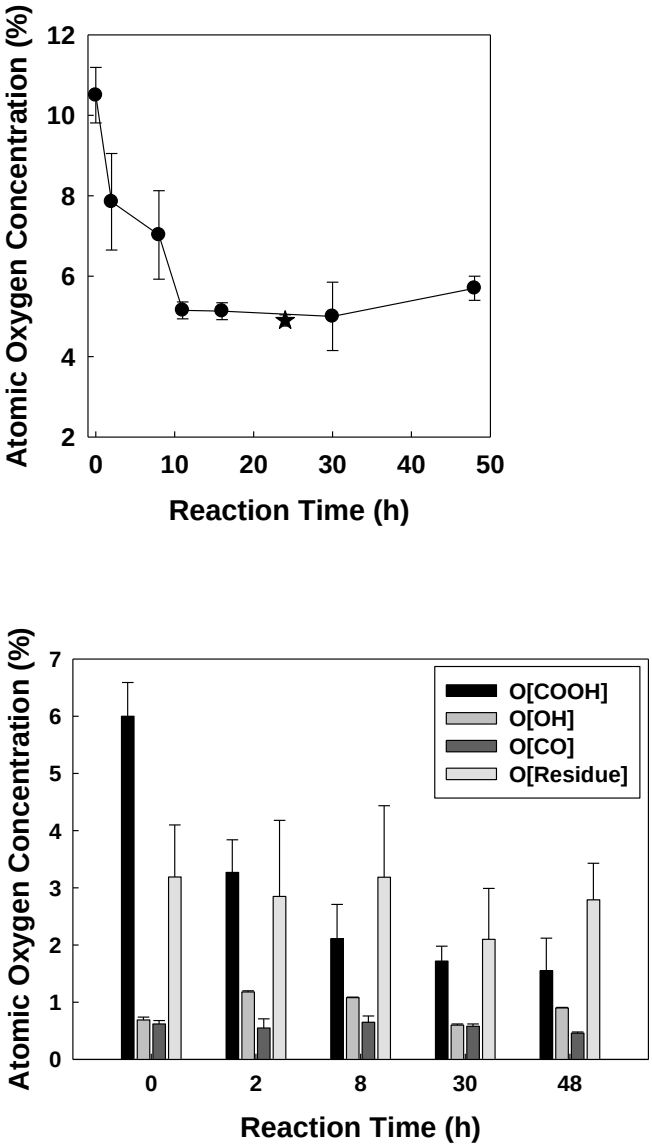

Figure 3.4. Surface atomic oxygen concentration (a) and the distribution of oxygen-containing functional groups (b) on initial and ·OH-treated COOH-MWCNTs surfaces. Error bars represent standard deviation.

The change of surface structure was also studied by Raman spectroscopy. COOH-MWCNTs have three characteristic modes: the radial breathing mode, the tangential mode (G-band (~1585 cm^{-1})) and the D mode (~1353 cm^{-1}). The D mode is the most

studied feature of which the intensity is commonly associated with defect sites or amorphous carbon [39, 40]. The G-band, on the other hand, is typically associated with well ordered sp^2 carbon on the graphitic sidewall. The intensity ratio of these two bands, I_D/I_G, was suggested to be a sensitive indicator for the abundance of the defects [41]. The I_D/I_G value sharply decreased from 0.915 to 0.779 in the first 2 h of reaction with ·OH and increased ever since. The non-monotonic change of I_D/I_G value was also observed in enzyme-catalyzed degradation of oxidized MWCNTs and was attributed to the exfoliation of highly oxidized graphitic lattice from the nanotube surface [4]. The COOH-MWCNTs used in this study is modified from pristine MWCNTs by sulfuric/nitric acids treatment. It has been reported that a large portion of the carboxyl groups created by acid treatment is presented on carboxylated carbonaceous fragments (CCF) on the nanotube surface [40]. We speculate the initial decrease of I_D/I_G along with surface oxygen is caused by removal of carboxyl groups on CCF, leading to their degradation or exfoliation which is known to significant lower the D-band intensity as the inner graphitic sidewall is exposed [40]. The following increase of I_D/I_G can be attributed to the formation of defects (e.g., functional groups and holes) on the graphitic sidewall, which has been observed in many studies when pristine CNTs underwent surface oxidation [37, 38, 42, 43]. The I_D/I_G continues to rise after 11 h reaction, where the surface oxygen concentration remains constant. It can be attributed to the formation of holes during the removal of carboxyl groups. These processes etch the sidewall around functional groups, which potentially leads to the degradation of CNTs. The reduced I_D/I_G of COOH-MWCNTs after UVA irradiation has been previously reported [5], consistent with the initial stage of reaction

with ·OH. The initial reactions between COOH-MWCNTs and the ROS are schematically illustrated in Figure 3.6 based on our findings.

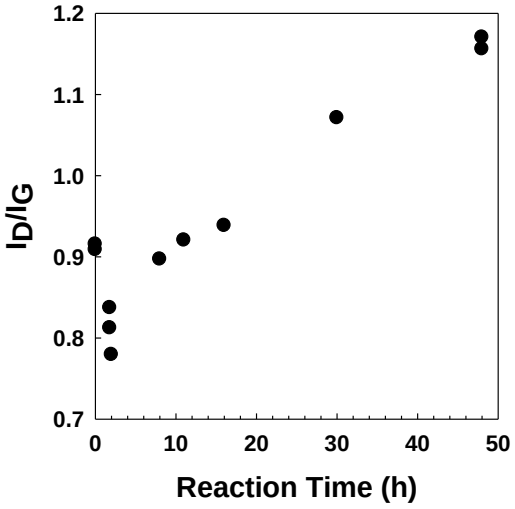

Figure 3.5. The intensity ratio of the D mode and the tangential mode of COOH-MWCNT Raman spectra, I_D/I_G, as a function of the reaction time with ·OH.

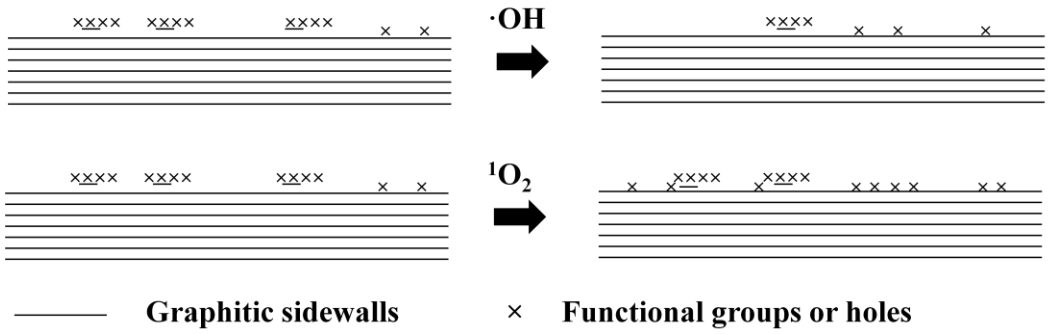

Figure 3.6. Schematic mechanisms for the initial reactions between COOH-MWCNTs and ·OH/$^1O_2$.

3.3.4 Inhibition Experiments

In order to further reveal the reaction mechanisms, two sets of inhibition experiments were conducted. The first set of inhibition experiment was carried out in low-oxygen condition where the suspension was purged with N_2 for 1 h and sealed. After N_2 purge, the dissolved oxygen concentration in the suspension was reduced from 5.33 mg/L to 0.68 mg/L. As the $^1O_2$ was reported to be produced by a type II photosensitization reaction, where the photoexcited CNTs transfer energy to dissolved O_2 [6], its production was expected to be significantly suppressed in low-oxygen condition. However, the surface oxygen concentrations of COOH-MWCNT after 14 days UVA irradiation in both aerobic and low-oxygen conditions were similar (8.37 ± 0.50 % and 8.27 ± 0.15 %, respectively). This finding again indicates $^1O_2$ is not the major player in the photochemical transformation, consistent with our earlier discussion. A recently proposed pathway suggests that ·OH can be generated through electron transfer from excited functionalized SWCNTs to O_2 [6]. Another possible route is reaction between photo-generated electron holes and water molecules, similar to that in TiO_2 photocatalysis. We speculate that ·OH was at least partially formed through the latter mechanism. To test our hypothesis, photochemical transformation experiments were carried out in the presence of electron hole scavengers, Na_2SO_3 [44]. As shown in Figure 3.7, the surface oxygen concentration of COOH-MWCNTs decreased over time in the presence of UVA light as discussed earlier. However, the phototransformation is inhibited in 10 mM Na_2SO_3 after both 3 and 7 days UVA irradiation, suggesting the inhibition of ·OH production. Na_2SO_3 scavenged photo-generated electron holes on COOH-MWCNT surface and consequently suppressed the ·OH production.

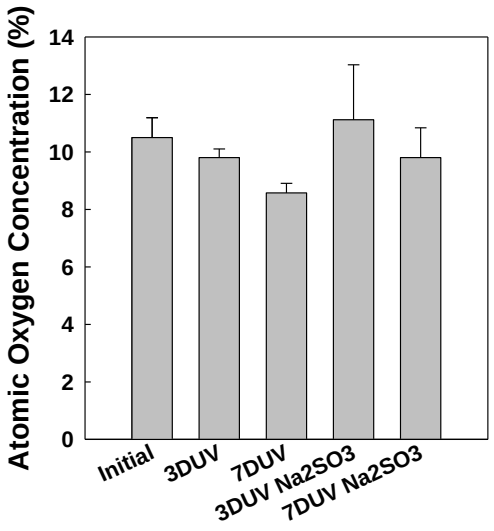

Figure 3.7. Surface atomic oxygen concentration of COOH-MWCNTs before and after UVA irradiation in deionized water or in the presence of 10 mM Na_2SO_3. Error bars represent standard deviation.

3.3.5 Impact of ·OH on the Stability of COOH-MWCNTs

Figure 3.8a presents the sedimentation curves of COOH-MWCNTs reacting with ·OH for various period of time in 10 mM NaCl. The initial COOH-MWCNTs were very stable in 10 mM NaCl due to their highly negatively charged surfaces which electrostatically stabilized the nanotubes. The stability of COOH-MWCNTs gradually decreased with increasing reaction time with ·OH. This change of stability is consistent with the change of surface potential as reflected by ζ potential measurements (Figure 3.8b). Reactions with ·OH reduced the surface potential of COOH-MWCNTs, leading to weaker electrostatic repulsion; hence faster aggregation and sedimentation. To better understand the role of surface functionality in COOH-MWCNT mobility, the relationships between surface oxygen concentration or individual functional group and

the stability were examined. The stability of oxidized MWCNTs was suggested to largely depend on the abundance of surface oxygen-containing functional groups [5, 22, 23]. Nevertheless, the stability of COOH-MWCNTs did not correlate well with the surface oxygen concentration. It continuously decreased after 11 h reaction where the surface oxygen concentration remained stable. On the other hand, a good correlation was found between the carboxyl group concentration and the stability. Considering carboxyl groups are the main oxygen-containing functional groups that dissociate at pH ~ 5.7, they are expected to be the major factor that controls the surface charge and the stability of COOH-MWCNTs. This is consistent with earlier studies examining the influence of surface functionality on the stability of acid modified MWCNTs [22, 23]. These results suggest the key role of ROS-mediated photochemical transformation of COOH-MWCNTs in their environmental transport.

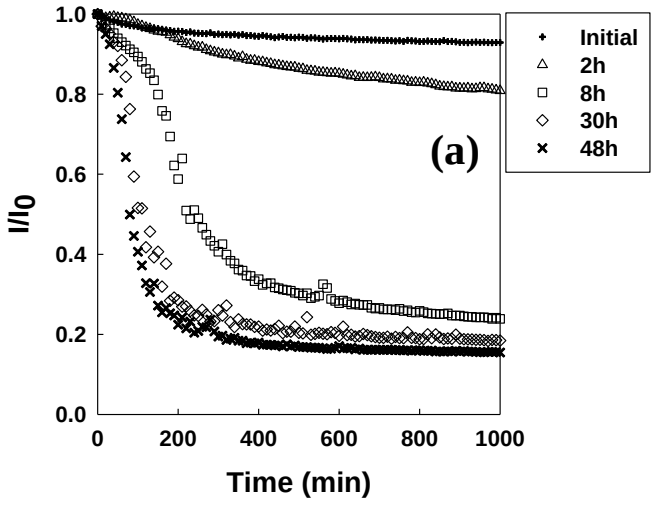

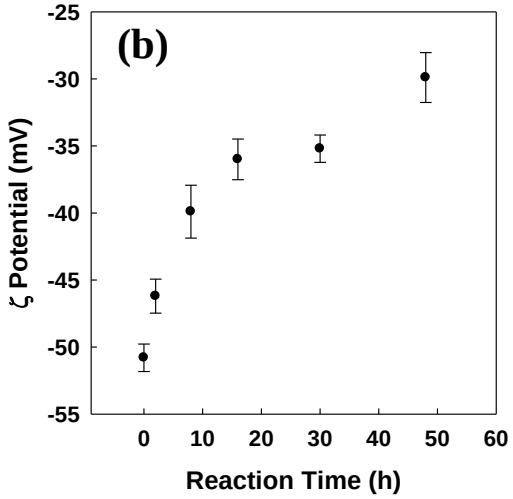

Figure 3.8. Sedimentation curves of COOH-MWCNTs with different reaction time with ·OH in 10 mM NaCl solutions (a) and the ζ potential of COOH-MWCNTs as a function of reaction time with ·OH (b). Error bars represent standard deviation.

3.3.6 Impact of Phototransformation on the Mobility of COOH-MWCNTs

The aggregation and deposition behaviors of initial and UVA-irradiated COOH-MWCNTs were studied to understand the impact of the phototransformation on their environmental transport. Both the initial and 7DUV COOH-MWCNTs showed aggregation behaviors that qualitatively agreed with the DLVO theory, consistent with findings from previous studies [19, 45, 46]. Figures 3.9a and 3.10a present the attachment efficiency (α), i.e., the inverse of the stability ratio, of the initial and 7DUV COOH-MWCNTs in NaCl and $CaCl_2$ solutions, respectively, as a function of the electrolyte concentration. All aggregation profiles are characterized by two distinct aggregation regimes: a reaction-limited aggregation regime ($\alpha<1$) at low electrolyte concentration in which electrostatic repulsion hinders aggregation; and a diffusion-limited aggregation

regime (α= 1) at elevated electrolyte concentrations where the energy barrier from electrostatic repulsion is completely eliminated. This suggested that electrostatic repulsion between COOH-MWCNT particles is the dominant factor controlling particle aggregation. The CCC which represents the electrolyte concentration at the boundary between the two regimes is a useful metric for evaluating colloidal stability. It can be obtained by extrapolating lines through the two regimes, as shown in Figure 3.9a and 3.10a.

The initial COOH-MWCNTs were stable at low NaCl concentrations, with a CCC of 226 mM. The CCC value was comparable to previously reported values for highly oxidized MWCNTs with oxygen contents above 10% [23, 24]. After 7 days of UVA irradiation, however, the stability of the nanoparticles greatly decreased, with a CCC of 52 mM NaCl. The colloidal stability of MWCNTs oxidized by acid wash has been shown to strongly depend on the degree of surface oxidation [22, 23, 47]. Thus the decreased stability observed is attributed to the loss of oxygen-containing functional groups on the surface of the irradiated COOH-MWCNTs, particularly carboxyl functional groups. Oxygen-containing functional groups stabilize MWCNTs through electrostatic repulsions and reduced hydrophobic forces in water [7, 45].

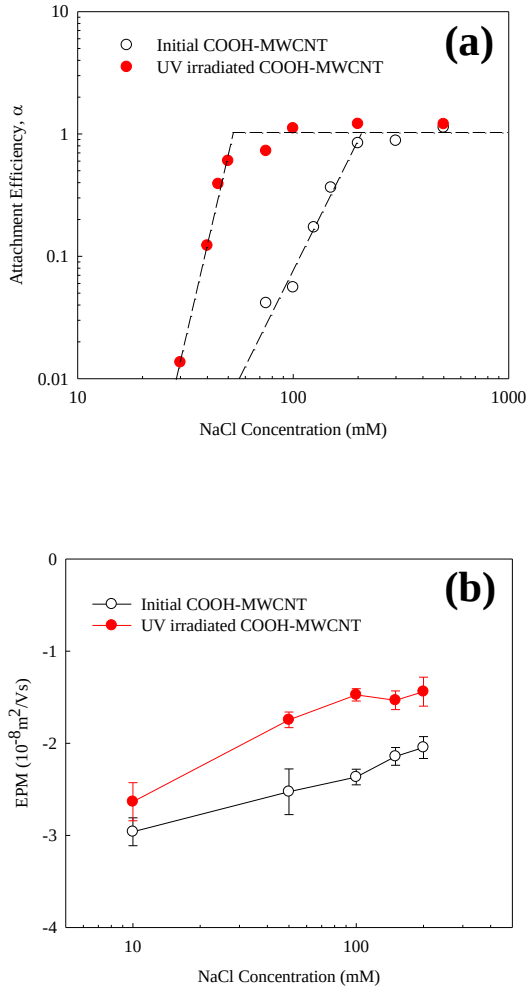

Figure 3.9. Attachment efficiency α (a) and electrophoretic mobility (b) of the initial COOH-MWCNTs and UV irradiated COOH-MWCNTs in NaCl.

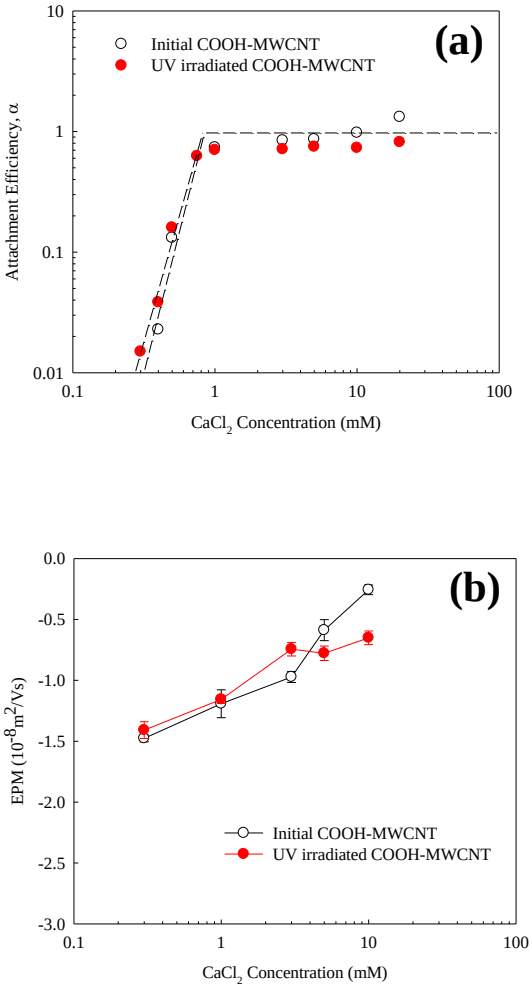

Figure 3.10. Attachment efficiency α (a) and electrophoretic mobility (b) of the initial COOH-MWCNTs and UV irradiated COOH-MWCNTs in $CaCl_2$.

Both the initial and 7DUV COOH-MWCNTs were negatively charged over the range of NaCl concentration studied (10 to 200 mM), and the negative EPM decreased with increasing NaCl concentration due to charge screening as is commonly observed with charged colloidal particles in aqueous solutions (Figure 3.9b). Over the entire range of NaCl, the irradiated COOH-MWCNTs were notably less negatively charged than the initial COOH-MWCNTs, which was consistent with the decreased stability of COOH-

MWCNTs after UVA irradiation. The decrease in negative surface charge was attributed to the loss of carboxyl groups during UVA irradiation as shown in Figure 3.1.

Interestingly, in $CaCl_2$ solutions, the CCC values of $CaCl_2$ for the initial and irradiated COOH-MWCNTs were similar, 0.86 and 0.83 mM respectively (Figure 3.10a). These values were also much smaller than those of NaCl due to charge neutralization by Ca^{2+}. The stability profiles of the COOH-MWCNTs before and after UV irradiation were very similar. The EPM measurement (Figure 3.10b) also revealed that the initial and UV irradiated COOH-MWCNTs had similar negative surface charge over the entire range of $CaCl_2$ concentrations tested (0.3 to 10 mM) despite the difference in surface oxygen content. Because the initial COOH-MWCNTs have more carboxyl groups, these results suggest that Ca^{2+} was more effective in neutralizing negative charges on the initial COOH-MWCNT surface than on the 7DUV COOH-MWCNT. Similar results were reported in the work of Yi and Chen [24] where the aggregation kinetics of two MWCNTs with different degrees of surface oxidation was similar in $CaCl_2$. They suggested that Ca^{2+} has a higher tendency to form complexes with adjacent carboxyl groups on highly oxidized MWCNTs than with isolated carboxyl groups on less oxidized MWCNTs. This offers a plausible explanation to the similar stability of the initial and irradiated COOH-MWCNTs observed in our study. Additional work is necessary to test this hypothesis. Furthermore, the analysis of CCC_{CaCl2}/CCC_{NaCl} ratio suggests that the aggregation of the 7DUV COOH-MWCNTs (CCC_{CaCl2}/CCC_{NaCl} ratio $= 2^{-5.97}$) follow the Schulze-Hardy Rule, which states that the CCC of highly charged particles is proportional to Z^{-6} (Z is the valence of the counter-ion) [45]. In contrast, the behavior of the initial COOH-MWCNTs deviated from the Schulze-Hardy Rule, with a CCC_{CaCl2}/CCC_{NaCl} ratio of $2^{-8.03}$. Because

the Schulze-Hardy Rule is only valid for inert electrolytes, i.e., electrolytes that do not specifically interact with the particle surface, this difference indicates the loss of surface carboxyl groups during UV irradiation that can specifically complex with Ca^{2+}. Similar values of the CCC_{CaCl2}/CCC_{NaCl} ratio were reported by Yi and Chen for surface oxidized MWCNTs: CCC_{CaCl2}/CCC_{NaCl} was $2^{-7.9}$ for highly oxidized MWCNTs and $2^{-5.7}$ for the less oxidized MWCNT [24].

Deposition rates of COOH-MWCNTs depend on both the mass transport of COOH-MWCNTs to the surface and the deposition attachment efficiency (i.e., the probability of a successful attachment resulting from a collision between COOH-MWCNTs and the silica surface). Figure 3.11 shows the deposition rate of the initial and irradiated COOH-MWCNTs as a function of NaCl concentration. Bell shaped relationship was found between the deposition rate and the ionic strength for both COOH-MWCNTs due to the concurrent aggregation at high ionic strength [19, 24]. The mass transfer rate of both COOH-MWCNTs remained constant at low ionic strength (< 20 mM) where the COOH-MWCNT was stable against aggregation as suggested by Figure 3.9a. The increasing ionic strength reduced the energy barrier between COOH-MWCNTs and the silica surface by screening their surface charge, resulting in higher attachment efficiency and consequently higher deposition rates. This is qualitatively consistent with the classic DLVO theory [48, 49]. However, as the ionic strength was further increased, the deposition rate drastically decreased due to the fast concurrent aggregation of COOH-MWCNTs during the deposition process (around 4 min), which resulted in decreased particle diffusivity as described by the Stokes-Einstein equation. The reduced mass transfer

outweighed the enhanced attachment efficiency, leading to a net decrease in deposition rate.

In 5 mM NaCl solution, the deposition rates of both COOH-MWCNTs were under the detection limit of our QCM-D system. While the deposition rate of irradiated COOH-MWCNTs was found to be 3 times higher than initial COOH-MWCNTs in 10 mM NaCl solution. Because the UVA irradiation didn't change the initial particle size of COOH-MWCNTs, the mass transfer rates of initial and irradiated COOH-MWCNTs were considered to be the same at low ionic strength (< 20 mM) where aggregation didn't occur. However, the surface potential of COOH-MWCNTs reduced after irradiation as indicated by their lower electrophoretic mobility (Figure 3.9b), resulting in lower energy barrier. Thus the higher deposition rate of irradiated COOH-MWCNTs at 10 mM NaCl can be attributed to their lower surface potential, which leads to higher attachment efficiency. In 40 mM NaCl solutions, aggregation took place, which greatly hindered the mass transport as discussed earlier. The impact of aggregation on deposition rates of initial and irradiated COOH-MWCNTs was different due to their different aggregation rates at a given ionic strength less than their CCCs. Initial COOH-MWCNTs were much more stable than the UVA irradiated sample as shown in Figure 3.9a. Thus the mass transfer rate of initial COOH-MWCNTs was higher than the irradiated sample at high ionic strength due to their slower aggregation rate and hence higher diffusion coefficient. As a result, the deposition rate of the initial COOH-MWCNTs gradually became higher than irradiated sample as ionic strength increased.

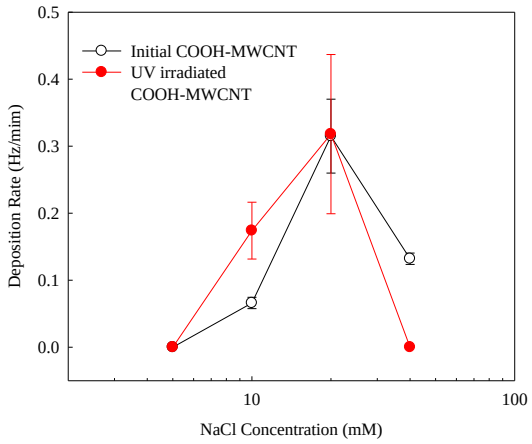

Figure 3.11. Deposition of the initial COOH-MWCNTs and UV irradiated COOH-MWCNTs (7DUV COOH-MWNCTs) in NaCl.

3.4 Conclusion

A mechanistic study of the photochemical transformation of COOH-MWCNTs is presented. UVA irradiation was found to reduce the surface oxygen concentration of COOH-MWCNTs through removal of carboxyl groups. COOH-MWCNTs were able to generate $^1O_2$ and ·OH in UVA light, which had differential effects on their surface structure. Surface oxygen concentration of COOH-MWCNTs decreased upon reaction with ·OH mainly through removal of carboxyl groups, similar to that in the phototransformation. $^1O_2$ also reacted with carboxyl groups, but introduced more oxygen-containing groups, leading to an overall increase in surface oxygen. The Raman spectroscopy and surface functional group distribution data suggested ·OH initially reacted with the carboxylated carbonaceous fragments, resulting in their degradation or exfoliation. Further reaction between ·OH and the graphitic sidewall led to formation of defects including functional groups and holes. The phototransformation process had little

change under low-oxygen condition, suggesting the limited role of $^1O_2$. However, it was suppressed in the presence of Na_2SO_3, an electron hole scavenger, indicating ·OH played a key role in the phototransformation and could be generated by reactions between electron holes and water. Reactions with ·OH reduced the surface potential and stability of COOH-MWCNTs, resulting in lower mobility in aquatic systems. Consistently, changes in surface chemistry induced by UVA irradiation greatly reduced the colloidal stability of COOH-MWCNTs in NaCl solutions. However, the surface potential and stability of COOH-MWCNTs remained constant in $CaCl_2$ solutions after irradiation.

3.5 References

(1) Hendren, C. O. H. C. O.; Mesnard, X.; Droge, J.; Wiesner, M. R., Estimating Production Data for Five Engineered Nanomaterials As a Basis for Exposure Assessment. *Environ. Sci. Technol.* **2011,** *45*, (7), 2562-2569.

(2) Kotchey, G. P.; Hasan, S. A.; Kapralov, A. A.; Ha, S. H.; Kim, K.; Shvedova, A. A.; Kagan, V. E.; Star, A., A Natural Vanishing Act: The Enzyme-Catalyzed Degradation of Carbon Nanomaterials. *Accounts Chem. Res.* **2012**.

(3) Allen, B. L.; Kotchey, G. P.; Chen, Y. N.; Yanamala, N. V. K.; Klein-Seetharaman, J.; Kagan, V. E.; Star, A., Mechanistic Investigations of Horseradish Peroxidase-Catalyzed Degradation of Single-Walled Carbon Nanotubes. *J. Am. Chem. Soc.* **2009,** *131*, (47), 17194-17205.

(4) Zhao, Y.; Allen, B. L.; Star, A., Enzymatic Degradation of Multiwalled Carbon Nanotubes. *J. Phys. Chem. A* **2011,** *115*, (34), 9536-9544.

(5) Hwang, Y. S.; Qu, X.; Li, Q., The Role of Photochemical Transformations in the Aggregation and Deposition of Carboxylated Multiwall Carbon Nanotubes Suspended in Water. *Carbon* **2013**.

(6) Chen, C. Y.; Jafvert, C. T., The role of surface functionalization in the solar light-induced production of reactive oxygen species by single-walled carbon nanotubes in water. *Carbon* **2011,** *49*, (15), 5099-5106.

(7) Qu, X. L.; Hwang, Y. S.; Alvarez, P. J. J.; Bouchard, D.; Li, Q. L., UV Irradiation and Humic Acid Mediate Aggregation of Aqueous Fullerene (nC(60)) Nanoparticles. *Environ. Sci. Technol.* **2010,** *44*, (20), 7821-7826.

(8) Qu, X.; Alvarez, P. J. J.; Li, Q., Impact of Sunlight and Humic Acid on the Deposition Kinetics of Aqueous Fullerene Nanoparticles (nC60). *Environ. Sci. Technol.* **2012,** *46*, (24), 13455-13462.

(9) Hwang, Y. S.; Li, Q. L., Characterizing Photochemical Transformation of Aqueous nC(60) under Environmentally Relevant Conditions. *Environ. Sci. Technol.* **2010,** *44*, (8), 3008-3013.

(10) Haag, W. R.; Hoigne, J.; Gassman, E.; Braun, A. M., SINGLET OXYGEN IN SURFACE WATERS .1. FURFURYL ALCOHOL AS A TRAPPING AGENT. *Chemosphere* **1984,** *13*, (5-6), 631-640.

(11) Maurette, M. T.; Oliveros, E.; Infelta, P. P.; Ramsteiner, K.; Braun, A. M., SINGLET OXYGEN AND SUPEROXIDE - EXPERIMENTAL DIFFERENTIATION AND ANALYSIS. *Helv. Chim. Acta* **1983,** *66*, (2), 722-733.

(12) Chen, C. Y.; Jafvert, C. T., Photoreactivity of Carboxylated Single-Walled Carbon Nanotubes in Sunlight: Reactive Oxygen Species Production in Water. *Environ. Sci. Technol.* **2010,** *44*, (17), 6674-6679.

(13) Ishibashi, K.; Fujishima, A.; Watanabe, T.; Hashimoto, K., Detection of active oxidative species in TiO2 photocatalysis using the fluorescence technique. *Electrochem. Commun.* **2000,** *2*, (3), 207-210.

(14) Ishibashi, K.; Fujishima, A.; Watanabe, T.; Hashimoto, K., Quantum yields of active oxidative species formed on TiO2 photocatalyst. *J. Photochem. Photobiol. A-Chem.* **2000,** *134*, (1-2), 139-142.

(15) Wepasnick, K. A.; Smith, B. A.; Schrote, K. E.; Wilson, H. K.; Diegelmann, S. R.; Fairbrother, D. H., Surface and structural characterization of multi-walled carbon nanotubes following different oxidative treatments. *Carbon* **2011,** *49*, (1), 24-36.

(16) Langley, L. A.; Villanueva, D. E.; Fairbrother, D. H., Quantification of surface oxides on carbonaceous materials. *Chem. Mat.* **2006,** *18*, (1), 169-178.

(17) Holthoff, H.; Egelhaaf, S. U.; Borkovec, M.; Schurtenberger, P.; Sticher, H., Coagulation rate measurements of colloidal particles by simultaneous static and dynamic light scattering. *Langmuir* **1996,** *12*, (23), 5541-5549.

(18) Schudel, M.; Behrens, S. H.; Holthoff, H.; Kretzschmar, R.; Borkovec, M., Absolute aggregation rate constants of hematite particles in aqueous suspensions: A comparison of two different surface morphologies. *Journal of Colloid and Interface Science* **1997,** *196*, (2), 241-253.

(19) Chen, K. L.; Elimelech, M., Aggregation and deposition kinetics of fullerene (C-60) nanoparticles. *Langmuir* **2006,** *22*, (26), 10994-11001.

(20) Saleh, N. B.; Pfefferle, L. D.; Elimelech, M., Aggregation Kinetics of Multiwalled Carbon Nanotubes in Aquatic Systems: Measurements and Environmental Implications. *Environ. Sci. Technol.* **2008,** *42*, (21), 7963-7969.

(21) Saleh, N. B.; Pfefferle, L. D.; Elimelech, M., Influence of Biomacromolecules and Humic Acid on the Aggregation Kinetics of Single-Walled Carbon Nanotubes. *Environ. Sci. Technol.* **2010,** *44*, (7), 2412-2418.

(22) Smith, B.; Wepasnick, K.; Schrote, K. E.; Bertele, A. H.; Ball, W. P.; O'Melia, C.; Fairbrother, D. H., Colloidal Properties of Aqueous Suspensions of Acid-Treated, Multi-Walled Carbon Nanotubes. *Environ. Sci. Technol.* **2009,** *43*, (3), 819-825.

(23) Smith, B.; Wepasnick, K.; Schrote, K. E.; Cho, H. H.; Ball, W. P.; Fairbrother, D. H., Influence of Surface Oxides on the Colloidal Stability of Multi-Walled Carbon Nanotubes: A Structure-Property Relationship. *Langmuir* **2009,** *25*, (17), 9767-9776.

(24) Yi, P.; Chen, K. L., Influence of Surface Oxidation on the Aggregation and Deposition Kinetics of Multiwalled Carbon Nanotubes in Monovalent and Divalent Electrolytes. *Langmuir* **2011,** *27*, (7), 3588-3599.

(25) Sauerbrey, G., Verwendung Von Schwingquarzen Zur Wagung Dunner Schichten Und Zur Mikrowagung. *Zeitschrift Fur Physik* **1959,** *155*, (2), 206-222.

(26) Matsumoto, Y.; Koinuma, M.; Ida, S.; Hayami, S.; Taniguchi, T.; Hatakeyama, K.; Tateishi, H.; Watanabe, Y.; Amano, S., Photoreaction of Graphene Oxide Nanosheets in Water. *J. Phys. Chem. C* **2011,** *115*, (39), 19280-19286.

(27) Joshi, A.; Punyani, S.; Bale, S. S.; Yang, H. C.; Borca-Tasciuc, T.; Kane, R. S., Nanotube-assisted protein deactivation. *Nat. Nanotechnol.* **2008,** *3*, (1), 41-45.

(28) Latch, D. E.; McNeill, K., Microheterogeneity of singlet oxygen distributions in irradiated humic acid solutions. *Science* **2006,** *311*, (5768), 1743-1747.

(29) Hassett, J. P., Chemistry - Dissolved natural organic matter as a microreactor. *Science* **2006,** *311*, (5768), 1723-1724.

(30) Wilkinson, F.; Helman, W. P.; Ross, A. B., Rate constants for the decay and reactions of the lowest electronically excited singlet state of molecular oxygen in solution. An expanded and revised compilation. *J. Phys. Chem. Ref. Data* **1995,** *24*, (2).

(31) Fox, M. A.; Dulay, M. T., HETEROGENEOUS PHOTOCATALYSIS. *Chem. Rev.* **1993,** *93*, (1), 341-357.

(32) Grandbois, M.; Latch, D. E.; McNeill, K., Microheterogeneous Concentrations of Singlet Oxygen in Natural Organic Matter Isolate Solutions. *Environ. Sci. Technol.* **2008,** *42*, (24), 9184-9190.

(33) Dukovic, G.; White, B. E.; Zhou, Z. Y.; Wang, F.; Jockusch, S.; Steigerwald, M. L.; Heinz, T. F.; Friesner, R. A.; Turro, N. J.; Brus, L. E., Reversible surface oxidation and efficient luminescence quenching in semiconductor single-wall carbon nanotubes. *J. Am. Chem. Soc.* **2004,** *126*, (46), 15269-15276.

(34) Chan, S. P.; Chen, G.; Gong, X. G.; Liu, Z. F., Oxidation of carbon nanotubes by singlet O-2. *Phys. Rev. Lett.* **2003,** *90*, (8).

(35) Alvarez, N. T.; Kittrell, C.; Schmidt, H. K.; Hauge, R. H.; Engel, P. S.; Tour, J. M., Selective Photochemical Functionalization of Surfactant-Dispersed Single Wall Carbon Nanotubes in Water. *J. Am. Chem. Soc.* **2008,** *130*, (43), 14227-14233.

(36) Buxton, G. V.; Greenstock, C. L.; Helman, W. P.; Ross, A. B., CRITICAL-REVIEW OF RATE CONSTANTS FOR REACTIONS OF HYDRATED ELECTRONS, HYDROGEN-ATOMS AND HYDROXYL RADICALS (.OH/.O-) IN AQUEOUS-SOLUTION. *J. Phys. Chem. Ref. Data* **1988,** *17*, (2), 513-886.

(37) Li, W.; Bai, Y.; Zhang, Y. K.; Sun, M. L.; Cheng, R. M.; Xu, X. C.; Chen, Y. W.; Mo, Y. J., Effect of hydroxyl radical on the structure of multi-walled carbon nanotubes. *Synth. Met.* **2005,** *155*, (3), 509-515.

(38) Zhang, X. W.; Lei, L. C.; Xia, B.; Zhang, Y.; Fu, J. L., Oxidization of carbon nanotubes through hydroxyl radical induced by pulsed O(2) plasma and its application for O(2) reduction in electro-Fenton. *Electrochim. Acta* **2009,** *54*, (10), 2810-2817.

(39) Graupner, R., Raman spectroscopy of covalently functionalized single-wall carbon nanotubes. *J. Raman Spectrosc.* **2007,** *38*, (6), 673-683.

(40) Salzmann, C. G.; Llewellyn, S. A.; Tobias, G.; Ward, M. A. H.; Huh, Y.; Green, M. L. H., The role of carboxylated carbonaceous fragments in the functionalization and spectroscopy of a single-walled carbon-nanotube material. *Adv. Mater.* **2007,** *19*, (6), 883-+.

(41) Simmons, J. M.; Nichols, B. M.; Baker, S. E.; Marcus, M. S.; Castellini, O. M.; Lee, C. S.; Hamers, R. J.; Eriksson, M. A., Effect of ozone oxidation on single-walled carbon nanotubes. *J. Phys. Chem. B* **2006,** *110*, (14), 7113-7118.

(42) Qui, N. V.; Scholz, P.; Krech, T.; Keller, T. F.; Pollok, K.; Ondruschka, B., Multiwalled carbon nanotubes oxidized by UV/H(2)O(2) as catalyst for oxidative dehydrogenation of ethylbenzene. *Catal. Commun.* **2011,** *12*, (6), 464-469.

(43) Martinez, M. T.; Callejas, M. A.; Benito, A. M.; Cochet, M.; Seeger, T.; Anson, A.; Schreiber, J.; Gordon, C.; Marhic, C.; Chauvet, O.; Fierro, J. L. G.; Maser, W. K., Sensitivity of single wall carbon nanotubes to oxidative processing: structural modification, intercalation and functionalisation. *Carbon* **2003,** *41*, (12), 2247-2256.

(44) Reber, J. F.; Meier, K., PHOTOCHEMICAL PRODUCTION OF HYDROGEN WITH ZINC-SULFIDE SUSPENSIONS. *J. Phys. Chem.* **1984,** *88*, (24), 5903-5913.

(45) Elimelech, M.; Gregory, J.; Jia, X.; Williams, R. A., Particle Deposition and Aggregation: Measurement, Modelling and Simulation. *Oxford, UK* **1995**.

(46) Petosa, A. R.; Jaisi, D. P.; Quevedo, I. R.; Elimelech, M.; Tufenkji, N., Aggregation and Deposition of Engineered Nanomaterials in Aquatic Environments: Role of Physicochemical Interactions. *Environ. Sci. Technol.* **2010,** *44*, (17), 6532-6549.

(47) Chen, K. L.; Elimelech, M., Relating Colloidal Stability of Fullerene (C-60) Manoparticles to Nanoparticle Charge and Electrokinetic Properties. *Environmental Science & Technology* **2009,** *43*, (19), 7270-7276.

(48) Verwey, E. J. W., Theory of the Stability of Lyophobic Colloids. *Philips Research Reports* **1945,** *1*, (1), 33-49.

(49) Derjaguin, B.; Landau, L., Theory of stability of highly charged liophobic sols and adhesion of highly charged particles in solutions of electrolytes. *Zhurnal Eksperimentalnoi Teor. Fiz.* **1945,** *15*, (11), 663-682.

Chapter 4: Impact of Sunlight and Humic Acid on the Aggregation Kinetics of Aqueous Fullerene Nanoparticles (nC_{60})

4.1 Introduction

Buckminsterfullerene (C_{60}), as another major CNM, has also drawn much attention due to its unique physicochemical properties such as antioxidative properties, photoactivity, hydrophobicity, the spherical cage structure, and high electron affinity, which could enable a wide range of potential applications including optics, cosmetics and pharmaceuticals.[1] The current and potential use in consumer products and large-scale production of fullerene C_{60} will inevitably lead to its release into the environment. Modeling studies predicted the concentrations of fullerenes at the order of magnitude of ng/L ~ μg/L in surface waters and μg/L in wastewater treatment plant effluents.[2] Because C_{60} as a molecule has extremely low solubility in water,[3, 4] the nano-sized colloidal particle of C_{60} formed in the aqueous phase, usually referred to as nC_{60}, is considered a more environmentally relevant form of fullerene. Many studies showed that nC_{60} can exert toxicity to various organisms such as bacteria, fish and human cell lines,[5-7] raising concerns regarding its potential impact to human and ecosystem health. Initial studies postulated that ROS generation is one of the major toxicity mechanisms involved.[8, 9] However, reports on the ROS generation of nC_{60} were contradictory. Several studies reported minimal to no ROS production by aqueous nC_{60} due to self-quenching.[10, 11] Thus it has been suggested that the toxicity of nC_{60} stems from ROS-independent oxidative stress.[12, 13]

Unlike conventional contaminants such as dissolved organic compounds and heavy metals, the fate and transport of nanoparticles are largely controlled by aggregation and deposition processes [14]. nC_{60} aggregation behavior in different electrolyte solutions has been quantitatively studied [15-17]. These studies suggest that pristine nC_{60} stability can be adequately described by the traditional DLVO theory [18, 19]. Compared to monovalent cations, divalent cations are much more efficient in coagulating nC_{60} as described by the Schulze-Hardy Rule [16, 20].

NOM, ubiquitous in aquatic environment and soils, is one of the key factors governing the environmental transport and fate of colloids. NOM can adsorb onto colloidal particles, alter their surface properties and consequently affect their transport patterns. The capability of adsorbed NOM to stabilize colloids such as nC_{60}, hematite, magnetite and clay particles is well recognized [16, 21-23]. The steric hindrance effect has been reported to be responsible for the enhanced nC_{60} stability in the presence of humic acid [16].

Because nC_{60} can remain suspended for an extended period of time at the ionic strength and pH found in surface waters [17, 24], exposure to sunlight could be an important process that affects its environmental fate. C_{60} has strong light absorption within the solar spectrum, especially in the UV range. Recent studies demonstrated that nC_{60} undergoes surface modification or decomposition under sunlight or UV irradiation [25-27]. Oxygen-containing functional groups were identified on the irradiated nC_{60} particle surface. These studies suggest that surface oxidized nC_{60} may be an important form of C_{60} in the aquatic environment. In addition, a recent study on the aggregation behavior of MWCNTs suggests that oxygen-containing surface functional groups may have a great impact on

the aggregation of carbon nanomaterials. A positive linear relationship was found between the CCC of the MWCNT and its total oxygen content [28]. However, little is known about the transport of photochemically modified nC_{60}.

This chapter addresses the effect of solar irradiation on the aggregation kinetics of nC_{60}. Exposure of nC_{60} to sunlight was simulated by UVA irradiation and its impact on nC_{60} aggregation was investigated in solutions varying in total ionic strength, cationic species, and organic content. This is the first report on the aggregation behavior of nC_{60} photochemically modified by sunlight. Our results suggest that sunlight may play a critical role in the environmental fate and transport of C_{60}.

4.2 Materials and Methods

4.2.1 Materials. Sublimed C_{60} powder (purity greater than 99%) was obtained from Materials Electronics Research Corporation (Tucson, Arizona). Suwannee River humic acid standard (II) (SRHA, International Humic Substances Society, Atlanta, Georgia) was used as the surrogate for aquatic NOM. The SRHA powder (100 mg) was dissolved in 100 mL DI water and stirred for 24 h in dark. The pH was adjusted to 8.5 with NaOH to aid the dissolution of SRHA. The stock solution was then filtered through 0.45 μm-pore-size Whatman membrane filters to remove undissolved SRHA. The concentration of the stock solution, 894 mg/L (470 mg/L as carbon), was determined by total organic carbon (TOC) analysis using a high sensitivity TOC analyzer (Shimadzu Scientific Instruments, Columbia, MD) based on the carbon content (52.6%) of SRHA [29]. Reagent-grade NaCl and $CaCl_2$ were obtained from Aldrich Chemicals (Milwaukee, Wisconsin).

4.2.2 Preparation of nC_{60} Stock Suspension. The aqueous nC_{60} stock suspension was prepared by direct sonication [27]. Sublimed C_{60} was pulverized into fine powder and 150 mg of this powder was added to 200 mL deionized water in a 500 mL glass beaker. The mixture was then put in an ice bath and sonicated with a sonicating probe (Vibra-Cell VCX 500, Sonics & Material, Newtown, CT) at 100 W for 30 min. After sonication, the mixture was filtered through 2 μm-pore-size Millex-AP membrane filters (Millipore, Billerica, MA) to remove large particles. All filters were washed with 10 mL DI water before use and replaced after 30 mL of filtrate was collected. The resulting clear yellow suspension was stored in dark at 4 °C until use. The C_{60} concentration in the stock suspension was 4.4 mg/L as determined by TOC measurement. All experiments were performed using the same stock suspension. Particle size of the stock suspension was routinely monitored over the period of the study (3 months); there were no detectable changes.

4.2.3 Irradiation Experiments. Irradiation experiments were carried out in a Luzchem LZC-4V Photoreactor (Luzchem, Ottawa, Ontario, Canada). Because UVA is the primary component of UV light in the solar irradiation that can reach the earth surface, a light source in the UVA wavelength range was employed to mimic the UV fraction of the solar spectrum. Four 8W black lamps (Hitachi FL8BL-B, $\lambda = 350 \pm 50$ nm), two on each side, provided approximately 2 mW/cm^2 (1.66 mW/cm^2 after absorption by the sample flask) of light intensity at the center of the reactor as measured by a radiometer (Control Company, Friendwoods, TX), comparable to the UVA intensity measured at the ground level on a sunny summer day in Houston, Texas. In each experiment, 30 mL of the nC_{60} stock suspension at unadjusted pH 6.3 was added to a 50

mL Erlenmeyer flask, sealed with parafilm with vents, placed on the merry-go-round at the center of the photoreactor, and slowly rotated to ensure uniform exposure. Samples were withdrawn on day 1, 2, 3 and 7, and stored in dark at 4 ºC before testing.

Physical and chemical properties of the irradiated nC_{60} suspension were thoroughly characterized by TEM, XPS, attenuated total reflectance Fourier transform infrared (ATR-FTIR) spectroscopy, and UV/Vis spectroscopy as in our previous study [27].

4.2.4 Characterization of Particle Size and Electrophoretic Mobility. Particle sizes of the pristine and irradiated nC_{60} were determined by DLS measurement using a ZEN 3600 Zetasizer Nano (Malvern, Worcestershire, UK) equipped with a monochromatic coherent He-Ne laser with a fixed wavelength of 633 nm. The intensity of scattered light was measured at 173° and the refractive index of nC_{60} was set at 2.20 [30]. Each sample was measured consecutively 6 times for the hydrodynamic radius. Particle EPM was measured by PALS using the ZEN 3600 Zetasizer Nano (Malvern, Worcestershire, UK). Measurements were carried out using folded capillary cells (Malvern, Worcestershire, UK) and 10 measurements were made for each sample. All size and EPM measurements were conducted at 23 °C.

4.2.5 nC_{60} Aggregation Kinetics. *Measurement of particle aggregation rate.* Aggregation of the pristine and irradiated nC_{60} suspensions in various solution conditions was characterized by monitoring the intensity weighted average particle size as a function of time via time-resolved DLS measurement. For experiments without humic acid, 0.25 mL of the nC_{60} stock suspension, predetermined amount of the electrolyte stock solution and DI water were introduced into a disposable polystyrene cuvette (Sarstedt, Germany)

to create a sample with a total volume of 1 mL and nC_{60} concentration of 1.1 mg/L. The sample was briefly mixed and immediately analyzed. The auto-correlation function was applied to data collected every 15 s. Since initiation of the instrument took 1 min, the first particle size datum was collected at 75 s after the nC_{60} suspension was mixed with the electrolyte solution.

For most experiments with humic acid, 5 mL nC_{60} stock suspension was pre-contacted with 5 mL SRHA solution at the same concentration as that used in the subsequent DLS measurement in a glass vial on a shaker bed for 24 h to allow adsorption. This mixture was then combined with the background solution containing the corresponding electrolyte and SRHA to form samples with 1.1 mg/L nC_{60} and 1 mg/L or 10 mg/L SRHA in 1 mL total volume. Selected experiments were also performed without SRHA pre-contact and compared with those with pre-contact to investigate the impact of SRHA adsorption dynamics.

Determination of aggregation kinetics. The rate of initial increase in the intensity weighted average hydrodynamic radius $a_h(t)$ determined by linear regression of the aggregation curve was used to represent the initial aggregation rate. Extrapolation of the aggregation data to time zero shows that the estimated particle size at time zero was similar for all experiments (average 86.5 ± 2.8 nm in NaCl and 86.9 ± 2.1 nm in $CaCl_2$) and close to that measured in DI water (82.3 ± 0.9 nm). This indicates that there were no significant changes in aggregation rate in the first 75 s, during which particle size data were not available, suggesting that the aggregation rate obtained represents the initial aggregation rate.

The attachment efficiency α is defined as the aggregation rate constant in the solution of interest normalized by the rate constant in the diffusion-limited regime, where the aggregation rate constant is independent of electrolyte concentration [15]. In our analysis, the diffusion-limited aggregation rate was determined by averaging the aggregation rates of all aggregation kinetic curves obtained in the diffusion-limited regime. Stability curves were constructed by plotting the α value as a function of the background electrolyte concentration. For easy comparison, the diffusion-limited aggregation rate determined for the pristine nC_{60} in the absence of SRHA was used as the diffusion-limited aggregation rate for all the stability curves in the same electrolyte. The CCC was approximated by the electrolyte concentration at the intersection of the reaction-limited stability curve and the diffusion-limited stability curve (as shown in Figures 4.1 and 4.4).

4.3 Result and Discussion

4.3.1 Characterization of nC_{60} Nanoparticles. The number mean and Z-average hydrodynamic radii of the pristine nC_{60} suspension were 54.8 $\pm$ 2.4 nm and 82.3 $\pm$ 0.9 nm respectively. The particles were highly negatively charged with an electrophoretic mobility of -3.34 $\pm$ 0.13 $\times 10^{-8}$ m^2 V^{-1} s^{-1} in 1 mM NaCl. The surface chemical properties of irradiated nC_{60} suspension prepared using the same protocol was thoroughly characterized in our previous study [27]. Mono-oxygenated carbon (C-O) and dioxygenated carbon (C=O or O-C-O) accounted for 19 and 15%, respectively, of the total carbon on the 7-day irradiated-nC_{60} surface. ATR-FTIR analyses confirmed surface oxygenation and hydroxylation. After 7 days of UVA irradiation, both the number mean particle size in DI water (54.7 $\pm$ 3.6 nm) and the electrophoretic mobility in 1 mM NaCl (-3.24 $\pm$

0.19 $\times 10^{-8}$ m^2 V^{-1} s^{-1}) remained unchanged, consistent with previous results [27]. The unchanged particle size suggests that there was no significant release of photochemical oxidation products into the aqueous phase, and the number concentration of nC_{60} was assumed to remain unchanged.

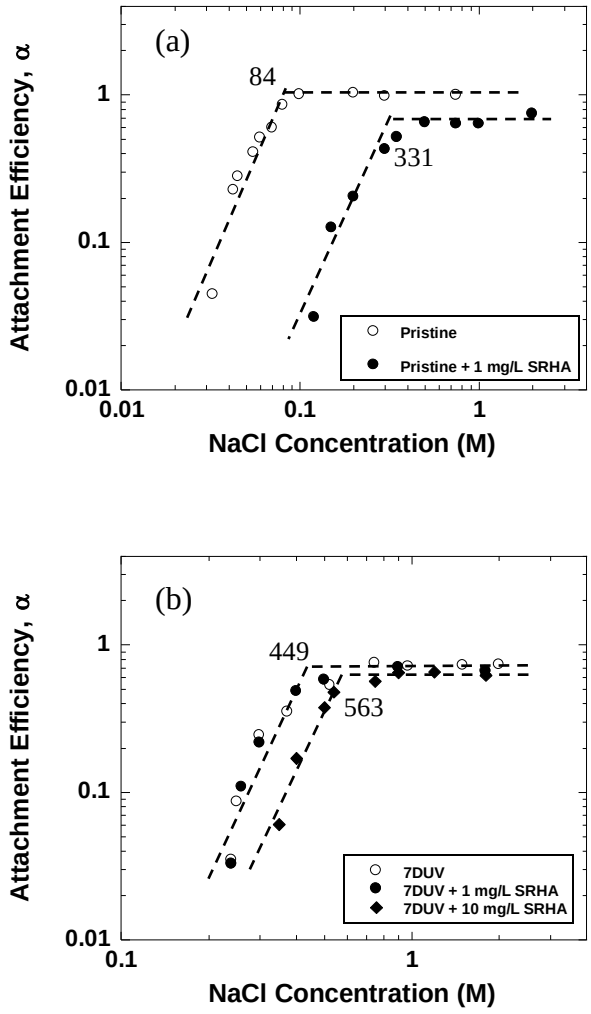

Figure 4.1. Attachment efficiencies of (a) pristine nC_{60} and (b) 7-day UV-irradiated nC_{60} (7DUV) in the absence and presence of SRHA as a function of NaCl concentration at pH 6.0 ± 0.3. Extrapolation of the reaction-limited and diffusion-limited regimes yields the

critical coagulation concentrations (CCC) at the intersections. The CCC values are noted next to the corresponding intersection.

4.3.2 Aggregation Kinetics in NaCl Solutions. The attachment efficiency (α) of nC_{60} in NaCl solutions before and after UV irradiation is shown in Figure 4.1. The pristine nC_{60} nanoparticles were only stable at NaCl concentrations below 20 mM, with a CCC of 84 mM. Our CCC value is lower than those previously reported for nC_{60} prepared by solvent exchange (160 mM NaCl [16] and 120 mM NaCl [15]) or by magnetic stirring (260 mM NaCl [31] and 166 mM KCl [17]), but higher than that (40 mM KCl [17]) of another sonicated nC_{60} that was dissolved in toluene before sonication. After 7 days of UVA irradiation, the stability of nC_{60} nanoparticles (denoted 7DUV-nC_{60}) in NaCl increased drastically (Figure 4.1b), with a CCC of 449 mM NaCl.

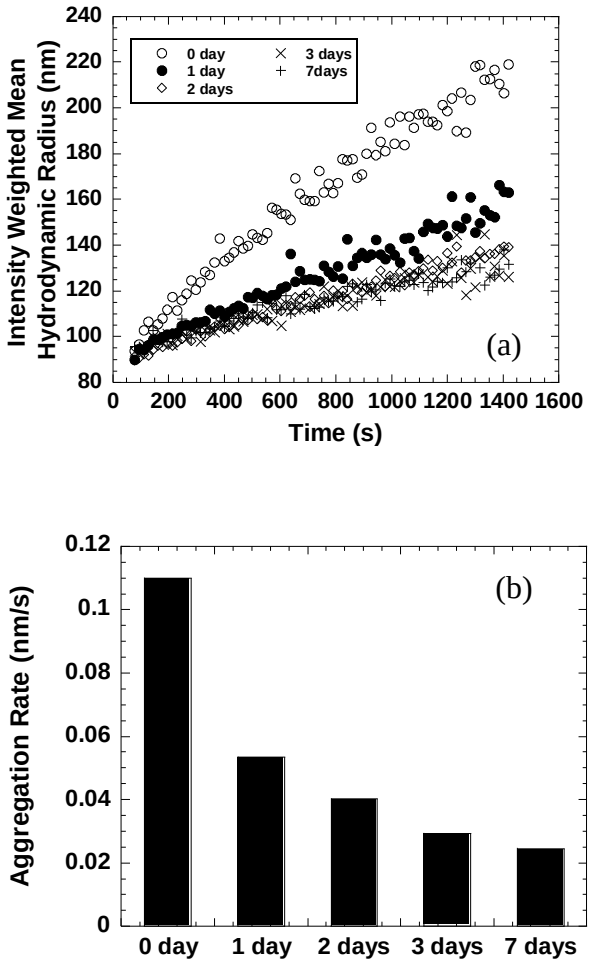

Figure 4.2. (a) Aggregation profiles (b) initial aggregation rate of samples with different UV irradiation time in the presence of 300 mM NaCl at pH 6.0 ± 0.3.

nC_{60} aggregation rate decreased with increasing UV irradiation time during the 7-day period. Figure 4.2 demonstrates the effect of UV irradiation time on the aggregation kinetics of nC_{60} in 300 mM NaCl. After 7 days of UVA irradiation, the initial aggregation rate dropped from 0.110 to 0.024 nm/s. Such increase in stability is attributed to the presence of oxygen-containing functional groups on the surface of the irradiated nC_{60} particles [26, 27]. Similar effects of surface oxygen-containing functional groups were reported for nC_{60} prepared by long-term stirring and carbon nanotubes oxidized by acid

wash; these effects were related to the extent of surface oxidation and resulting changes in surface charge or electrophoretic mobility [17, 28, 32].

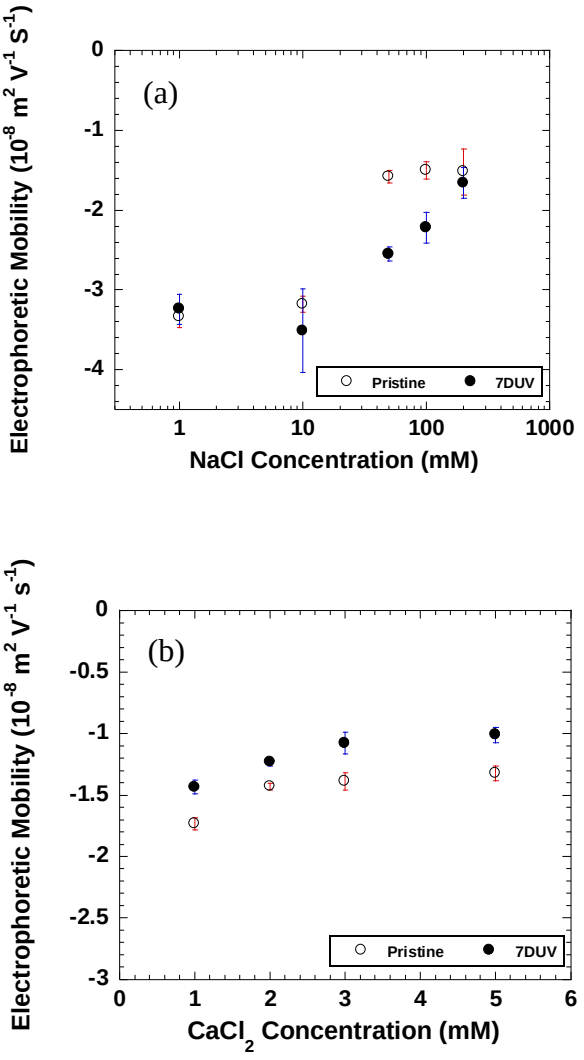

Figure 4.3. Electrophoretic Mobility of pristine nC_{60} and 7-day UV-irradiated nC_{60} (7DUV) as a function of (a) NaCl and (b) $CaCl_2$ concentration at pH 6.0 ± 0.3.

The electrophoretic mobility of nC_{60} before and after UVA irradiation at different NaCl concentrations is compared in Figure 4.3a. For both the pristine and UV irradiated samples, particle electrophoretic mobility became less negative with increasing NaCl

concentration due to charge screening. The pristine nC_{60} and 7DUV-nC_{60} were similarly charged at NaCl concentrations below 10 mM; in the NaCl concentration range of 10-200 mM; however, the 7DUV-nC_{60} surface was notably more negatively charged than the pristine nC_{60}, consistent with the higher colloidal stability. The difference in response to the charge screening effect of NaCl is attributed to the changes in nC_{60} surface chemistry; i.e., addition of oxygen-containing functionalities, during UV irradiation. Differences in electrophoretic mobility were also reported for nC_{60} samples prepared by different protocols [30], and were attributed to differences in surface chemistry. A close examination of the electrophoretic mobility data reveals that changes in particle electrophoretic mobility alone could not account for the observed increase in particle stability after UV irradiation. For example, the electrophoretic mobility of the 7DUV-nC_{60} in 200 mM NaCl was $-1.66 \pm 0.19 \times 10^{-8}$ m^2 V^{-1} s^{-1}, similar to that of the pristine nC_{60} at its CCC of 84 mM NaCl, where rapid aggregation occurred. Nevertheless, the 7DUV-nC_{60} was very stable with an α value less than 0.001 in 200 mM NaCl. Such inconsistency between the electrophoretic mobility and the stability of nanoparticles has also been reported in previous studies on MWCNTs. Smith et al. [28, 32] found that although the CCCs of oxidized MWCNTs increased with increasing surface oxidation, the changes in electrophoretic mobility did not correlate well to the CCCs. This discrepancy was attributed to the fact that electrophoretic mobility reflects the potential at the plane of shear, not the actual surface charge [28]. Another possible reason is that the surface oxygen functional groups increased nC_{60} hydrophilicity and decreased hydrophobic interactions, as described by the extended DLVO theory [33].

As a major component of NOM, humic acid is ubiquitous in the natural aqueous environment. It has a heterogeneous structure with hydrophobic backbones and hydrophilic side chains. Although negatively charged, humic acid can readily adsorb onto colloidal surfaces such as that of nC_{60} via hydrophobic interaction, potentially mediating colloidal aggregation. The capability of adsorbed NOM to stabilize colloids like nC_{60}, hematite, magnetite and clay particles is widely reported [16, 21-23]. As shown in Figure 4.1a, SRHA at 1 mg/L greatly increased the stability of the pristine nC_{60}; the CCC increased from 84 to 331 mM NaCl. On the other hand, the electrophoretic mobility of nC_{60} did not change notably after equilibrating with 1 mg/L SRHA, suggesting that electrostatic interactions were not responsible for the increase in stability. This is consistent with the finding of Chen and Elimelech [16]. The increased stability in the presence of SRHA is attributed to the steric hindrance effect of humic acid molecules adsorbed on nC_{60} surface. With 10 mg/L SRHA, no aggregation of pristine nC_{60} was observed at NaCl concentrations up to 1.5 M NaCl (data not shown). This further demonstrates that steric hindrance rather than electrostatic repulsion is the main stabilizing mechanism in the presence of humic acid, since the surface charge should be effectively screened at such an elevated NaCl concentration.

The effect of humic acid on the stability of 7DUV-nC_{60} (Figure 4.1b) was much weaker. At 1 mg/L SRHA, there was no notable change in particle stability; when SRHA concentration was increased to 10 mg/L, particle stability increased slightly with a CCC of 563 mM compared to 449 mM without humic acid. The small influence of humic acid on the aggregation properties of 7DUV-nC_{60} is attributed to decreased adsorption of humic acid due to increased hydrophilicity of the nC_{60} surface after UV irradiation.

Unlike pristine nC_{60}, which showed significant adsorption of SRHA (q = 1209 mg/kg), UV-irradiated nC_{60} had no detectable adsorption of SRHA during 24 h of contact. These results suggest that the stability of the UV-irradiated nC_{60} depends more on the oxygen-containing surface functional groups than humic acid, and the role of humic acid may be further reduced at longer irradiation time, which increases the level of surface oxidation [27].

Attachment efficiencies in the diffusion-limited regime of the pristine nC_{60} with humic acid (α = 0.66) and the 7DUV-nC_{60} with (α = 0.68) and without humic acid (α = 0.73) were found to be less than unity. The decrease in α in the diffusion-limited regime was reported previously with humic acid in $MgCl_2$ solutions [16] and indicates that the steric hindrance effect, which cannot be eliminated by double layer compression, predominates in stabilizing the pristine nC_{60} at high NaCl concentrations. In the absence of humic acid, however, the less-than-unity α value of the 7DUV-nC_{60} in the diffusion-limited regime indicates that the oxygen-containing surface functional groups formed during UV irradiation can stabilize nC_{60} through mechanisms not eliminated by high NaCl concentration, e.g., increase in surface hydrophilicity.

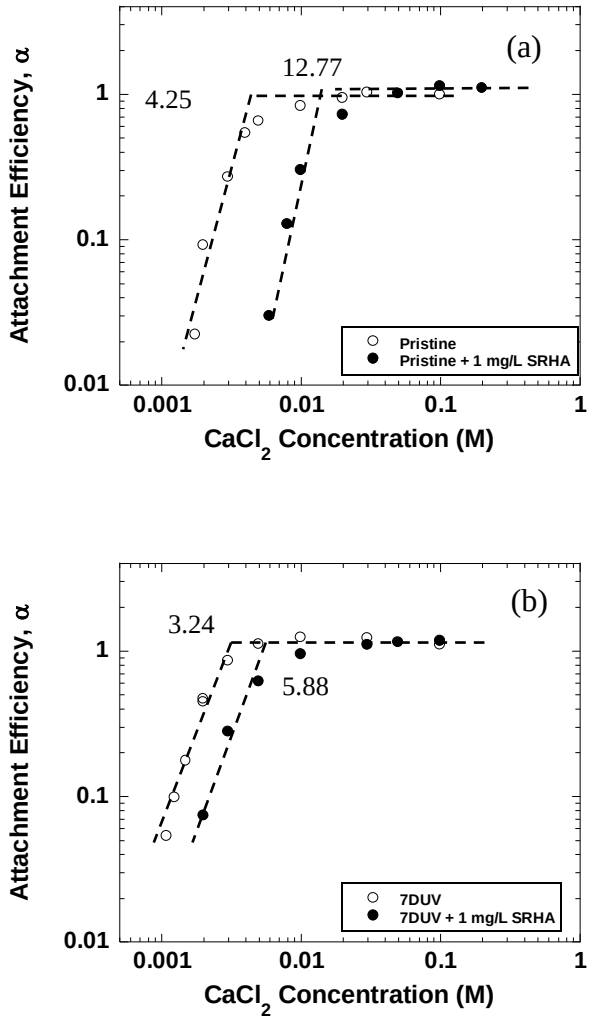

Figure 4.4. Attachment efficiencies of (a) pristine nC_{60} and (b) 7-day UV-irradiated nC_{60} (7DUV) in the absence and presence of SRHA as a function of $CaCl_2$ concentration at pH 6.0 ± 0.3. By extrapolating through reaction-limited and diffusion-limited regimes, the intersections of the extrapolations yield critical coagulation concentrations which are noted aside.

4.3.3 Aggregation Kinetics in $CaCl_2$ Solutions. Colloidal stability depends strongly on the electrolyte valence, as described by the Schulze-Hardy Rule [20]. Cations of higher valence are more efficient in coagulation. As a result, the CCCs of $CaCl_2$ for the

pristine and 7DUV-nC_{60}, 4.25 and 3.24 mM $CaCl_2$, respectively, were markedly lower than those of NaCl. Contrary to the observations in NaCl solutions, the 7DUV-nC_{60} was less stable than the pristine nC_{60} in $CaCl_2$ solutions (Figure 4.4). Comparison between the electrophoretic mobility of the pristine and the 7DUV-nC_{60} reveals that the 7DUV-nC_{60} was less negatively charged than the pristine nC_{60} over the entire tested range of $CaCl_2$ concentrations (Figure 4.3b), suggesting that Ca^{2+} was more effective in neutralizing negative charges on the 7DUV-nC_{60} surface than on the pristine n$C_{60.}$ The Schulze-Hardy Rule predicts that the CCC is proportional to Z^{-6} (Z is the valence of the counter-ion) for surfaces of high charge density [34] and Z^{-2} for surfaces of low charge density [35]. In our experiments, the power term is -4.3 for the pristine nC_{60} and -7.1 for the 7DUV-nC_{60}. The behavior of the pristine nC_{60} agrees with the Schulze-Hardy Rule, while the power term for the 7DUV-nC_{60} is higher than the normal range. Because the Schulze-Hardy Rule holds for indifferent electrolytes that do not form any specific interactions with the colloidal surface, this result indicates that Ca^{2+} specifically interacts with the 7DUV-nC_{60} surface, presumably with carboxyl groups formed from UV irradiation.

The presence of humic acid increased the stability of the pristine nC_{60}, similar to that observed in NaCl solutions. With 1 mg/L SRHA, the CCC for the pristine nC_{60} increased from 4.2 to 12.8 mM $CaCl_2$. This is attributed to the steric hindrance effect of the adsorbed humic acid. The 7DUV-nC_{60}, however, behaved differently in $CaCl_2$ than in NaCl solutions: With 1 mg/L humic acid, the CCC increased from 3.24 to 5.88 mM $CaCl_2$, indicating adsorption of humic acid on the 7DUV-nC_{60} particle surface; the effect of humic acid at the same concentration in NaCl solutions was undetectable. This suggests that Ca^{2+} may have facilitated humic acid adsorption onto the 7DUV-nC_{60}

surface. Enhanced humic acid adsorption could occur through two potential mechanisms: 1) Ca^{2+} specifically interacts with the oxygen-containing function groups (e.g., carboxyl groups) on the 7DUV-nC_{60} surface, neutralizing surface negative charges as demonstrated by the less negative EPM (Figure 4.3b); it complexes with humic acid and reduces its molecular charge [36]. Consequently, the electrostatic repulsion between the 7DUV-nC_{60} and humic acid is reduced, favoring humic acid adsorption. 2) Ca^{2+} could form ionic bridges between humic acid and the oxygen-containing functional groups on the 7DUV-nC_{60}, an effect that has been reported in studies on humic acid adsorption onto mineral surfaces [37-40].

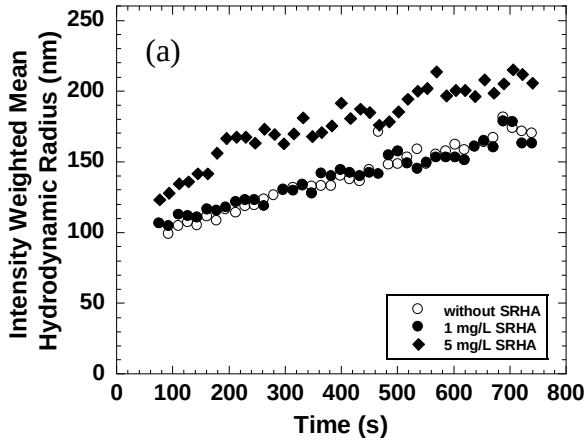

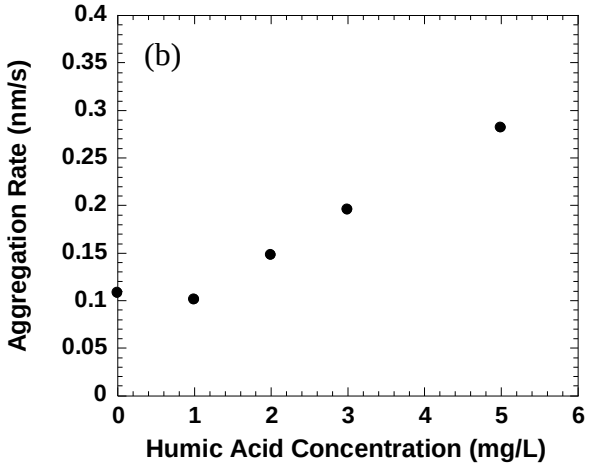

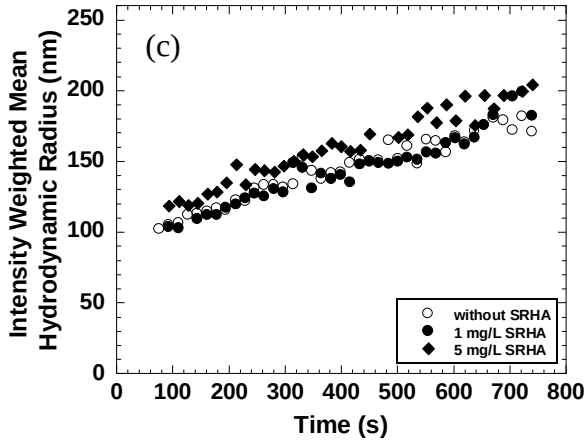

Figure 4.5. (a) Aggregation profiles of pristine nC_{60} in the absence and presence of humic acid without pre-contact; (b) Aggregation rate as a function of humic acid concentration without pre-contact; (c) Aggregation profiles of pristine nC_{60} in the absence and presence of humic acid with 24 h pre-contact. Measurements were conducted in 200 mM $CaCl_2$.

The dynamics of the contact between nC_{60} and humic acid was found to affect the aggregation behavior in the diffusion-limited regime. Figure 4.5 compares the aggregation rate of SRHA precoated pristine nC_{60} and that of nC_{60} simultaneously mixed with SRHA and the background $CaCl_2$ solution. All the experiments were conducted in 200 mM $CaCl_2$ to ensure that the aggregation is diffusion-limited. When pristine nC_{60} and SRHA at a concentration higher than 1 mg/L were introduced to the $CaCl_2$ solution simultaneously just before DLS measurement, the nC_{60} aggregation rate was significantly higher than that in the absence of SRHA (Figure 4.5a) and the initial aggregation rate increased with increasing SRHA concentration (Figure 4.5b). A similar effect was reported in a previous study [16] using nC_{60} synthesized by solvent exchange, and was attributed to the bridging of nC_{60} by humic acid aggregates. Interestingly, when the pristine nC_{60} was pre-contacted with SRHA for 24 hours, the diffusion-limited

aggregation rate was independent of SRHA concentration (Figure 4.5c). These results suggest that SRHA aggregation in the presence of Ca^{2+} is faster than SRHA adsorption onto nC_{60} and that once precoated with humic acid, nC_{60} does not attach to humic acid aggregates.

4.4 Conclusion

The transport and fate of nC_{60} is affected by multiple environmental factors, including sunlight and natural organic matter. In this chapter, the initial aggregation kinetics of nC_{60} before and after UVA irradiation was investigated in solutions varying in ionic strength, ionic composition and humic acid concentration. In NaCl solutions, surface oxidation induced by UV irradiation remarkably increased nC_{60} stability due to the increased negative surface charge and reduced particle hydrophobicity; while humic acid greatly enhanced the stability of pristine nC_{60} via the steric hindrance effect, it had little influence on the stability of UV-irradiated nC_{60} in NaCl due to reduced adsorption on oxidized nC_{60} surface. In contrast, UV irradiation reduced nC_{60} stability in $CaCl_2$ due to specific interactions of Ca^{2+} with the negatively charged functional groups on UV-irradiated nC_{60} surface and the consequent charge neutralization. By neutralizing surface charges of both UV-irradiated nC_{60} and humic acid as well as forming intermolecular bridges, Ca^{2+} facilitated humic acid adsorption on UV-irradiated nC_{60}, resulting in enhanced stability in the presence of humic acid.

While the stability of the pristine nC_{60} is largely controlled by the humic acid adsorbed on the nC_{60} surface, humic acid adsorption is mediated by the oxygen-containing surface functionality on the UV-irradiated nC_{60} particles. On the other hand,

the extent of nC_{60} photochemical transformation is strongly influenced by humic acid [27]. In addition, specific interactions between cationic species such as Ca^{2+} and nC_{60} surface functionality resulting from UV irradiation or humic acid adsorption can be a dominating factor in nC_{60} aggregation kinetics. These findings suggest that a better quantitative understanding of the dynamics of nC_{60} surface chemistry change is critical to predicting fullerene transport and fate in the aqueous environment as well as risk assessment for carbon based nanomaterials.

Part of this chapter has been published and reprinted with permission from: Qu, X.L., Hwang, Y.S., Alvarez, P.J.J., Bouchard, D. and Li, Q.L. UV Irradiation and Humic Acid Mediate Aggregation of Aqueous Fullerene (nC_{60}) Nanoparticles. ***Environmental Science & Technology*** 44(20), 7821-7826. **2010**. Copyright 2013 American Chemical Society.

4.5 References

(1) Nakamura, E.; Isobe, H., Functionalized fullerenes in water. The first 10 years of their chemistry, biology, and nanoscience. *Accounts Chem. Res.* **2003,** *36*, (11), 807-815.

(2) Aschberger, K.; Micheletti, C.; Sokull-Kluttgen, B.; Christensen, F. M., Analysis of currently available data for characterising the risk of engineered nanomaterials to the environment and human health - Lessons learned from four case studies. *Environment international* **2011,** *37*, (6), 1143-56.

(3) Heymann, D., Solubility of fullerenes C60 and C70 in seven normal alcohols and their deduced solubility in water. *Fullerene Science & Technology* **1996,** *4*, (3), 509-515.

(4) Jafvert, C. T.; Kulkarni, P. P., Buckminsterfullerene's (C(60)) octanol-water partition coefficient (K(ow)) and aqueous solubility. *Environ. Sci. Technol.* **2008,** *42*, (16), 5945-5950.

(5) Fang, J. S.; Lyon, D. Y.; Wiesner, M. R.; Dong, J. P.; Alvarez, P. J. J., Effect of a fullerene water suspension on bacterial phospholipids and membrane phase behavior. *Environ. Sci. Technol.* **2007,** *41*, (7), 2636-2642.

(6) Zhu, S. Q.; Oberdorster, E.; Haasch, M. L., Toxicity of an engineered nanoparticle (fullerene, C-60) in two aquatic species, Daphnia and fathead minnow. *Mar. Environ. Res.* **2006,** *62*, S5-S9.

(7) Sayes, C. M.; Fortner, J. D.; Guo, W.; Lyon, D.; Boyd, A. M.; Ausman, K. D.; Tao, Y. J.; Sitharaman, B.; Wilson, L. J.; Hughes, J. B.; West, J. L.; Colvin, V. L., The differential cytotoxicity of water-soluble fullerenes. *Nano Lett.* **2004,** *4*, (10), 1881-1887.

(8) Markovic, Z.; Todorovic-Markovic, B.; Kleut, D.; Nikolic, N.; Vranjes-Djuric, S.; Misirkic, M.; Vucicevic, L.; Janjetovic, K.; Isakovic, A.; Harhaji, L.; Babic-Stojic, B.; Dramicanin, M.; Trajkovic, V., The mechanism of cell-damaging reactive oxygen generation by colloidal fullerenes. *Biomaterials* **2007,** *28*, (36), 5437-5448.

(9) Sayes, C. M.; Gobin, A. M.; Ausman, K. D.; Mendez, J.; West, J. L.; Colvin, V. L., Nano-C-60 cytotoxicity is due to lipid peroxidation. *Biomaterials* **2005,** *26*, (36), 7587-7595.

(10) Lee, J.; Yamakoshi, Y.; Hughes, J. B.; Kim, J. H., Mechanism of C-60 photoreactivity in water: Fate of triplet state and radical anion and production of reactive oxygen species. *Environ. Sci. Technol.* **2008,** *42*, (9), 3459-3464.

(11) Lee, J.; Fortner, J. D.; Hughes, J. B.; Kim, J. H., Photochemical production of reactive oxygen species by C-60 in the aqueous phase during UV irradiation. *Environ. Sci. Technol.* **2007,** *41*, (7), 2529-2535.

(12) Lyon, D. Y.; Brunet, L.; Hinkal, G. W.; Wiesner, M. R.; Alvarez, P. J. J., Antibacterial activity of fullerene water suspensions (nC(60)) is not due to ROS-mediated damage. *Nano Lett.* **2008,** *8*, (5), 1539-1543.

(13) Lyon, D. Y.; Alvarez, P. J. J., Fullerene Water Suspension (nC(60)) Exerts Antibacterial Effects via ROS-Independent Protein Oxidation. *Environ. Sci. Technol.* **2008,** *42*, (21), 8127-8132.

(14) Qu, X. L.; Alvarez, P. J. J.; Li, Q. L. *Review of Nanomaterial Research and Relevance for Water Reuse*; In press.

(15) Chen, K. L.; Elimelech, M., Aggregation and deposition kinetics of fullerene (C-60) nanoparticles. *Langmuir* **2006,** *22*, (26), 10994-11001.

(16) Chen, K. L.; Elimelech, M., Influence of humic acid on the aggregation kinetics of fullerene (C-60) nanoparticles in monovalent and divalent electrolyte solutions. *J. Colloid Interface Sci.* **2007,** *309*, (1), 126-134.

(17) Chen, K. L.; Elimelech, M., Relating Colloidal Stability of Fullerene (C-60) Manoparticles to Nanoparticle Charge and Electrokinetic Properties. *Environ. Sci. Technol.* **2009,** *43*, (19), 7270-7276.

(18) Verwey, E. J. W., Theory of the Stability of Lyophobic Colloids. *Philips Research Reports* **1945,** *1*, (1), 33-49.

(19) Derjaguin, B.; Landau, L., Theory of stability of highly charged liophobic sols and adhesion of highly charged particles in solutions of electrolytes. *Zhurnal Eksperimentalnoi Teor. Fiz.* **1945,** *15*, (11), 663-682.

(20) Hardy, W. B., "A preliminary investigation of the conditions which determine the stability of irreversible hydrosols ". *Proc. R. Soc. London* **1900,** *66*, (426), 110-125.

(21) Tipping, E.; Higgins, D. C., The Effect of Adsorbed Humic Substances on the Colloid Stability of Hematite Particles. *Colloids Surfaces* **1982,** *5*, (2), 85-92.

(22) Heidmann, I.; Christl, I.; Kretzschmar, R., Aggregation kinetics of kaolinite-fulvic acid colloids as affected by the sorption of Cu and Pb. *Environ. Sci. Technol.* **2005,** *39*, (3), 807-813.

(23) Illes, E.; Tombacz, E., The effect of humic acid adsorption on pH-dependent surface charging and aggregation of magnetite nanoparticles. *J. Colloid Interface Sci.* **2006,** *295*, (1), 115-123.

(24) Gao, J.; Youn, S.; Hovsepyan, A.; Llaneza, V. L.; Wang, Y.; Bitton, G.; Bonzongo, J. C. J., Dispersion and Toxicity of Selected Manufactured Nanomaterials in Natural River Water Samples: Effects of Water Chemical Composition. *Environ. Sci. Technol.* **2009,** *43*, (9), 3322-3328.

(25) Hou, W. C.; Jafvert, C. T., Photochemical Transformation of Aqueous C-60 Clusters in Sunlight. *Environ. Sci. Technol.* **2009,** *43*, (2), 362-367.

(26) Lee, J.; Cho, M.; Fortner, J. D.; Hughes, J. B.; Kim, J. H., Transformation of Aggregate C-60 in the Aqueous Phase by UV Irradiation. *Environ. Sci. Technol.* **2009,** *43*, (13), 4878-4883.

(27) Hwang Yu Sik; Qilin, L., Characterizing Photochemical Transformation of Aqueous nC_{60} under Environmentally Relevant Conditions. *Environ. Sci. Technol.* **2010,** *ASAP*, DOI: 10.1021/es903713.

(28) Smith, B.; Wepasnick, K.; Schrote, K. E.; Cho, H. H.; Ball, W. P.; Fairbrother, D. H., Influence of Surface Oxides on the Colloidal Stability of Multi-Walled Carbon Nanotubes: A Structure-Property Relationship. *Langmuir* **2009,** *25*, (17), 9767-9776.

(29) McHedlov-Petrossyan, N. O.; Klochkov, V. K.; Andrievsky, G. V., Colloidal dispersions of fullerene C-60 in water: some properties and regularities of coagulation by electrolytes. *J. Chem. Soc.-Faraday Trans.* **1997,** *93*, (24), 4343-4346.

(30) Brant, J. A.; Labille, J.; Bottero, J. Y.; Wiesner, M. R., Characterizing the impact of preparation method on fullerene cluster structure and chemistry. *Langmuir* **2006,** *22*, (8), 3878-3885.

(31) Bouchard, D.; Ma, X.; Issacson, C., Colloidal Properties of Aqueous Fullerenes: Isoelectric Points and Aggregation Kinetics of C-60 and C-60 Derivatives. *Environ. Sci. Technol.* **2009,** *43*, (17), 6597-6603.

(32) Smith, B.; Wepasnick, K.; Schrote, K. E.; Bertele, A. H.; Ball, W. P.; O'Melia, C.; Fairbrother, D. H., Colloidal Properties of Aqueous Suspensions of Acid-Treated, Multi-Walled Carbon Nanotubes. *Environ. Sci. Technol.* **2009,** *43*, (3), 819-825.

(33) Wu, W.; Giese, R. F.; van Oss, C. J., Stability versus flocculation of particle suspensions in water - correlation with the extended DLVO approach for aqueous systems, compared with classical DLVO theory. *Colloid Surf. B-Biointerfaces* **1999,** *14*, (1-4), 47-55.

(34) Sano, M.; Okamura, J.; Shinkai, S., Colloidal nature of single-walled carbon nanotubes in electrolyte solution: The Schulze-Hardy rule. *Langmuir* **2001,** *17*, (22), 7172-7173.

(35) Elimelech, M.; Gregory, J.; Jia, X.; Williams, R. A., Particle Deposition and Aggregation: Measurement, Modelling and Simulation. *Oxford, UK* **1995**.

(36) Chen, K. L.; Elimelech, M., Interaction of Fullerene (C-60) Nanoparticles with Humic Acid and Alginate Coated Silica Surfaces: Measurements, Mechanisms, and Environmental Implications. *Environ. Sci. Technol.* **2008,** *42*, (20), 7607-7614.

(37) Feng, X. J.; Simpson, A. J.; Simpson, M. J., Chemical and mineralogical controls on humic acid sorption to clay mineral surfaces. *Org. Geochem.* **2005,** *36*, (11), 1553-1566.

(38) Arnarson, T. S.; Keil, R. G., Mechanisms of pore water organic matter adsorption to montmorillonite. *Mar. Chem.* **2000,** *71*, (3-4), 309-320.

(39) Mariquit, E.; Salim, C.; Hinode, H., The Effect of Calcium Ions in the Adsorption and Photocatalytic Oxidation of Humic Acid. *J. Chem. Eng. Jpn.* **2009,** *42*, (7), 538-543.

(40) Mariquit, E. G.; Salim, C.; Hinode, H., The Role of Calcium Ions in the Photocatalytic Oxidation of Humic Acid at Neutral pH. In *Environmental Challenges in the Pacific Basin*, Carpenter, D. O., Ed. Blackwell Publishing: Oxford, 2008; Vol. 1140, pp 389-393.

Chapter 5: Impact of Sunlight and Humic Acid on the Deposition Kinetics of Aqueous Fullerene Nanoparticles (nC_{60})

5.1 Introduction

Other than the aggregation behavior discussed in Chapter 4, the deposition behavior of nC_{60} on natural surfaces is also a key process controlling their environmental transport. A number of studies have investigated the transport of nC_{60} in model porous media as well as natural soils using packed column experiments or QCM-D.[1-10] These studies suggest that the properties of nC_{60} and the collectors, solution chemistry, and hydrodynamic conditions are the major factors governing the deposition process. The deposition of nC_{60} is qualitatively in good agreement with the classic DLVO theory and mostly happens in the primary minimum.[5] However the majority of past studies were carried out with pristine nC_{60} in simple electrolyte solutions. Phototransformation and interactions with NOM could alter the surface chemistry of nC_{60} and consequently confound its deposition behavior.

As discussed in the previous chapter, sunlight exposure leads to surface oxidation of nC_{60} nanoparticles. The oxygen-containing functional groups formed greatly hindered the aggregation of nC_{60} in NaCl solutions due to the increased negative surface charge and hydrophilicity. Ca^{2+} can interact with the functional groups and destabilize UVA-irradiated nC_{60}. Dissolved humic acid has been shown to readily adsorb on pristine nC_{60} and enhance its colloidal stability in water.[11, 12] On the other hand, the effect of surface-immobilized macromolecules (e.g., humic acid in organic-rich soil/sediment) on nC_{60}

deposition has been found to vary. Humic acid and alginate were found to retard nC_{60} deposition through steric repulsion;[2] while EPS enhanced the deposition of nC_{60}.[9]

In this chapter, deposition of nC_{60} under environmentally relevant conditions was investigated by introducing UVA irradiation and humic acid, in either dissolved or surface-immobilized form, into the experimental system. The main objective was to determine the role of nC_{60} surface transformation (surface oxidation under sunlight and addition of humic acid) in its deposition behavior. nC_{60} irradiated by UVA for varying periods of time was thoroughly characterized, and its deposition kinetics on bare and humic acid coated silica surface measured under different solution conditions was compared to that of pristine nC_{60}. nC_{60} deposition kinetics was directly measured by QCM-D and compared to that determined by conventional packed column experiments. This is the first study addressing the effect of solar irradiation on nC_{60} deposition. Along with my earlier work regarding the impact of sunlight and humic acid on nC_{60} aggregation,[12] findings from this study underscore the important role of solar irradiation in the environmental fate and transport of nC_{60}, suggesting that a better quantitative understanding of environment-induced changes in nC_{60} surface chemistry is crucial to predicting its environmental transport and fate.

5.2 Materials and Methods

5.2.1 Materials. Sublimed C_{60} powder (> 99%) was purchased from Materials Electronics Research Corporation (Tucson, AZ). Suwannee River humic acid standard (II) (SRHA) and Elliott Soil humic acid (EHA) were purchased from the International Humic Substances Society (Atlanta, GA). Humic acid stock solutions were prepared by stirring

the HA solutions in dark for 24 hours followed by filtration through 0.45-μm pore-size nylon membrane filters (Whatman, Piscataway, NJ). The concentrations of HA stock solutions were determined using a high-sensitivity TOC analyzer (Shimadzu Scientific Instruments, Columbia, MD) based on the carbon content of SRHA (52.6%) and EHA (58.1%).[13] Poly-L-lysine (PLL, P-1274), reagent-grade NaCl and two types of pure silica sands, with particle size 0.5 ~ 10 μm (silica sand 1) and 5 ~ 15 nm (silica sand 2) were obtained from Sigma-Aldrich (St. Louis, MO). 4-(2-Hydroxyethyl)-1-Piperazineethanesulfonic Acid (HEPES) was purchased from Fisher Scientific (Pittsburgh, PA). All solutions were prepared with ultrapure water generated by an E-pure system (Barnstead, Dubuque, IA).

5.2.2 Preparation of nC_{60} Stock Suspension. The aqueous nC_{60} stock suspension was prepared using a direct sonication protocol. A total of 150 mg pulverized C_{60} powder was mixed with 200 mL deionized water in a 500-mL glass beaker, and sonicated at 100 W with a sonicating probe (Vibra-Cell VCX 500, Sonics & Material, Newtown, CT) for 30 min in an ice bath. The resulting mixture was filtered through 2-μm pore-size Millex-AP membrane filters (Millipore, Billerica, MA) to remove large particles. All filters were washed with 10 mL of ultrapure water before use and replaced after 30 mL of filtrate was collected. The concentration of the resulting C_{60} suspension was 11 mg/L as measured by TOC. It was diluted to 10 mg/L and stored in dark at room temperature. The intensity based mean hydrodynamic diameter of nC_{60} was determined by DLS (Zen 3600 zetasizer Nano, Malvern, Worcestershire, UK) to be 162 ± 5 nm. All experiments were performed within 5 months, during which the stock suspension was stable as confirmed by monitoring the particle size distribution.

5.2.3 UVA Irradiation Experiments. Since UVA is the main component of UV light in solar spectrum, a light source in UVA wavelength was used to simulate the UV portion in solar irradiation. In the irradiation experiments, aliquots of 30 mL nC_{60} stock suspension were added to 50 mL Erlenmeyer flasks and sealed with parafilm with vents. In each experiment, four flasks were placed on the merry-go-round at the center of a Luzchem LZC-4 V photoreactor (Luzchem, Ottawa, Ontario, Canada). Four 8 W black lamps (Hitachi FL8BL-B, $\lambda = 350 \pm 50$ nm), two on each side, provided a total irradiation intensity of 2 mW/cm^2 in the middle of the reactor as measured by a radiometer at 350 nm (Control Company, Firendwoods, TX). Ambient air was circulated through the photoreactor, and the temperature was maintained at 25 ± 3 °C. Samples were withdrawn on the 20th hour and 7th day and stored in dark at room temperature before analysis. The surface oxygen content of nC_{60} with different irradiation time was determined by XPS (PHI Quanteria, Chanhassen, MN). To prepare samples for XPS analysis, 50 mL sample suspension was filtered through a 0.1-μm membrane filter (Millipore, Billerica, MA) to collect nC_{60} on the membrane surface. The solid cake was dried in a vacuum oven at -85 kPa and 100 **°C** for two days.

5.2.4 nC_{60} Aggregation Kinetics and Electrophoretic Mobility. Particle size determines the diffusive mass transfer rate of colloidal particles to a surface and hence the deposition rate. nC_{60} particle size during the deposition measurement was determined from aggregation kinetics measurements in the same solution chemistry. The electrophoretic mobility of nC_{60} and silica sands was measured in folded capillary cells (Malvern, Worcestershire, UK) by PALS at 25 °C with at least 5 measurements per sample.

5.2.5 Deposition Kinetics of nC_{60}. The deposition kinetics of nC_{60} on bare and humic acid (SRHA or EHA) coated silica surface was first studied using a QCM-D system (Q-Sense E4, BiolinScientific, Västra Frölunda, Sweden). The system is equipped with four measurement chambers each housing a 5 MHz silica coated quartz crystal sensor (Batch 10384, Biolin Scientific, Västra Frölunda, Sweden). Before use, the silica coated crystals were soaked in 2% SDS cleaning solution for 12 h and sonicated for 20 min. They were then copiously rinsed with ultrapure water, dried with ultra high-purity N_2 and cleaned in an ozone/UV chamber (Bioforce Nanoscience, Inc., Ames, IA) for 30 min immediately prior to use. All the measurements were performed at a constant temperature of 25 °C and a flow rate of 0.1 mL/min, resulting in a laminar flow in the measurement chamber with a Reynolds number (*Re*) of 0.2. In each experiment, the electrolyte solution was first pumped through the measurement chamber until a stable baseline is achieved (i.e., the frequency signal drifts less than 1.8 Hz/h). For experiments involving dissolved humic acid, the background solution containing the electrolyte and humic acid was then introduced into the system for 20 min. Except for EHA in 100 mM NaCl, there was no humic acid adsorption on the silica surface at ionic strength up to 100 mM as reflected by the unchanged frequency. Predetermined amount of NaCl, humic acid and nC_{60} stock solutions were mixed to form test solutions with 5 mg/L nC_{60} in the solution chemistry of interest and an unadjusted pH of 6.0 ± 0.5. The resulting suspension was immediately pumped into the measurement chamber, allowing nC_{60} to deposit on the silica coated crystal surface. As the deposition took place, the increasing mass of nC_{60} on the silica crystal surface hindered the vibration of the crystal and subsequently reduced

the frequency. A viscoelastic deposited layer also dampened the sensor vibration, leading to energy dissipation.

The mass of a thin and rigid deposited layer on the silica crystal surface is related to the change of the frequency as described by the Sauerbrey Equation:[14, 15]

$$\Delta m = -\frac{C\Delta f_n}{n} \quad (5\text{-}1)$$

Here, Δm is the deposited mass, Δf_n is the change of frequency at overtone *n*, and *C* is the crystal constant (17.7 ng/(Hz-cm^2)).

For a viscoelastic layer, the Voigt model is usually used to obtain the thickness or mass and viscoelastic properties of the layer.[15] In our study, significant dissipation accompanied frequency decrease during nC_{60} deposition, suggesting a viscoelastic nC_{60} layer. Both the frequency and the dissipation changed linearly with time during the initial deposition of nC_{60}, indicating continuous deposition on the clean crystal surface (i.e., no ripening or detachment). The Voigt model was employed to simultaneously fit the frequency and dissipation data at the 3rd, 5th, 7th, 9th and 11th overtone to obtain nC_{60} deposition rate in terms of mass per unit time. The model calculated mass deposition rate correlated well with the initial slope of the frequency data. Considering the limitations of the mass deposition rate calculation, e.g., it assumes a homogeneous, uniform layer, and the mass calculated includes that of water in the layer, we chose to quantify nC_{60} deposition rate using the initial (200 sec) slope of the frequency shift obtained at the 3rd overtone Δf_3, which is the most stable. In order to gain insight on the physicochemical

interactions between nC_{60} and the surface, nC_{60} deposition rates were normalized by that measured under favorable deposition conditions to obtain the attachment efficiency α:

$$\alpha = \frac{d\Delta f_3/dt}{(d\Delta f_3/dt)_{fav}} \quad (5\text{-}2)$$

Here $d\Delta f_3/dt$ and $(d\Delta f_3/dt)_{fav}$ are the initial slope of frequency shift measured at the 3rd overtone in the solution of interest and that under favorable deposition conditions, respectively. In this study, the favorable deposition conditions were achieved by coating the silica crystal sensor with positively charged PLL.

Deposition of pristine nC_{60} on bare sand was also examined using conventional packed column experiments to compare with the QCM-D results.

5.2.6 Precoating Silica Surface with PLL and Humic Acid. To coat the silica crystal surface with PLL, bare silica surface was first rinsed with a HEPES solution (10 mM HEPES, 100 mM NaCl). Then the PLL coating solution (100 mg/L PLL, 10 mM HEPES, 100 mM NaCl) was introduced for 15 min, during which PLL adsorption reached equilibrium as suggested by the stabilized frequency. To study the deposition of nC_{60} on humic acid coated silica surface, a layer of humic acid was adsorbed on the PLL layer by flowing 10 mM NaCl, followed by 10 mg/L humic acid in 10 mM NaCl for 40 min across the crystal surface. Finally, the PLL or humic acid coated surface was rinsed with the electrolyte solution used in the deposition measurement. Silica sand was used as a surrogate for the silica crystals to dertermine their surface potential. Humic acid coated silica sand was made by successively dispersing the sand in 100 mg/L PLL and 10 mg/L

EHA solutions. The sand was separated from each solution by centrifugation (1000 g for 5 min) and thoroughly washed with ultrapure water.

5.3 Results and Discussion

5.3.1 nC_{60} Deposition under Favorable Conditions. The favorable deposition rate of nC_{60} as a function of NaCl concentration is presented in Figure 5.1. For each type of nC_{60}, the favorable deposition rate was constant at low ionic strength, but decreased sharply as ionic strength increased. According to the aggregation data, when the nC_{60} suspension entered the QCM-D measurement chamber (5 min after the nC_{60} stock suspension was mixed with the NaCl solution), nC_{60} nanoparticles were stable at low ionic strength (up to 10 and 150 mM for the pristine nC_{60} and the 7-day UVA-irradiated nC_{60} (7DUV nC_{60}), respectively), but aggregated at higher ionic strength. Peclet number (P_e), which represents the ratio of convective to diffusive mass transport, ranged from 5.9×10^{-7} to 5.0×10^{-5} in these deposition experiments, suggesting diffusive mass transport. Therefore, the sharp decline of favorable deposition rate at higher ionic strength was attributed to the increase of particle size due to aggregation and the consequent decrease in diffusion coefficient as suggested by the Stokes-Einstein equation. Because the UVA irradiation didn't change the initial particle size,[12] the favorable deposition rates of all three nC_{60} were identical at low ionic strength that did not cause significant aggregation. The favorable deposition rate reached a plateau beyond a certain NaCl concentration. We hypothesize it is caused by the diffusion-limited nC_{60} aggregation at NaCl concentrations beyond the CCC, where the aggregation rate is independent of NaCl concentration.

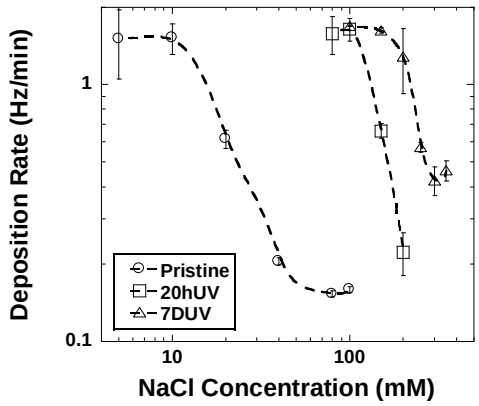

Figure 5.1. Deposition rates of pristine, 20-hour UVA-irradiated (20hUV) and 7-day UVA-irradiated (7DUV) nC_{60} to PLL-coated silica crystal surface (favorable deposition condition) as a function of NaCl concentration. Error bars represent standard deviation.

5.3.2 The Effect of UVA Irradiation. Figure 5.2 compares the deposition rate and attachment efficiency of pristine and UVA-irradiated nC_{60}. Previous studies suggest the stability of pristine nC_{60} heavily depends on the synthesis protocol and resulting nanoparticle properties, especially particle size and surface charge.[16-18] Nevertheless, deposition of pristine nC_{60} is generally susceptible to changes in ionic strength, with a critical deposition concentration of 18 mM NaCl (Figure 5.2a) in this work, lower than that previously reported for nC_{60} prepared by solvent exchange, 30 and 32 mM NaCl.[2, 19] The deposition rate of each nC_{60} was found to decrease at high ionic strength due to the decline of mass transfer rate caused by concurrent aggregation of the nanoparticles (Figure 5.2b).

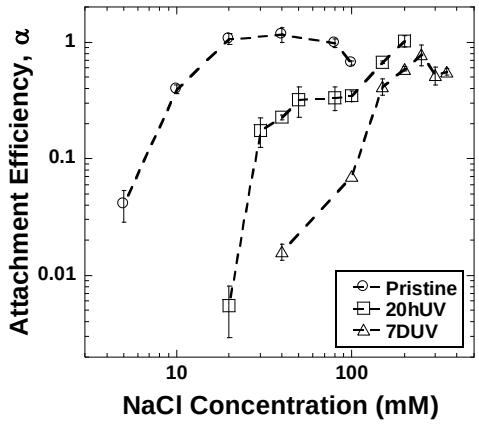

Figure 5.2a. Attachment efficiencies of pristine, 20-hour UVA-irradiated (20hUV) and 7-day UVA-irradiated (7DUV) nC_{60} on silica surface as a function of NaCl concentration. Error bars represent standard deviation.

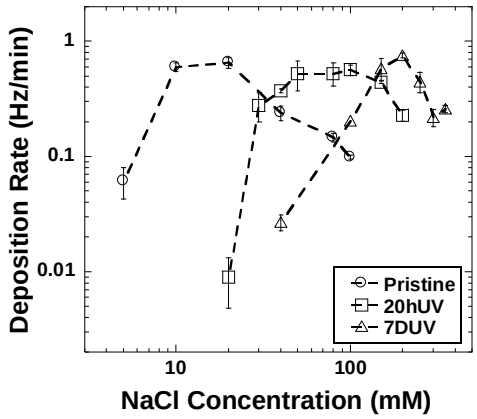

Figure 5.2b. Deposition rates of pristine, 20-hour UVA-irradiated (20hUV) and 7-day UVA-irradiated (7DUV) nC_{60} on silica surface as a function of NaCl concentration. Error bars represent standard deviation.

Figure 5.2a clearly shows that UVA irradiation remarkably enhanced the stability of nC_{60} against deposition, consistent with our previous finding showing that UVA irradiation enhanced the stability of nC_{60} against aggregation in NaCl solutions.[12] The

increased stability was mainly attributed to the surface oxidation and the resulting increase in negative surface potential and hydrophilicity. XPS analysis revealed a notable increase of mono-oxygenated carbon (C-O) and di-oxygenated carbon (C=O or O-C-O) on UVA-irradiated nC_{60} surface, suggesting the introduction of oxygen-containing functional groups. The surface oxygen content of nC_{60} increased with increasing UVA irradiation time from 9.3 ± 0.3 % at the pristine state to 11.3 ± 0.6 % after 20 hours and 14.2 ± 0.6 % after 7 days of irradiation (Figure 5.3a). As a result, the negative surface charge increased with increasing irradiation time as indicated by the measured electrophoretic mobility (Figure 5.3b), consistent with their higher stability shown in Figure 5.2a. The 7DUV nC_{60} was also more negatively charged than previously reported,[12] suggesting batch to batch variations of the irradiated samples. The stability of nC_{60} exhibits a systematic dependence on its surface oxygen content; sample with higher surface oxygen content tends to be more stable. Similar relationship has been reported between the colloidal stability of multi-walled carbon nanotubes and its surface oxygen concentration.[20, 21]

In Figure 5.2a, the attachment efficiency α of the 7DUV nC_{60} reached a maximum at 250 mM NaCl, yet its value, 0.78 ± 0.15, was notably smaller than 1. This was followed by a decrease in α (0.52 ± 0.09) when NaCl concentration further increased to 300 mM. Calculation of DLVO interaction energy between the 7DUV nC_{60} and the bare silica surface, however, shows that the energy barrier disappears at 250 mM NaCl. Such discrepancy suggests that the surface oxygen functional groups can stabilize nC_{60} through non-DLVO forces. Lower than unity α values were also observed with UVA-irradiated nC_{60} in our previous study on nC_{60} aggregation.[12] The decrease in attachment efficiency

at high ionic strength has been reported in the deposition of bacteriophage MS2, norovirus GI and GII and polystyrene latex colloids on silica and glass surfaces.[22-24] These results cannot be explained by the DLVO theory[25, 26] and were attributed to structural forces, likely the hydration force. Hydration force also seems to affect the deposition behavior of the pristine and 20-hour UVA-irradiated (20hUV) nC_{60}. The attachment efficiency of both was lower than expected at NaCl concentration between 80 and 100 mM. However, hydration force was less significant for the pristine and 20hUV nC_{60} than the 7DUV nC_{60} because (1) UVA irradiation increased the surface hydrophilicity of nC_{60} and consequently enhanced the hydration force; (2) hydration force is more pronounced at high ionic strength, where the surface hydrated counter ions are more abundant.

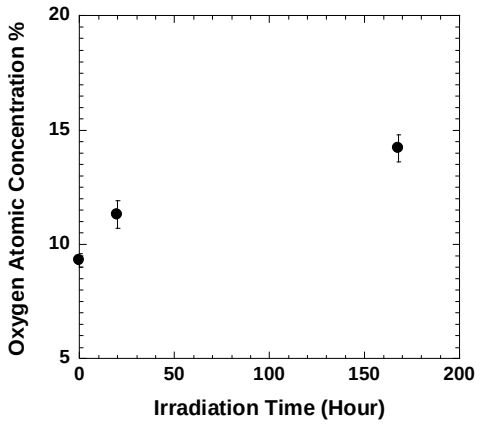

Figure 5.3a. Surface oxygen atomic concentration of nC_{60} as a function of UVA irradiation time as measured by XPS. Error bars represent standard deviation.

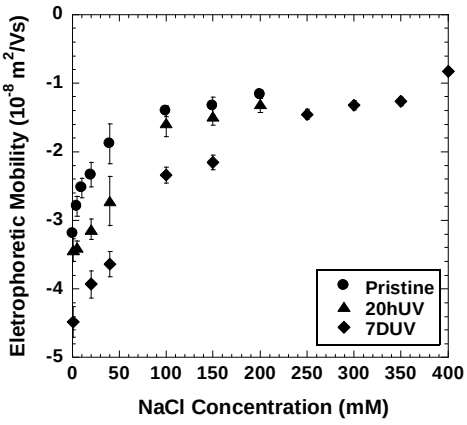

Figure 5.3b. Electrophoretic mobility of pristine, 20-hour UVA-irradiated (20hUV) and 7-day UVA-irradiated (7DUV) nC_{60} as a function of NaCl concentration. Error bars represent standard deviation.

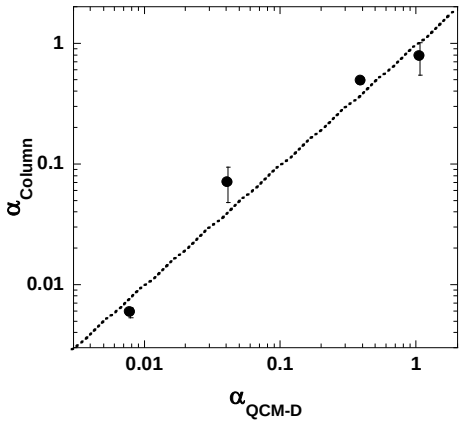

Figure 5.4. Correlation between attachment efficiencies of pristine nC_{60} deposition in the packed column system and QCM-D system at the same ionic strength. Error bars represent standard deviation. Dashed line indicates the perfect consistency.

Deposition kinetics of pristine nC_{60} was also characterized by packed column experiments. The seepage velocity was adjusted to match the flow velocity used in the QCM-D measurements (2×10^{-4} m/s). The *Pe* in the packed column and QCM-D systems

are 9.6×10^{-6} and 5.9×10^{-7} respectively over the ionic strength range compared, suggesting diffusive transport in both systems. The calculated α values are compared to those determined by QCM-D in Figure 5.4. The attachment efficiency determined from the two systems, α_{Column} and α_{QCM-D}, agree with each other well, suggesting the relevance and applicability of QCM-D as an alternative for packed column experiments to study nC_{60} deposition behavior. The QCM-D method is less time consuming and labor intensive; it also avoids heterogeneity in porous media grain size, porosity and surface chemistry, which contribute to discrepancies between different works.

5.3.3 The Effect of Dissolved Humic Acid. As a major component of NOM, humic acid can readily adsorb onto colloidal particles via hydrophobic interactions, alter their surface physicochemical properties and consequently change their transport pattern. Various studies have reported that dissolved humic acid could retard deposition of various colloidal particles such as nC_{60}, latex particles, carbon nanotubes, hematite, and titanium dioxide,[2, 27-31] mainly through the steric hindrance effect. Our previous study revealed that humic acid adsorbed on nC_{60} significantly enhanced the stability of nC_{60} against aggregation; with 1 mg/L SRHA, the CCC of the pristine nC_{60} rose from 84 mM to 331 mM NaCl,[12] and there was no detectable change in particle size at 100 mM NaCl (the highest ionic strength used in deposition experiments with dissolved humic acid) for at least 5 min. Because the nC_{60} used in this work was prepared in the same way as our previous study, the particle size is assumed to remain unchanged in the presence of humic acid (at 1 mg/L and 5 mg/L) over the NaCl concentrations tested (5-100 mM).[12] Thus the favorable deposition rate measured in 5 mM NaCl solution in the absence of humic acid was used for the whole ionic strength range tested.

Adsorption of dissolved humic acid can affect nC_{60} deposition of in two ways: 1) it hinders aggregation and hence enhances diffusive mass transfer; 2) it reduces the deposition attachment efficiency. As shown in Figure 5.5a, the deposition attachment efficiency was reduced by up to one order of magnitude in the presence of humic acid. The reduced deposition can be attributed to the change of nC_{60} surface potential and the steric repulsion from adsorbed humic acid. Adsorption experiments show that EHA and SRHA had similar adsorption on pristine nC_{60} at 1 mg/L (K_d = 1648 and 1722 (mg/Kg)/(mg/L) respectively). However, EHA was more efficient than SRHA in stabilizing pristine nC_{60}, likely due to its higher molecular weight,[13, 32, 33] which results in stronger steric repulsion. In the absence of humic acid, the nC_{60} attachment efficiency increased with increasing ionic strength as predicted by the DLVO theory, except for a drop at very high ionic strength as discussed earlier. In the presence of humic acid, however, the nC_{60} attachment efficiency exhibited a complex, non-monotonous behavior. Such complex behavior is a result of the interplay between the conflicting effects of ionic strength on humic acid adsorption by nC_{60} and nC_{60} surface potential. When ionic strength increases, the electrostatic repulsion between nC_{60} and the silica surface decreases, leading to more deposition; on the other hand, the electrostatic repulsion between humic acid molecules and nC_{60} surface also decreases, resulting in more humic acid adsorption and hence greater steric hindrance effect. The effect of ionic strength on the overall nC_{60} deposition efficiency is therefore the net effect of these two mechanisms. This interpretation is supported by measurement of SRHA adsorption on the pristine nC_{60} coated silica surface using QCM-D. At a SRHA concentration of 5 mg/L, the amount of SRHA adsorbed on nC_{60} coated silica crystal surface was 0.50 mg/m^2 at 10 mM NaCl,

and increased to 0.78 mg/m^2 at 40 mM NaCl. As expected, the nC_{60} attachment efficiency decreased with increasing SRHA concentration due to more SRHA adsorption. The complex behavior of nC_{60} attachment efficiency in the presence of humic acid clearly demonstrates that quantification of NOM adsorption is crucial to accurate prediction of nC_{60} deposition. Both SRHA and EHA had negligible adsorption on the 7DUV nC_{60} surface at 1 mg/L due to increased nC_{60} surface hydrophilicity and negative charge after irradiation. Thus dissolved humic acid is expected to affect the deposition of UVA-irradiated nC_{60} to a much less extent.

The overall impact of dissolved humic acid on nC_{60} deposition is the net effect of enhanced nC_{60} mass transfer to the surface because of the smaller particle size and the reduced attachment efficiency (Figure 5.5b). The nC_{60} deposition rate in the absence of humic acid initially increased with ionic strength due to the increase in attachment efficiency, but declined at ionic strength greater than 20 mM due to nC_{60} aggregation and hence decreased mass transfer. Dissolved humic acid reduced nC_{60} deposition at low ionic strength, suggesting that the reduction in attachment efficiency due to steric hindrance out-competes the enhanced mass transfer rate resulting from smaller particle sizes. At high ionic strength (e.g., 100 mM NaCl), however, the opposite occurred: nC_{60} deposition rate in the presence of humic acid was much higher than that in the absence of humic acid, although the attachment efficiency of nC_{60} is lower in the presence of humic acid (Figure 5.5a). This is attributed to the enhanced mass transfer rate of nC_{60} in the presence of humic acid due to the smaller particle size. However, these results should not be simply interpreted as dissolved humic acid would enhance the deposition of nC_{60} at high ionic strength, as nC_{60} would undergo fast aggregation without humic acid and large

nC_{60} aggregates can be easily removed by straining in porous media, which is not reflected by the QCM-D measurement.

5.3.4 The Effect of Surface-immobilized Humic Acid. Using two pure silica sands (silica sand 1 and 2) as surrogates to the silica crystal surface, surface-immobilized humic acid was found to lower the negative surface potential of the silica crystal. As shown in Figure 5.6a, although ζ potential of the two bare silica sands was drastically different, EHA coated silica sands were similarly charged, suggesting that the surface potential of silica sands was dominated by the immobilized EHA macromolecules. The ζ potential of the bare silica crystal surface is -53 mV as measured by a SurPASS Electrokinetic Analyzer in 1 mM ionic strength, which is close to silica sand 1, -52 ± 2.2 mV. Therefore, EHA coated silica crystal surface was assumed to have the same ζ potential as the EHA coated silica sand 1. This finding qualitatively agreed with an earlier study using crushed quartz sand as a surrogate for the silica crystal.[34]

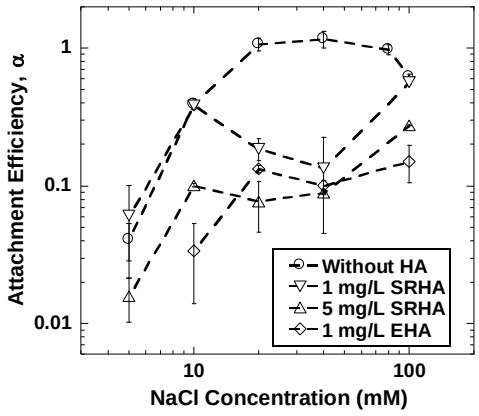

Figure 5.5a. Attachment efficiencies of pristine nC_{60} onto silica surface as a function of NaCl concentration in the presence of dissolve Suwannee River humic acid or Elliott Soil humic acid. Error bars represent standard deviation.

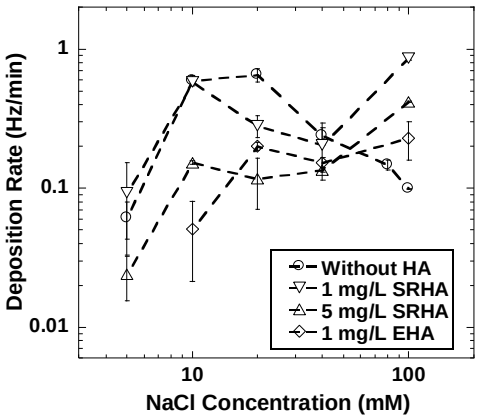

Figure 5.5b. Deposition rates of pristine nC_{60} onto silica surface as a function of NaCl concentration in the presence of dissolve Suwannee River humic acid or Elliott Soil humic acid. Error bars represent standard deviation.

The deposition of pristine nC_{60} on EHA coated silica surface was lower than that on bare silica surface (Figure 5.6b), whereas the deposition of pristine nC_{60} on SRHA coated silica surface was similar to that on the bare silica surface except at 5 mM. This contradicts the DLVO calculation which shows notably lower energy barrier on EHA coated silica surface. The reduced deposition is attributed to steric hindrance by the immobilized humic acid. This effect is more pronounced at low ionic strength because humic acid molecules have a more stretched-out conformation due to the electrostatic repulsion between charged groups.

The presence of both surface-immobilized EHA and SRHA greatly facilitated the deposition of 7DUV nC_{60} and the attachment efficiency on the humic acid coated surface was less sensitive to the change of ionic strength as shown in Figure 5.6c. Several studies

have reported enhanced colloid deposition by surface-immobilized macromolecules, including nC_{60} deposition on alginate[2] and EPS coated silica surface,[9] and *pseudomonas aeruginosa* deposition on alginate coated silica surface[35] in monovalent electrolyte solutions, which was attributed to the hydrophobic effect or physical trapping in the macromolecules. However, neither of the mechanisms applied in this case. The 7DUV nC_{60} is more hydrophilic than the pristine nC_{60} as a result of surface oxidation; physical trapping, if any, is expected to also enhance the deposition of the pristine nC_{60}, contradictory to our findings. Moreover, the effect of physical trapping will be largely suppressed at high ionic strength as the structure of humic acid becomes more compact. We hypothesize that three mechanisms are responsible for the enhanced attachment efficiency of the 7DUV nC_{60} on humic acid coated silica surfaces: the diminished steric hindrance, the reduced collector surface potential, and hydrogen bonding. It has been shown that the structure and properties of immobilized macromolecules strongly depend on ionic strength.[22, 36] At high ionic strength (~60 mM), the steric hindrance diminishes as the conformation of humic acid become more compact.[22, 35] Thus at the ionic strength we employed for measuring the 7DUV nC_{60} deposition kinetics, 40 ~ 200 mM, the steric hindrance force was likely not prominent. DLVO calculation suggests the presence of surface immobilized humic acid reduces electrostatic repulsion, which partially offsets the effect of steric hindrance forces and gradually became the dominant effect with increasing ionic strength. This is consistent with our observation of both pristine and 7DUV nC_{60} deposition.

However, the deposition of the 7DUV nC_{60} on humic acid coated silica surfaces is relatively insensitive to ionic strength, suggesting the reduced electrostatic repulsion is

not the sole mechanism for the enhanced deposition. Another likely mechanism involved is hydrogen bonding between the oxygen-containing groups on the 7DUV nC_{60} surface and the oxygen and nitrogen-containing groups on surface-immobilized humic acid.

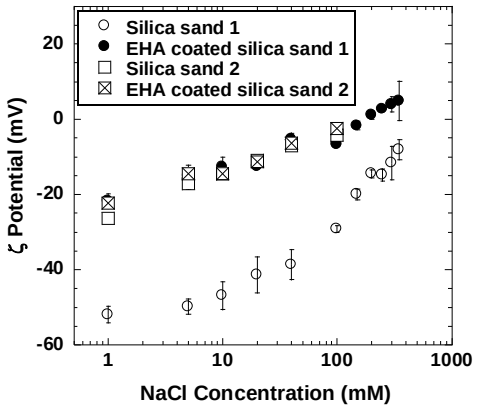

Figure 5.6a. ζ potentials of bare and Elliot Soil humic acid coated silica sand as a function of NaCl concentration. Error bars represent standard deviation. The particle size of silica sand 1 and 2 are 0.5 ~ 10 um and 5 ~ 15 nm respectively.

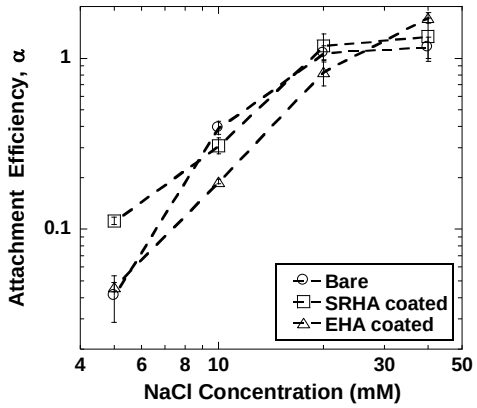

Figure 5.6b. Attachment efficiencies of pristine nC_{60} onto bare and humic acid coated silica surface as a function of NaCl concentration. Error bars represent standard deviation.

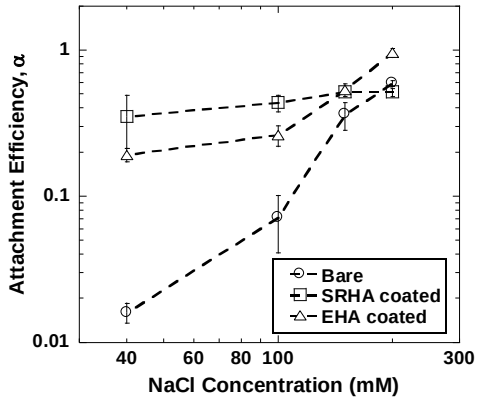

Figure 5.6c. Attachment efficiencies of 7-day UVA-irradiated nC_{60} onto bare and humic acid coated silica surface as a function of NaCl concentration. Error bars represent standard deviation.

5.4 Conclusion

Nanoparticle transport in natural settings is complex due to interactions with the surrounding environment. In this study, the impact of UVA irradiation and humic acid on deposition of nC_{60} on silica surface as a surrogate for natural sediments was studied using packed column experiments and quartz crystal microbalance with dissipation monitoring under various solution conditions. Surface oxidation of nC_{60} induced by UVA irradiation greatly retarded its deposition due to the increased negative surface charge and hydrophilicity. Dissolved humic acid, once adsorbed onto nC_{60} surface, also hindered its deposition mainly through steric hindrance forces. The extent of this effect depended on the properties and amount of humic acid adsorbed, which is a function of ionic strength and humic acid concentration. humic acid has limited adsorption on UVA-irradiated nC_{60} and is expected to play a less important role in its stability. Humic acid immobilized onto the silica surface had a variable effect on nC_{60} deposition, depending on the complex

interplay of DLVO and non-DLVO interactions such as electrostatic interaction, steric hindrance, and hydrogen bonding as well as humic acid molecular conformation. These results highlight the importance of environment-induced changes in nC_{60} surface chemistry in its fate and transport in aquatic environments.

Part of this chapter has been published and reprinted with permission from: Qu, X.L., Alvarez, P.J.J., Li, Q.L. Impact of Sunlight and Humic Acid on the Deposition Kinetics of Aqueous Fullerene Nanoparticles (nC_{60}). ***Environmental Science & Technology*** 46(24), 13455-13462. **2012**.

5.5 References

(1) Brant, J.; Lecoanet, H.; Wiesner, M. R., Aggregation and deposition characteristics of fullerene nanoparticles in aqueous systems. *J. Nanopart. Res.* **2005,** *7*, (4-5), 545-553.

(2) Chen, K. L.; Elimelech, M., Interaction of Fullerene (C-60) Nanoparticles with Humic Acid and Alginate Coated Silica Surfaces: Measurements, Mechanisms, and Environmental Implications. *Environ. Sci. Technol.* **2008,** *42*, (20), 7607-7614.

(3) Espinasse, B.; Hotze, E. M.; Wiesner, M. R., Transport and retention of colloidal aggregates of C-60 in porous media: Effects of organic macromolecules, ionic composition, and preparation method. *Environ. Sci. Technol.* **2007,** *41*, (21), 7396-7402.

(4) Wang, Y. G.; Li, Y. S.; Fortner, J. D.; Hughes, J. B.; Abriola, L. M.; Pennell, K. D., Transport and retention of nanoscale C-60 aggregates in water-saturated porous media. *Environ. Sci. Technol.* **2008,** *42*, (10), 3588-3594.

(5) Wang, Y. G.; Li, Y. S.; Pennell, K. D., Influence of electrolyte species and concentration on the aggregation and transport of fullerene nanoparticles in quartz sands. *Environmental Toxicology and Chemistry* **2008,** *27*, (9), 1860-1867.

(6) Wang, Y. G.; Li, Y. S.; Kim, H.; Walker, S. L.; Abriola, L. M.; Pennell, K. D., Transport and Retention of Fullerene Nanoparticles in Natural Soils. *J. Environ. Qual.* **2010,** *39*, (6), 1925-1933.

(7) Li, Y. S.; Wang, Y. G.; Pennell, K. D.; Abriola, L. M., Investigation of the transport and deposition of fullerene (C60) nanoparticles in quartz sands under varying flow conditions. *Environ. Sci. Technol.* **2008,** *42*, (19), 7174-7180.

(8) Isaacson, C.; Zhang, W.; Powell, T.; Ma, X.; Bouchard, D., Temporal Changes in Aqu/C-60 Physical-Chemical, Deposition, and Transport Characteristics in Aqueous Systems. *Environ. Sci. Technol.* **2011,** *45*, (12), 5170-5177.

(9) Tong, M. P.; Ding, J. L.; Shen, Y.; Zhu, P. T., Influence of biofilm on the transport of fullerene (C-60) nanoparticles in porous media. *Water Res.* **2010,** *44*, (4), 1094-1103.

(10) Chae, S. R.; Xiao, Y.; Lin, S.; Noeiaghaei, T.; Kim, J. O.; Wiesner, M. R., Effects of humic acid and electrolytes on photocatalytic reactivity and transport of carbon nanoparticle aggregates in water. *Water Res.* **2012**.

(11) Chen, K. L.; Elimelech, M., Influence of humic acid on the aggregation kinetics of fullerene (C-60) nanoparticles in monovalent and divalent electrolyte solutions. *J. Colloid Interface Sci.* **2007,** *309*, (1), 126-134.

(12) Qu, X. L.; Hwang, Y. S.; Alvarez, P. J. J.; Bouchard, D.; Li, Q. L., UV Irradiation and Humic Acid Mediate Aggregation of Aqueous Fullerene (nC(60)) Nanoparticles. *Environ. Sci. Technol.* **2010,** *44*, (20), 7821-7826.

(13) IHSS Website. http://www.ihss.gatech.edu/

(14) Sauerbrey, G., Verwendung Von Schwingquarzen Zur Wagung Dunner Schichten Und Zur Mikrowagung. *Zeitschrift Fur Physik* **1959,** *155*, (2), 206-222.

(15) Reviakine, I.; Johannsmann, D.; Richter, R. P., Hearing What You Cannot See and Visualizing What You Hear: Interpreting Quartz Crystal Microbalance Data from Solvated Interfaces. *Anal. Chem.* **2011,** *83*, (23), 8838-8848.

(16) Chen, K. L.; Elimelech, M., Interaction of Fullerene (C(60)) Nanoparticles with Humic Acid and Alginate Coated Silica Surfaces: Measurements, Mechanisms, and Environmental Implications. *Environ. Sci. Technol.* **2008,** *42*, (20), 7607-7614.

(17) Isaacson, C.; Zhang, W.; Powell, T.; Ma, X.; Bouchard, D., Temporal Changes in Aqu/C(60) Physical-Chemical, Deposition, and Transport Characteristics in Aqueous Systems. *Environ. Sci. Technol.* **2011,** *45*, (12), 5170-5177.

(18) Chen, K. L.; Elimelech, M., Relating Colloidal Stability of Fullerene (C-60) Nanoparticles to Nanoparticle Charge and Electrokinetic Properties. *Environ. Sci. Technol.* **2009,** *43*, (19), 7270-7276.

(19) Chen, K. L.; Elimelech, M., Aggregation and deposition kinetics of fullerene (C-60) nanoparticles. *Langmuir* **2006,** *22*, (26), 10994-11001.

(20) Smith, B.; Wepasnick, K.; Schrote, K. E.; Bertele, A. H.; Ball, W. P.; O'Melia, C.; Fairbrother, D. H., Colloidal Properties of Aqueous Suspensions of Acid-Treated, Multi-Walled Carbon Nanotubes. *Environ. Sci. Technol.* **2009,** *43*, (3), 819-825.

(21) Smith, B.; Wepasnick, K.; Schrote, K. E.; Cho, H. H.; Ball, W. P.; Fairbrother, D. H., Influence of Surface Oxides on the Colloidal Stability of Multi-Walled Carbon Nanotubes: A Structure-Property Relationship. *Langmuir* **2009,** *25*, (17), 9767-9776.

(22) Yuan, B. L.; Pham, M.; Nguyen, T. H., Deposition Kinetics of Bacteriophage MS2 on a Silica Surface Coated with Natural Organic Matter in a Radial Stagnation Point Flow Cell. *Environ. Sci. Technol.* **2008,** *42*, (20), 7628-7633.

(23) da Silva, A. K.; Kavanagh, O. V.; Estes, M. K.; Elimelech, M., Adsorption and Aggregation Properties of Norovirus GI and GII Virus-like Particles Demonstrate Differing Responses to Solution Chemistry. *Environ. Sci. Technol. 45*, (2), 520-526.

(24) Elimelech, M., Indirect Evidence for Hydration Forces in the Deposition of Polystyrene Latex Colloids on Glass Surfaces. *J. Chem. Soc.-Faraday Trans.* **1990,** *86*, (9), 1623-1624.

(25) Verwey, E. J. W., Theory of the Stability of Lyophobic Colloids. *Philips Research Reports* **1945,** *1*, (1), 33-49.

(26) Derjaguin, B.; Landau, L., Theory of stability of highly charged liophobic sols and adhesion of highly charged particles in solutions of electrolytes. *Zhurnal Eksperimentalnoi Teor. Fiz.* **1945,** *15*, (11), 663-682.

(27) Franchi, A.; O'Melia, C. R., Effects of natural organic matter and solution chemistry on the deposition and reentrainment of colloids in porous media. *Environ. Sci. Technol.* **2003,** *37*, (6), 1122-1129.

(28) Pelley, A. J.; Tufenkji, N., Effect of particle size and natural organic matter on the migration of nano- and microscale latex particles in saturated porous media. *J. Colloid Interface Sci.* **2008,** *321*, (1), 74-83.

(29) Phenrat, T.; Song, J. E.; Cisneros, C. M.; Schoenfelder, D. P.; Tilton, R. D.; Lowry, G. V., Estimating Attachment of Nano- and Submicrometer-particles Coated with Organic Macromolecules in Porous Media: Development of an Empirical Model. *Environ. Sci. Technol.* **2010,** *44*, (12), 4531-4538.

(30) Thio, B. J. R.; Zhou, D. X.; Keller, A. A., Influence of natural organic matter on the aggregation and deposition of titanium dioxide nanoparticles. *J. Hazard. Mater.* **2011,** *189*, (1-2), 556-563.

(31) Jaisi, D. P.; Saleh, N. B.; Blake, R. E.; Elimelech, M., Transport of Single-Walled Carbon Nanotubes in Porous Media: Filtration Mechanisms and Reversibility. *Environ. Sci. Technol.* **2008,** *42*, (22), 8317-8323.

(32) Beckett, R.; Jue, Z.; Giddings, J. C., Determination of Molecular-weight Distributions of Fulvic and Humic Acids Using Flow Field-flow Fractionation. *Environ. Sci. Technol.* **1987,** *21*, (3), 289-295.

(33) Shinozuka, T.; Shibata, M.; Yamaguchi, T., Molecular Weight Characterization of Humic Substances by MALDI-TOF-MS. *J. Mass Spectrom. Soc. Jpn.* **2004,** *52*, (1), 29-32.

(34) Jiang, X. J.; Tong, M. P.; Li, H. Y.; Yang, K., Deposition kinetics of zinc oxide nanoparticles on natural organic matter coated silica surfaces. *J. Colloid Interface Sci. 350*, (2), 427-434.

(35) de Kerchove, A. J.; Elimelech, M., Impact of alginate conditioning film on deposition kinetics of motile and nonmotile Pseudomonas aeruginosa strains. *Appl. Environ. Microbiol.* **2007,** *73*, (16), 5227-5234.

(36) Hong, S. K.; Elimelech, M., Chemical and physical aspects of natural organic matter (NOM) fouling of nanofiltration membranes. *Journal of Membrane Science* **1997,** *132*, (2), 159-181.

Chapter 6: Impact of Photochemical Transformation on the Toxicity of Multi-walled Carbon Nanotubes

6.1 Introduction

The toxicity of CNTs was closely related to their physicochemical properties. Recent studies suggested that CNTs are toxic to organisms at different levels and their toxicity is influenced by several major factors such as impurities, amorphous carbon, surface charge, shape, length, aggregation state, and layer numbers [1]. However, the toxicity mechanism is still not well understood. Early investigation revealed the physical membrane perturbation was one of the major toxicity mechanisms [2-4]. As a result, direct contact between CNT and bacteria is required for inactivation. Later on, the oxidative stress was identified as another toxicity mechanism as suggested by the high level of oxidative stress-related gene expression [3]. However, another study reported that the antimicrobial activity of CNTs did not correlate well with the oxidative stress [4]. Studies have shown that the physicochemical properties of CNT have great influence on its cytotoxicity [3-6]. SWCNT exhibit much higher toxicity than MWCNT due to their smaller diameter [3]. For MWCNT, a correlation between bacterial cytotoxicity and physicochemical properties that enhance MWCNT-cell contact opportunities was found [5]. The authors suggested that nanotubes with higher toxicity are uncapped, debundled, short, and dispersed in solution. The effect of length on the CNT toxicity is still controversial. Short MWCNT and SWCNT were reported to possess higher toxicity [4, 5]. However, one study suggested longer SWCNT is more toxic than the shorter one [7]. Metallic SWCNT have higher

toxicity than the semiconducting SWCNT due to the metallic SWCNT-mediated cellular oxidative stress [6].

Based on these toxicity studies, it was recently proposed that the cytotoxicity of CNT can be generally explained by a three-step mechanism: (1) Direct contact between CNT and bacteria; (2) Cell membrane perturbation; and (3) Disruption of a specific microbial process via disturbing/oxidizing a vital cellular structure/component [6]. Another study suggested this mechanism is also applicable to graphene-based materials (i.e., graphite, graphite oxide, graphene oxide and reduced graphene oxide) [8].

Our previous studies (Chapter 3) suggested the CNT structure changes upon reactions with natural environmental components such as sunlight. As the surface chemistry of CNT changes in the natural aquatic systems, their toxicity evolves accordingly. To date, little has been done to address this issue. To bridge this knowledge gap, the impact of sunlight-induced structure changes on MWCNT toxicity was investigated using *E. coli* as a model organism.

6.2 Material and Methods

6.2.1 Preparation of MWCNT Suspensions and Reactions with ·OH

Both the pristine MWCNT and COOH-MWCNT stock suspensions were prepared by direct sonication. 40 mg CNTs was added to 400 mL deionized water in a 500-mL glass beaker. The mixture was placed in an ice bath and sonicated with a sonicating probe (Vibra-Cell VCX 500, Sonics & Material, Newtown, CT) at 100 W for 30 min. For COOH-MWCNT, a stable dispersion was obtained after sonication, while MWCNT,

though evenly dispersed, formed large aggregates in water. The stock solutions were stored in the dark at room temperature until use.

·OH was generated by UV photolysis of H_2O_2. 50 mL 100 mg/L CNTs were mixed with 50 mL 30% H_2O_2 in a 150-mL glass beaker and exposed to 2.0 mW/cm^2 UVA irradiation in the Luzchem LZC-4V Photoreactor using six 8W black-light lamps (350±50 nm). After reacting for a predetermined period of time, the resulting CNT suspension was filtered through 0.1-μm membranes. The CNTs retained on the membrane were thoroughly washed with deionized water twice and resuspended in 50 mL of deionized water.

6.2.2 Cell Preparation

E. coli 8739 were grown in LB (Luria-Bertani) medium at 37 ℃ for 4 h and harvested in the midexponential growth phase. Bacteria suspension was centrifuged at 5000 rpm for 5 min to pellet the cells. Cells were washed with saline solution (0.9% NaCl) twice to remove residual nutrients and resuspended in saline solution. Bacteria suspension was then diluted using saline solution to obtain stock suspension with optical density of 0.1 at 600 nm.

6.2.3 Cell Viability Assay

Two sets of viability assay, the solution assay and the filter assay, were used to examine the toxicity of MWCNTs towards *E. coli* cells. In the solution toxicity assay, *E.coli* was incubated with predetermined amount of CNT for 3 h at room temperature. The loss of viability of *E. coli* cells was determined by plate counting method. The filter toxicity

assay was carried out by filtering *E. coli* cells on a CNT layer deposited on the membrane to ensure direct contact (bioavailability equals 100%). First, 10 mL of 100 ppm CNT suspension was filtered through a 0.1 μm PVDF membrane filter to form a CNT cake layer. Then 4 mL of 4×10^6 CFU/mL *E. coli* suspension was filtered through the CNT coated membranes and a bare a 0.1 μm PVDF membrane (served as a control). After filtration, the membrane coupon was immersed in 16 mL 0.45% NaCl solution and incubated at room temperature for 3 h. After incubation, the membrane coupon was bath sonicated for 5 min, which has little effect on the viability of *E. coli* cells (data not shown). The CNT layer on the membrane was completely resuspended in the solution and transferred into 50 mL centrifuge tube and mixed by vortex. The viability of the bacteria was then quantified by plate counting method.

6.2.4 Thiol Oxidation and Quantification

Oxidative stress is a major cited mechanism for CNMs. In this study, the oxidative capacity of different CNT samples was quantified by their ability to induce lipid preoxidation and oxidize glutathione (GSH), a common antioxidant and redox state mediator. The lipid peroxidation was quantified using commercial lipid peroxidation (malondialdehyde, MDA) assay kit. MDA is the natural byproduct of lipid peroxidation. It reacts with thiobarbituric acid (TBA) to generate the MDA-TBA adduct, which will be later quantified colorimetrically (λ = 532 nm) or fluorometrically (Ex/Em = 532/553 nm). The thiol groups in GSH can be quantified by the Ellman's assay. 500 µL of 100 mg/L CNT and 500 µL 1 mM GSH were mixed in a 24-well plate covered with alumium foil, and then placed on a shaker to incubate for 3 h at room temperature. After incubation, the

suspension was filtered through a 0.2 μm membrane. A 180 μL aliquot of the filtrate was mixed with 940 μL 0.05 M Tris-HCl and 20 μL 100 mM DNTB (Ellman's reagent, 5,5'-dithio-bis-(2-nitrobenzoic acid). The 150 μL of resulting solution was then transferred into 96-well plates. Their absorbance at 412 nm was measured by a microplate spectrophotometer and used to calculate the loss of GSH. 8.8 mM hydrogen peroxide solution was used as a positive control for the assay.

6.3 Results and Discussion

6.3.1 Bacterial Cytotoxicity of CNTs

Both pristine MWCNT and COOH-MWCNT (> 95% purity) were purchased from NanoLab, Inc. (Newton, MA) with the same diameter and length (15 ± 5 nm and 1 ~ 5 μm, respectively). Pristine MWCNTs were synthesized by a chemical vapor deposition method using a predominantly iron catalyst. They were later purified with HCl to remove accessible iron. COOH-MWCNTs were produced by refluxing pristine MWCNTs in a concentrated HNO_3/H_2SO_4 mixture. Our previous study suggested that the photochemical transformation of COOH-MWCNTs under UVA light was mainly mediated by self-generated ·OH. As a result, the MWCNT and COOH-MWCNT was subjected to ·OH oxidation to simulate the impact of sunlight exposure on their structures. After 30 h reaction with ·OH, COOH-MWCNTs lose surface oxygen-containing functional groups, mainly carboxyl groups as shown in Figure 6.1. On the contrary, MWCNTs gained surface oxygen after 65 h reaction with ·OH.

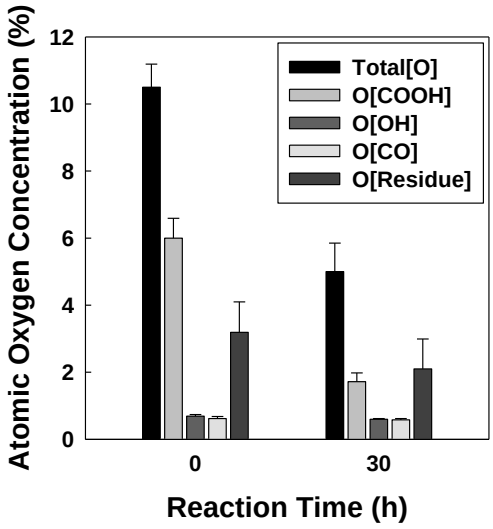

Figure 6.1. Atomic surface oxygen concentration and the distribution of oxygen-containing functional groups on initial and 30h ·OH-treated COOH-MWCNT surfaces. Error bars represent standard deviation.

The cytotoxicity of all four CNT samples including MWCNT, MWCNT after 65 h reaction with ·OH (MWCNT 65h), COOH-MWCNT, and COOH-MWCNT after 30 h reaction with ·OH (COOH-MWCNT 30h) were studied using *E. coli* as a model bacterium. 50 mg/L CNT and 10^6 cells were incubated in 0.45% NaCl solution for 3 h at room temperature. Their antibacterial activities are summarized in Figure 6.2. Interestingly both COOH-MWCNTs and COOH-MWCNTs 30h showed little effect on the cell viability. The cytotoxicity of oxidized MWCNTs have been examined by several groups [5, 9, 10]. However the results in these reports are often contradictory: some studies have reported significant antibacterial activity [5, 10], while others found no toxicity [9]. On the other hand, we found that the MWCNTs and MWCNT 65h exhibited strong antibacterial activity. This also contradicts an earlier study which suggests the ability to

well disperse in water is a key determinant of CNT toxicity [5]. It is well known that one of the most important factors that could lead to the CNT toxicity is impurities such as residual metal catalysts and amorphous carbon. The presence of impurities is also a common reason for conflicting data on CNT toxicity. The metal impurity released from CNTs has been reported to enhance the toxicity [11]. CNTs used in this study have been thoroughly washed by HCl to remove residual ion catalyst. Nevertheless, in order to differentiate the metal-induced toxicity, cell viability assay was conducted in CNT filtrates. As shown in Figure 6.2, the presence of MWCNT filtrate (MWCNT F) has no effect on the cell viability, indicating the minimal role of possible metal impurity in MWCNT sample. MWCNT 65h filtrate (MWCNT 65h F) was able to enhance the growth of *E. coli* cells. It is most likely due to the formation of dissolved organic carbon during the oxidation process, which can be used by cells as carbon sources.

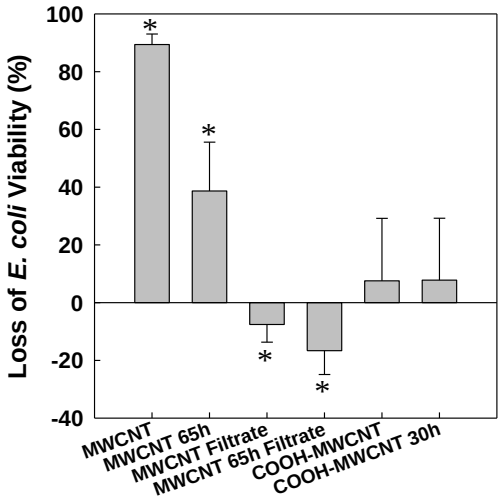

Figure 6.2. Loss of cell viability after incubation with 50 mg/L CNT suspensions and CNT filtrates. *, significant difference between the sample and the control (student *t* test, $P < 0.1$, N=3).

6.3.2 Inhibition of Antibacterial Activity

Oxidative stress is the most commonly accepted mechanism for CNT toxicity. In order to test this mechanism, the antibacterial test was carried out in 1 mM GSH, a common antioxidant. The presence of antioxidant significantly inhibited the loss of cell viability in the presence of both MWCNT and MWCNT 65h as shown in Figure 6.3, suggesting the oxidative stress is a major mechanism of MWCNT antibacterial activity.

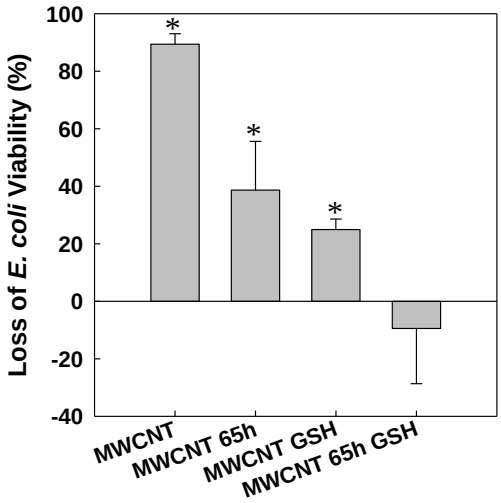

Figure 6.3. Loss of cell viability after incubation with 50 mg/L CNT suspensions with and without 1 mM GSH. *, significant difference between the sample and the control (student *t* test, $P < 0.1$, N=3).

6.3.3 Oxidative Stress Mediated by CNTs

The loss of reduced glutathione in the presence of CNTs was used to quantify their ability to induce oxidation stress. 8.8 mM H_2O_2 was used as a positive control, which oxidized all the glutathione as shown in Figure 7.4. MWCNTs showed strong ability to oxidize glutathione. After 3 h exposure, 90.8 ± 0.2% of the glutathione was oxidized by MWCNT, while COOH-MWCNT only oxidized 27.5 ± 0.7 % of the glutathione. The stronger oxidative capacity of MWCNT correlates well with its higher toxicity (Figure 6.4a), indicating the toxicity of MWCNT is related to its ability to oxidize intracellular components such as thiols. Reactions with ·OH reduced the oxidative capacity of MWCNT as suggested by the lower glutathione oxidation of MWCNT 65h. It is also

consistent with the reduced toxicity of MWCNT after ·OH reaction. The filtrates of MWCNT and MWCNT 65h had little oxidative capacity. ·OH reduced the surface oxygen concentration of COOH-MWCNTs, leading to much stronger oxidative capacity (Figure 6.4b). The loss of glutathione increased from 27.5 ± 0.7 % to 98.5 ± 0.1 % after the COOH-MWCNTs were treated with ·OH for 30 h. Nevertheless, COOH-MWCNT and COOH-MWCNT 30h both had very low toxicity. We hypothesize that the hydrophilic surface of COOH-MWCNTs impeded the contact and penetration of cell membranes, resulting in a lower chance to oxidize intracellular molecules.

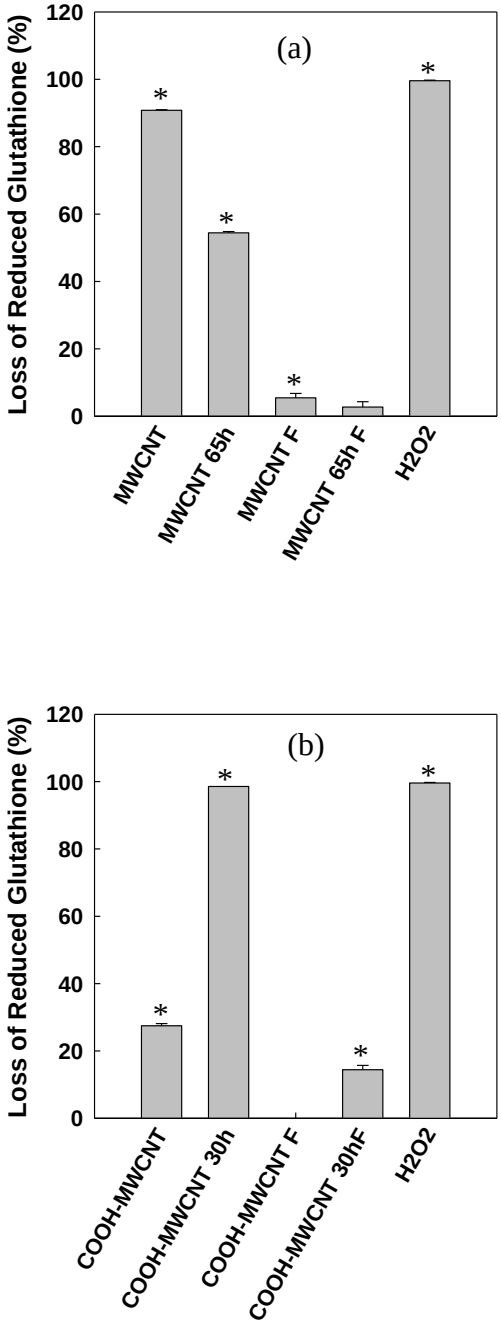

Figure 6.4. *In vitro* loss of reduced glutathione in the presence of 50 mg/L CNTs or 8.8 mM H_2O_2 after 3 h exposure. *, significant difference between the sample and the control (student *t* test, $P < 0.05$, N=3).

6.4 References

(1) Liu, Y.; Zhao, Y.; Sun, B.; Chen, C., Understanding the Toxicity of Carbon Nanotubes. *Accounts of Chemical Research* **2012**.

(2) Kang, S.; Pinault, M.; Pfefferle, L. D.; Elimelech, M., Single-walled carbon nanotubes exhibit strong antimicrobial activity. *Langmuir* **2007,** *23*, (17), 8670-8673.

(3) Kang, S.; Herzberg, M.; Rodrigues, D. F.; Elimelech, M., Antibacterial effects of carbon nanotubes: Size does matter. *Langmuir* **2008,** *24*, (13), 6409-6413.

(4) Liu, S. B.; Wei, L.; Hao, L.; Fang, N.; Chang, M. W.; Xu, R.; Yang, Y. H.; Chen, Y., Sharper and Faster "Nano Darts" Kill More Bacteria: A Study of Antibacterial Activity of Individually Dispersed Pristine Single-Walled Carbon Nanotube. *ACS Nano* **2009,** *3*, (12), 3891-3902.

(5) Kang, S.; Mauter, M. S.; Elimelech, M., Physicochemical determinants of multiwalled carbon nanotube bacterial cytotoxicity. *Environ. Sci. Technol.* **2008,** *42*, (19), 7528-7534.

(6) Vecitis, C. D.; Zodrow, K. R.; Kang, S.; Elimelech, M., Electronic-Structure-Dependent Bacterial Cytotoxicity of Single-Walled Carbon Nanotubes. *ACS Nano* **2010,** *4*, (9), 5471-5479.

(7) Yang, C. N.; Mamouni, J.; Tang, Y. A.; Yang, L. J., Antimicrobial Activity of Single-Walled Carbon Nanotubes: Length Effect. *Langmuir* **2010,** *26*, (20), 16013-16019.

(8) Liu, S. B.; Zeng, T. H.; Hofmann, M.; Burcombe, E.; Wei, J.; Jiang, R. R.; Kong, J.; Chen, Y., Antibacterial Activity of Graphite, Graphite Oxide, Graphene Oxide, and Reduced Graphene Oxide: Membrane and Oxidative Stress. *ACS Nano* **2011,** *5*, (9), 6971-6980.

(9) Roy, M.; Sonkar, S. K.; Tripathi, S.; Saxena, M.; Sarkar, S., Non-Toxicity of Water Soluble Multi-Walled Carbon Nanotube on Escherichia-coli Colonies. *J. Nanosci. Nanotechnol.* **2012,** *12*, (3), 1754-1759.

(10) Kang, S.; Mauter, M. S.; Elimelech, M., Microbial Cytotoxicity of Carbon-Based Nanomaterials: Implications for River Water and Wastewater Effluent. *Environ. Sci. Technol.* **2009,** *43*, (7), 2648-2653.

(11) Liu, X. Y.; Gurel, V.; Morris, D.; Murray, D. W.; Zhitkovich, A.; Kane, A. B.; Hurt, R. H., Bioavailability of nickel in single-wall carbon nanotubes. *Adv. Mater.* **2007,** *19*, (19), 2790-+.

Chapter 7: Conclusions and Engineering Significance

7.1 Conclusions

CNMs have been proposed to be used in a wide range of applications owing to their excellent mechanical, electrical, optical, and thermal properties. Their widespread use in consumer and industrial products and the large scale production will inevitably lead to their presence in the natural environment. However, our understanding of their environmental reactivity, mobility, and toxicity is still very limited, posing a significant barrier to the sustainable development of nanotechnology. The present research focuses on the environmental transformation of two groups of CNMs, CNTs and fullerenes, in natural aquatic systems and its impact on their environmental fate, transport, and toxicity.

The reactivity of CNMs is one of the key factors that control their environmental fate. The photochemical reactivity of CNMs and the resulting transformation products are studied in this work. The physicochemical properties of nC_{60} and CNTs are dynamic in natural aquatic systems due to their interactions with sunlight. Phototransformation of nC_{60} and COOH-MWCNTs occurs at significant rates under UVA irradiation at intensity similar to that of sunlight. The transformation is mainly mediated by photogenerated ROS, leading to oxygenation or deoxygenation of the nanocarbon surface depending on its initial surface oxidation state. nC_{60} generates $^1O_2$ in the presence of molecular oxygen and sunlight, which in turn oxidizes its surface [1]. The reaction with $^1O_2$ initially oxidizes the external surfaces of nC_{60} without reducing the particle size. As the reaction proceeds, significant dissolution of intermediates occurs in weeks, leading to the reduction of particle size [2]. The mineralization of nC_{60} is expected after long-term solar irradiation [3, 4].

Thus photodegradation is an important fate process for nC_{60}, which needs to be carefully evaluated in risk assessment. COOH-MWCNTs were found to produce both $^1O_2$ and ·OH upon solar irradiation. These two major ROS have differential effects on CNT structures. $^1O_2$ reacts with the carboxyl groups and graphitic sidewall, leading to a more oxidized CNT surface. ·OH initially reacts with the carboxylated carbonaceous fragments on CNT surface, resulting in their degradation or exfoliation. Further reaction between ·OH and the graphitic sidewall leads to formation of defects including functional groups and holes. Reactions with self-generated ·OH are proposed to be the major reason for the phototransformation of COOH-MWCNTs. UVA irradiation reduces the surface oxygen of COOH-MWCNTs by removing surface carboxyl groups. Long-term solar exposure is expected to introduce more defects onto the CNT surface and possibly degrade the external carbon sidewall. Nevertheless, MWCNTs have multiple layers of sidewalls and contain millions of carbon atoms, thus they are not likely to be photodegraded within a reasonable timescale. SWCNTs, on the other hand, are expected to be more susceptible to photodegradation. Biodegradation of CNMs is out of scope of this study, but it is another possible major fate process of CNMs as suggested in the literature [5].

The environmental behaviors of CNMs are very sensitive to their structure changes. As a result, interactions between CNMs and major environmental components such as sunlight and NOM significantly alter their environmental mobility and toxicity. The mobility of nC_{60} and CNTs was found to strongly depend on their surface chemistry, the concentration and properties of NOM, and the ionic concentration and composition of water. In NaCl solutions, the colloidal stability of COOH-MWCNTs correlates well with the abundance of surface carboxyl groups. COOH-MWCNTs with more surface carboxyl

groups have higher surface charge and consequently higher stability. On the other hand, the stability of nC_{60} depends on their surface oxygen concentration. The CCC values of the initial nC_{60} and COOH-MWCNTs are 84 mM and 226 mM NaCl respectively. Thus they are very unstable and tend to settle in seawater of which the ionic strength is usually larger than 600 mM. But their CCC are much higher than the typical ionic strength of freshwater (< 10 mM). In this case, the presence of multivalent cations, especially Ca^{2+}, and NOM plays a more important role in the mobility of CNMs than the total ionic strength of the water. Ca^{2+} has higher valence and is known to specifically interact with the oxygen-containing functional groups on CNM surfaces. Thus it is very efficient in destabilizing CNM particles. The CCC values of the initial nC_{60} and COOH-MWCNTs are 4.25 mM and 0.86 mM respectively in $CaCl_2$ solutions. Most Ca^{2+} in freshwater comes from the calcium-containing soils and rocks such as limestone, gypsum, dolomite, etc. Its concentration varies a lot from less than 0.1 mM to several mM [6], depending on the local geology. NOM is another key factor that controls the mobility of CNM nanoparticles. Humic acid at environmental concentrations is used as a surrogate for NOM in this study. Once adsorbed onto nC_{60} surface, humic acid hinders its aggregation and deposition mainly through steric hindrance forces. The extent of this effect depends on the properties and amount of humic acid adsorbed. Humic acid immobilized onto the silica surface can potentially enhance or hinder nC_{60} deposition, depending on the complex interplay of DLVO and non-DLVO interactions.

Solar irradiation can alter the mobility of CNMs by changing their surface chemistry and their interactions with NOM. Surface oxidation induced by UVA irradiation hinders nC_{60} aggregation and deposition on silica surface in NaCl solutions due to the increased

negative surface charge and hydrophilicity; it enhances nC_{60} aggregation in $CaCl_2$ solutions due to specific interactions of Ca^{2+} with the negatively charged oxygen-containing functional groups on irradiated nC_{60} surface. UVA irradiation reduces the surface carboxyl groups of COOH-MWCNTs, leading to increased aggregation and deposition on a silica surface in NaCl solutions. However, the surface potential and colloidal stability of COOH-MWCNTs remain stable in $CaCl_2$ solutions after UVA irradiation. Humic acid has limited adsorption on the more hydrophilic and negatively charged surface of irradiated nC_{60} and is expected to play a less important role in its stability.

The toxicity of MWCNTs is found to be closely related to their surface chemistry. MWCNTs with pristine graphitic sidewalls are more toxic to bacteria, *E. coli*, than highly oxidized COOH-MWCNTs due to their higher oxidative capacity and bioavailability. Phototransformation of MWCNTs leads to more oxidized surfaces, reducing their toxicity. Oxidative stress is identified as a major toxicity mechanism for MWCNTs. Antioxidants such as reduced glutathione can effectively protect cells from the negative impact of MWCNTs.

The present research addresses environment-induced structural changes of CNTs and fullerens and the structure-activity relationships for their mobility and toxicity. The findings in this work, to some extent, can be extrapolated to other CNMs such as graphenes and graphene oxides. It provides critical information for environmental fate and risk modeling of CNMs. It also highlights that a better quantitative understanding of environment-induced changes in CNM structure is crucial to assessing their potential environmental risks.

7.2 Engineering Significance

The present dissertation work is the first study that systematically investigates the impact of environment-induced transformation (e.g., sunlight exposure and NOM addition) on the structure, fate and transport, and toxicity of CNMs in natural aquatic systems. It contributes to the mechanistic understanding of the photochemical transformation of CNMs including fullerene nanoparticles and carbon nanotubes as well as the consequent impact on their environmental risks. It also contributes to knowledge of the role of NOM in the aggregation and deposition behaviors of CNM nanoparticles. These findings provide fundamental understanding of the reactivity, mobility, and toxicity of CNMs in natural aquatic systems, enabling better risk assessment and management. This dissertation addressed several key questions critical for predicting CNM environmental risks as discussed below.

Are CNMs reactive in natural aquatic systems? How and through which route does sunlight exposure change CNM structures?

This investigation reveals both fullerenes and CNTs undergo photochemical transformation at significant rates under UVA irradiation at intensity similar to that in sunlight. Thus they are reactive in natural aquatic systems and their structures are dynamic. This finding has significant implications for risk assessment since the environmental behaviors of CNMs are sensitive to their structure changes. The phototransformation processes of nC_{60} and COOH-MWCNTs are at least partially mediated by self-generated ROS, leading to oxygenation or deoxygenation depending on their initial surface oxidation state.

How are the mobility and toxicity of CNMs related to their structures (i.e., structure-activity relationships)?

The structure-activity relationship is a major step towards CNM modeling in the environment. In this work, correlations between several structure parameters of CNMs and their environmental behaviors have been developed and tested. The stability of CNMs against aggregation and deposition is largely decided by their surface oxygen-containing functional groups in electrolyte solutions without NOM. The mobility of nC_{60} is a function of the surface oxygen concentration. On the other hand, the mobility of COOH-MWCNTs correlates well with the abundance of surface carboxyl groups. Phototransformation influences the transport of CNMs through either introducing or removing surface oxygen-containing functional groups.

Will the traditional theories of colloid science be applicable to CNM nanoparticle transport studies?

The size of the CNM nanoparticles studied falls in the size range of colloidal particles, in which particle-particle and particle-surface interactions are extensively studied in colloidal science. One of the most commonly used theories in colloid science to interpret particle transport is the DLVO theory. In this study, the aggregation and deposition kinetics of nC_{60} and CNTs with different structures were quantified using DLS, QCM-D and packed-columns in solutions varying in ionic strength, ionic composition and humic acid concentration. In most conditions without NOM, the results qualitatively agree with the prediction of DLVO theory. Non-DLVO forces such as steric hindrance forces, hydrophobic effects, and bridging effects also can contribute to the aggregation and

deposition behaviors in specific conditions. The bottom line is that DLVO theory serves as a good starting point for the prediction of CNM environmental transport.

The role of NOM in the environmental transport of CNMs.

NOM is one of the most important controlling factors in the environmental transport of CNMs. Once adsorbed on the surface of nC_{60}, humic acid molecules can greatly enhance its stability through steric hindrance. However, the stabilization effect depends on the amount and properties of humic acid adsorbed. Sunlight-induced surface oxidation of nC_{60} reduces the humic acid sorption. Soil humic acid is found to be more efficient than aquatic humic acid in stabilizing nC_{60} due to its higher molecular weight, which provides stronger steric hindrance.

7.3 Future Research

The risk assessment of CNMs is still in its infancy. Other than the questions addressed in this dissertation, there are still many remaining challenges. Several areas that immediately relate to the scope of this dissertation are proposed for future research.

The indirect photochemical transformation of CNMs.

In this study, the photochemical transformation of CNMs in lab conditions (mostly in deionized water) was found to be mediated by self-generated ROS. However, the transformation processes of CNMs under environmentally relevant conditions, which are often highly heterogeneous, are still not well understood. It is well known that ROS can be generated in natural waters by nitrite and nitrate photolysis, dissolved NOM photosensitization and photo-Fenton reactions. The natural background ROS will

inevitably lead to the indirect phototransformation of CNMs, which is expected to be a major transformation route. Nevertheless, the indirect phototransformaiton of CNMs hasn't yet been addressed in the literature.

Biodegradation of CNMs

CNTs can be degraded by several enzymes such as horseradish peroxidase, myeloperoxidase that are often involved in the biodegradation processes [5, 7, 8]. Thus it is possible for them to be biodegraded in natural settings. Biodegradation is especially important for CNTs, which have large structures and cannot be photodegraded within a reasonable timescale. Bacteria and fungi[9] known to be capable of degrading polycyclic aromatic hydrocarbons are the ideal candidates for biodegradation tests. The abiotic and biotic transformation routes are most likely coupled. ROS with high oxidative potential can potentially prepare CNMs for subsequent biodegradation which relies on enzymes and their byproducts with lower oxidative potential. Thus the impact of phototransformation on the biodegradability of CNMs is also of interest.

Heteroaggregation of CNMs with naturally occurring particles.

The aggregation study presented in this dissertation mainly focuses on homoaggregation which is the aggregation between the CNM nanoparticles. In natural aquatic systems, there are different kinds of naturally occurring particles (e.g., clay particles and microorganisms) at concentrations far exceeding that of CNM nanoparticles. Although the investigation of homoaggregation provides some insight into the CNM colloidal stability, the heteroaggregation between CNM nanoparticles and natural occurring particles has higher environmental significance. In order to predict the fate and

transport of CNMs in aquatic systems, research is needed to address the heteroaggregation of CNMs in environmentally relevant conditions.

7.4 References

(1) Hou, W. C.; Jafvert, C. T., Photochemistry of Aqueous C(60) Clusters: Evidence of (1)O(2) Formation and its Role in Mediating C(60) Phototransformation. *Environ. Sci. Technol.* **2009,** *43*, (14), 5257-5262.

(2) Hou, W. C.; Kong, L. J.; Wepasnick, K. A.; Zepp, R. G.; Fairbrother, D. H.; Jafvert, C. T., Photochemistry of Aqueous C(60) Clusters: Wavelength Dependency and Product Characterization. *Environ. Sci. Technol.* **2010,** *44*, (21), 8121-8127.

(3) Hou, W. C.; Jafvert, C. T., Photochemical Transformation of Aqueous C(60) Clusters in Sunlight. *Environ. Sci. Technol.* **2009,** *43*, (2), 362-367.

(4) Hwang, Y. S.; Li, Q. L., Characterizing Photochemical Transformation of Aqueous nC(60) under Environmentally Relevant Conditions. *Environ. Sci. Technol.* **2010,** *44*, (8), 3008-3013.

(5) Kotchey, G. P.; Hasan, S. A.; Kapralov, A. A.; Ha, S. H.; Kim, K.; Shvedova, A. A.; Kagan, V. E.; Star, A., A Natural Vanishing Act: The Enzyme-Catalyzed Degradation of Carbon Nanomaterials. *Accounts of Chemical Research* **2012**.

(6) Jeziorski, A.; Yan, N. D.; Paterson, A. M.; DeSellas, A. M.; Turner, M. A.; Jeffries, D. S.; Keller, B.; Weeber, R. C.; McNicol, D. K.; Palmer, M. E.; McIver, K.; Arseneau, K.; Ginn, B. K.; Cumming, B. F.; Smol, J. P., The Widespread Threat of Calcium Decline in Fresh Waters. *Science* **2008,** *322*, (5906), 1374-1377.

(7) Allen, B. L.; Kichambare, P. D.; Gou, P.; Vlasova, II; Kapralov, A. A.; Konduru, N.; Kagan, V. E.; Star, A., Biodegradation of Single-Walled Carbon Nanotubes through Enzymatic Catalysis. *Nano Lett.* **2008,** *8*, (11), 3899-3903.

(8) Allen, B. L.; Kotchey, G. P.; Chen, Y. N.; Yanamala, N. V. K.; Klein-Seetharaman, J.; Kagan, V. E.; Star, A., Mechanistic Investigations of Horseradish Peroxidase-Catalyzed Degradation of Single-Walled Carbon Nanotubes. *J. Am. Chem. Soc.* **2009,** *131*, (47), 17194-17205.

(9) Schreiner, K. M.; Filley, T. R.; Blanchette, R. A.; Bowen, B. B.; Bolskar, R. D.; Hockaday, W. C.; Masiello, C. A.; Raebiger, J. W., White-Rot Basidiomycete-Mediated Decomposition of C-60 Fullerol. *Environ. Sci. Technol.* **2009,** *43*, (9), 3162-3168.